DEVELOPMENT OF BIFUNCTIONAL CATALYST FOR THE SINGLE-STEP
SYNTHESIS OF DIMETHYL ETHER

A THESIS SUBMITTED TO
THE GRADUATE SCHOOL OF NATURAL AND APPLIED SCIENCES
OF
MIDDLE EAST TECHNICAL UNIVERSITY

BY

MEHMETALİ İLKER ŞENER

IN PARTIAL FULFILLMENT OF THE REQUIREMENTS
FOR
THE DEGREE OF MASTER OF SCIENCE
IN
CHEMICAL ENGINEERING

JULY 2019

Approval of the thesis:

DEVELOPMENT OF BIFUNCTIONAL CATALYST FOR THE SINGLE-STEP SYNTHESIS OF DIMETHYL ETHER

submitted by **MEHMETALİ İLKER ŞENER** in partial fulfillment of the requirements for the degree of **Master of Science in Chemical Engineering Department, Middle East Technical University** by,

Prof. Dr. Halil Kalıpçılar
Dean, Graduate School of **Natural and Applied Sciences**   _____

Prof. Dr. Pınar Çalık
Head of Department, **Chemical Engineering**   _____

Prof. Dr. Naime Aslı Sezgi
Supervisor, **Chemical Engineering, METU**   _____

Prof. Dr. Timur Doğu
Co-Supervisor, **Chemical Engineering, METU**   _____

Examining Committee Members:

Prof. Dr. Suna Balcı
Chemical Engineering, Gazi University   _____

Prof. Dr. Naime Aslı Sezgi
Chemical Engineering, METU   _____

Assoc. Prof. Dr. Dilek Varışlı
Chemical Engineering, Gazi University   _____

Assist. Prof. Dr. Zeynep Tutumlu
Material Sci. and Nanotech., TOBB ETU   _____

Assist. Prof. Dr. Bahar İpek Torun
Chemical Engineering, METU   _____

Date: 29.07.2019

I hereby declare that all information in this document has been obtained and presented in accordance with academic rules and ethical conduct. I also declare that, as required by these rules and conduct, I have fully cited and referenced all material and results that are not original to this work.

Name, Surname: Mehmetali İlker Şener

Signature:

ABSTRACT

DEVELOPMENT OF BIFUNCTIONAL CATALYST FOR THE SINGLE-STEP SYNTHESIS OF DIMETHYL ETHER

Şener, Mehmetali İlker
Master of Science, Chemical Engineering
Supervisor: Prof. Dr. Naime Aslı Sezgi
Co-Supervisor: Prof. Dr. Timur Doğu

July 2019, 159 pages

Depletion of fossil fuels, global warming concerns and increasing CO_2 emissions necessitated the utilization of syngas in the production of alternative fuels over the last few years. Dimethyl ether (DME) is considered as promising diesel substitute or LPG additive due to its high cetane number and good burning properties.

The single-step DME synthesis method, which involves consecutive methanol formation and methanol dehydration reactions, enables the production of DME directly from the syngas. Despite the advantage of breaking the thermodynamic limitation in the single-step DME synthesis, development of an bifunctional catalyst to synthesize DME from the syngas is a challenging topic.

Mesoporous alumina and mesoporous carbon supports were synthesized. Cu-Zn metals were loaded for the methanol synthesis reaction whereas tungstophosphoric acid (TPA) was loaded for the methanol dehydration reaction into these supports with different amounts using impregnation and one-pot methods. Synthesized catalysts were characterized by XRD, N_2 physisorption, TGA, TPR, TPD, SEM-EDX.

Thermodynamic equilibrium analyses showed that the optimum molar CO/H_2 ratio was 1/1 and the optimum operating temperature was 275°C under 50 bar pressure.

Performance tests were carried out at these conditions in DME production system for the single-step DME synthesis from syngas.

Commercial alumina and methanol synthesis catalyst mixture was the most catalytically active couple among all catalysts. TPA loaded catalysts inhibited the water-gas shift reaction and showed high CO conversion and high methanol and DME selectivities. Optimum TPA loading was determined as 10 wt. %, regardless of the loading method. The highest CO conversion was obtained as 53% with 43% DME selectivity over 10 wt. % TPA impregnated alumina catalyst mixed with commercial methanol synthesis catalyst with the molar CO/H_2 ratio of 1/1 among the synthesized catalysts.

The highest DME selectivity was found to be 78.5% from syngas containing 25% CO_2, whereas the highest total conversion was found to be 34.5% from syngas containing 10% CO_2 in the presence of commercial methanol synthesis and alumina mixture.

The TPA and Cu-Zn loaded bifunctional CMK-3 catalyst showed higher DME selectivity compared to the TPA and Cu-Zn loaded bifunctional EMA catalyst.

Keywords: DME, Syngas, Methanol, TPA, Alumina, Bifunctional

ÖZ

TEK BASAMAKTA DİMETİL ETER SENTEZİ İÇİN ÇİFT FONKSİYONLU KATALİZÖR GELİŞTİRİLMESİ

Şener, Mehmetali İlker
Yüksek Lisans, Kimya Mühendisliği
Tez Danışmanı: Prof. Dr. Naime Aslı Sezgi
Ortak Tez Danışmanı: Prof. Dr. Timur Doğu

Temmuz 2019, 159 sayfa

Fosil yakıtların tükenmesi, küresel ısınma endişeleri ve artan CO_2 salınımları, son birkaç yılda alternatif yakıtların üretiminde sentez gazının kullanımını zorunlu kılmıştır. Dimetil eter (DME), yüksek setan sayısı ve iyi yanma özellikleri nedeniyle ümit verici dizel alternatifi veya LPG katkı maddesi olarak kabul edilmektedir.

Ardışık metanol sentezi ve metanol dehidrasyon reaksiyonlarını içeren tek basamaklı DME sentezi ile sentez gazından doğrudan DME üretilmesi sağlanır. Tek basamaklı DME sentezi ile termodinamik denge sınırlamasının aşılabilmesine rağmen, DME'yi sentez gazından sentezlemek için çift fonksiyonlu katalizörler halen geliştirilme aşamasındadır.

Mezogözenekli alümina ve mezogözenekli karbon katalizör destek malzemeleri sentezlenmiştir. Metanol sentez reaksiyonu için Cu-Zn metalleri yüklenirken, metanol dehidrasyon reaksiyonu için emdirme ve tek-kap sentez yöntemleri kullanılarak bu desteklere farklı miktarlarda tungsfosforik asit (TPA) yüklenmiştir. Sentezlenen katalizörler XRD, azot fizisorpsiyonu, TGA, TPR, TPD ve SEM-EDX ile karakterize edilmiştir.

Termodinamik denge analizleri, 50 bar basınçta optimum CO/H_2 molar oranının 1'e 1, optimum reaktör sıcaklığının 275°C olduğunu göstermiştir. DME üretim sisteminde, sentez gazından tek basamaklı DME sentezi için performans testleri bu koşullarda yapılmıştır.

Ticari alümina ve metanol sentez katalizör karışımı, tüm katalizörler arasında en yüksek katalitik aktiviteyi gösteren çift olmuştur. TPA yüklü katalizörler, su gaz değişimi reaksiyonunu baskılarken, yüksek CO dönüşümü ve yüksek metanol ve DME seçiciliği göstermiştir. Yükleme yönteminden bağımsız olarak optimum TPA yükleme oranının ağırlıkça %10 olduğu görülmüştür. Sentezlenen katalizörler içerisinde 1'e 1 CO/H_2 molar oranı ile en yüksek CO dönüşümü %53 olarak %43 DME seçiciliği ile, ağırlıkça %10 TPA emdirilmiş alümina katalizörü ile karıştırılmış ticari metanol sentez katalizörü kullanılarak elde edilmiştir.

En yüksek DME seçiciliği %25 CO_2 içeren sentez gazından %78,5 olarak bulunurken, ticari metanol sentez ve alümina katalizör karışımı varlığında en yüksek toplam dönüşüm %10 CO_2 içeren sentez gazından %34,5 olarak bulunmuştur.

TPA ve Cu-Zn yüklenmiş iki fonksiyonlu CMK-3 katalizörü, TPA ve Cu-Zn yüklenmiş iki fonksiyonlu EMA katalizörüne göre daha yüksek DME seçiciliği göstermiştir.

Anahtar Kelimeler: DME, TPA, Alümina, Metanol, Sentez Gazı

To My Beloved Family…

ACKNOWLEDGEMENTS

I would like to express my sincere gratitude to my supervisor Prof. Dr. Naime Aslı Sezgi for her endless support and guidance throughout this thesis. She encouraged and helped me with her deepest knowledge all the time. I take this opportunity to acknowledge her for helping me make this thesis possible.

I also would like to express my gratitude to my co-supervisor Prof. Dr. Timur Doğu. Without his support and guidance, this work would not be possible. He helped me with his deepest knowledge at all points of this study.

I would like to offer my sincere thanks to Prof. Dr. Nuray Oktar for the valuable things she taught me and for her strong support on me all the time. Her belief in me was invaluable for me.

I also would like to thank Prof. Dr. Gülşen Doğu for her encouragement and her positive attitude in every aspect.

Arzu was my oldest lab mate, my teaching assistant and now she is my colleague. I would like to thank for her insightful comments and motivation. I would like to express my gratitude to Merve for her support and all the fun we have had in the last four years. I also would like to thank Zeynep & Veysi, Canan, Fatma, Merve, Seda, Ezgi, Burak, Pınar, Abdul Rehman, Saeed and other people from Chemical Engineering Department. It was great sharing laboratory and the department with all of them during the last four years.

I am grateful to Tuğçe for supporting me spiritually throughout my life more than 10 years. I also would like to express my gratitude to Fulya, Gürhan & Zeynep, Çağrı & Duygu, Cansu, Eren for being invaluable friends.

TABLE OF CONTENTS

LIST OF TABLES

LIST OF FIGURES

xx

LIST OF ABBREVIATIONS

ABBREVIATIONS

BET: Brunauer–Emmett–Teller

BJH: Barrett, Joyner, and Halenda

CA: Commercial alumina

DME: Dimethyl ether

EDX: Energy-dispersive X-ray spectroscopy

EMA: Mesoporous alumina synthesized using EISA method

EOS: Equation of state

EtOH: Ethanol

FA: Formic acid

GC: Gas chromatography

MeOH: Methanol

MSC: Commercial methanol synthesis catalyst

SEM: Scanning electron microscope

TCD: Thermal conductivity detector

TGA: Thermogravimetric analysis

TPA: Tungstophosphoric acid

TPD: Temperature programmed desorption

TPR: Temperature programmed reduction

WGS: Water-gas shift reaction

XRD: X-Ray Diffraction

LIST OF SYMBOLS

SYMBOLS

A_i **:** Area of component i in the GC pictogram

E_{des} **:** Activation energy of desorption, J/mol

K : Equilibrium constant

n_i **:** Number of moles of component i, mol

n_{eqm} **:** Number of moles of component i at equilibrium, mol

n_t **:** number of moles of component i at any time, mol

P : Pressure, bar

P_o **:** Saturated pressure of adsorbate gas, mmHg

Pc : Critical pressure of the component, bar

R : Ideal gas constant, J/molK

X_i **:** Fractional conversion of component i

T : Temperature, K

T_c **:** Critical temperature of the component, K

S_i **:** Selectivity of species i

y_i **:** Mole fraction of species i

z : Compressibility factor

Greek Letters

ϕ_i **:** Fugacity coefficient of species i

β_i **:** Beta factor of component i

β **:** Heating rate, K/s

θ **:** Bragg angle, °

ω_i **:** Acentric factor of the species i

$\Delta G°$ **:** Gibbs free energy of the reaction, J/mol

ΔH **:** Enthalpy of the reaction, J/mol

CHAPTER 1

INTRODUCTION

Fast increase in the rate of energy consumption and related environmental problems necessitated the development of sustainable alternative fuels. In addition, fast depletion of fossil fuel reserves and the continuous increase in petroleum product prices have initiated major research for the development of non-petroleum transportation fuel alternates. Moreover, increase in the rate of global warming and the emission of pollutants from the diesel engines of buses and trucks has also initiated new research for the production of clean fuels.

Searching for an alternative fuel production has increased considerably over the last years in order to improve engine performance while reducing the air pollution. Alternative fuels can be used directly in engines as fuel (e.g. biodiesel, dimethyl ether) or fuel additive for a better burning performance resulting in a longer engine life.

Combustion of fuels in cars and trucks produces sulfur oxides (SO_x) along with the other combustion gases. Emission of SO_x gases are regulated by the laws in cars and other industries since these gases are known as one of the main air pollutant and cause of acid rain. Therefore, different desulfurization processes are required in refineries to reduce the sulfur content of petroleum fuels to ppm levels. Alternative fuels are more attractive compared to fossil fuels due to their low sulfur content since these fuels usually do not require desulfurization processes.

Alternative fuels are generally obtained from non-petroleum, renewable sources, agricultural products and wastes. They are usually biologically degradable and these fuels can be stored easily because of their high flash point.

Development of alternative fuel industry will also create new employment areas, improve agriculture and reduce internal migration (Ozbay, 2008).

1

Among these alternative fuels, dimethyl ether (DME) is a promising fuel due to its superior properties (Ozbay, 2008). DME can be produced either directly from synthesis gas or from dehydration of methanol.

1.1. Importance of DME

Searching for a new alternative fuel has been increased globally for the last decades. Methanol from natural gas or coal is a well-known production method, therefore it is known as an alternative fuel and fuel additive. However, environmental, health and safety concerns prevent the widespread use of methanol transportation fuel. Also the main drawback of the methanol production is the low raw material conversion due to thermodynamic limitations.

DME is also an attractive fuel alternative since it can be either used as a diesel substitute or LPG additive to improve engine performance. Moreover, DME is preferred due to its higher cetane number and higher oxygen content compared to conventional diesel. It also has very low emission features which makes this fuel both environmentally and customer friendly and provide to design a new diesel engine technology (Fleisch et al., 1997).

Converting natural gas or coal to liquid fuel is achieved usually in two step using suitable processes. In the first step gasification of coal or steam reforming of natural gas used to obtain syngas and in the second stage Fischer-Tropsch is usually used to convert the syngas mixture into a liquid-solid hydrocarbon mixture. However, this product cannot be directly used and requires catalytic or thermal cracking and fractionation processes. Hence, converting natural gas or coal to DME production reduces the number of processing steps and capital investment.

DME has similar handling and storing properties to LPG. LPG contains C_3-C_4 hydrocarbons and pipeline and storage tanks of LPG can be used for DME.

1.2. Properties of DME

DME has the chemical formula of CH_3-O-CH_3 which is the simplest ether compound. DME is a colorless, nontoxic, non-corrosive, and non-carcinogenic gas. It is a volatile organic compound with a low boiling point of -25°C (Zhang et al., 2011). Its vapor pressure is about 600 kPa at 25°C which allows easy liquefaction under low pressure (Ogawa et al, 2004).

DME has high oxygen content (about 35wt%) and it does not contain sulfur and nitrogen. Therefore, during combustion of DME, it creates smokeless, clean exhaust gas. Moreover, owing to the high cetane number (55-60), it is preferable for diesel engines (Fleisch et al., 1997). DME can also be used as LPG additive since it has similar physical properties. Table 1.1 shows the physical properties of DME.

Table 1.1. *Properties of DME* (Ogawa et al., 2004)

Properties	
Molecular formula	C_2H_6O
Boiling point (K)	247.9
Liquid density (g/cm^3 at 293K)	0.67
Specific gravity (vs air)	1.59
Vapor pressure (atm at 293K)	6.1
Explosion limit	3.4-17
Cetane number	55-60
Net calorific value (MJ/Nm^3)	59.44
Net calorific value (J/kg)	28.90

1.3. Usage areas of DME

DME has been attracting attention significantly in many areas due to its unique properties. Smokeless and effective combustion properties of DME provide proper usage in diesel engines as fuel or fuel additive (Fleisch et al., 1997). It is a very good alternative to liquefied petroleum gas (LPG) especially for household use due to its similar properties to propane and butane.

DME is easily converted to liquid and gaseous forms and cleaner than chlorofluorocarbons (CFCs, Freon), therefore it is proper to use as a refrigerant (Azizi et al., 2014). Moreover, DME can be used not only as fuel in fuel cells but also electricity generation in power plants. Additionally, DME has wide applications such as cosmetic products, pesticide, polishing agent and propellant (Zhang et al., 2011; Lu et al., 2004; Adachi et al, 2000b).

1.4. Production Methods of DME

In the synthesis of DME from syngas, the main reactions are methanol synthesis (R1, R2), methanol dehydration reaction (R3) and the water gas shift reaction (R4) as a side reaction (Ogawa et al, 2004; Celik et al., 2013).

$$CO + 2H_2 \leftrightarrow CH_3OH \tag{R1}$$

$$CO_2 + 3H_2 \leftrightarrow CH_3OH + H_2O \tag{R2}$$

$$2CH_3OH \leftrightarrow CH_3OCH_3 + H_2O \tag{R3}$$

$$CO + H_2O \leftrightarrow CO_2 + H_2 \tag{R4}$$

Although a few DME plants and demo plants are available, industrial scale DME production is not completely became widespread and commercialized yet. Hence, a few DME production methods are available. However, the most common DME production methods are two-step process or single-step from synthesis gas. These two pathways for production of DME are given in Figure 1.1.
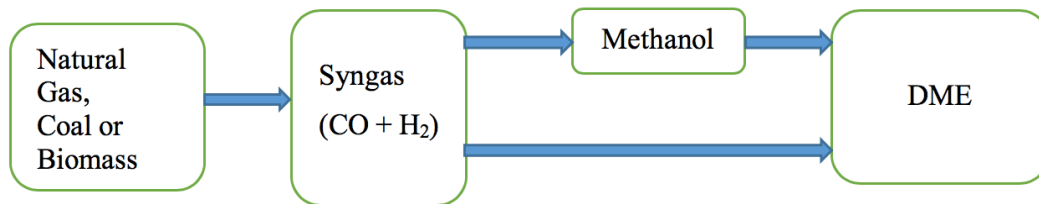
Figure 1.1. Possible pathways for production of DME (adapted from Fleisch et al., 1997)

First route is the conventional two-step process, which involves hydrogenation reaction to produce methanol from syngas (R1 and R2) using copper-zinc catalyst and then dehydration of methanol to produce DME (R3) in the presence of solid acid catalyst in a separate reactor. This production method enables to use of methanol as raw material. Therefore, it is suitable for the methanol production plants that are already in operation.

The second route involves R1, R2 and R3 reactions in the same reactor, in the presence of a bifunctional catalyst. Methanol production from syngas is highly limited by the thermodynamic equilibrium. But the single-step synthesis of DME, i.e., production of methanol from syngas and then DME production from methanol dehydration in the same reactor, breaks the equilibrium limitations and increases CO conversion. In this route, by lowering the water level through the water-gas shift (WGS) reaction (R4), methanol dehydration and CO conversion can be increased (Peng et al., 1999).

Overall stoichiometry of these reactions for producing DME from syngas, which contains a mixture of CO and H_2 can be expressed as (R5) and (R6) (Ogawa et al., 2004; Celik et al., 2013).

$$3CO + 3H_2 \leftrightarrow CH_3OCH_3 + CO_2 \hspace{3cm} \text{(R5)}$$

$$2CO + 4H_2 \leftrightarrow CH_3OCH_3 + H_2O \hspace{3cm} \text{(R6)}$$

All reactions in the production of DME are highly exothermic and they are significantly limited by the thermodynamic equilibrium. However, the single-step DME synthesis from syngas has more advantages compared to the two-step synthesis process (Celik et al., 2013). The single-step DME synthesis process allows higher DME production rates due to combining methanol formation and methanol dehydration reactions (R1, R2, R3) in a single reactor (Peng et al., 1999). It is also a cost efficient process compared to the two-step process, since the single-step DME synthesis process does not require any additional dehydration reactor.

1.5. Fuel Characteristics

DME is the simplest ether with an oxygen atom. Having a higher cetane number than the conventional petroleum diesel makes it more attractive, compared to its opponents. DME is also considered as a new alternative fuel in terms of environmental and economical point of view.

DME has calorific value (lower level) of 6900 kcal/kg that is lower than that of propane, but higher than that of methanol (Adachi et al., 2000a) Due to its high cetane number (55-60), it is an excellent alternative for diesel-engines (Ciftci et al., 2010). Since it has low boiling point, fast fuel/air mixing is achieved that leads to decrease ignition delay, and it is useful especially at cold start of vehicles (Fleisch et al., 1997).

DME is easily liquidified, hence it is easy to handle fuel. Since, it has similar vapor pressure to that of LPG, storage and transportation can be done based on available LPG handling techniques. Low emission of CO, NO_x and particulates resulting from the combustion process of DME shows its clean burning characteristics, so it can be classified as environmentally friendly fuel (Azizi et al., 2014).

1.6. Safety Data

DME can be classified as clean and safe compound. DME has hardly any odor at low concentrations in gaseous form and causes no negative health effects (Varişli et al., 2009). It has been reported as a non-carcinogenic, non-mutagenic and non-toxic compound (Fleisch et al., 1997). In addition to that, it does not form explosive peroxides. Therefore, based on LPG handling technology, it provides safe storage and transportation.

DME is a clean alternative in terms of having no particulate matter and low emissions of CO, NOx. Having zero ozone depletion and lower global warming potentials compared to CFCs makes DME environmentally friendly aerosol and green refrigerant (Azizi et al., 2014).

CHAPTER 2

CATALYSIS

Solid catalysts are used in many applications from lab scale to industrial scale productions. Lowering the activation energy of the reaction is the main aim of the catalysts. Catalytic activity, product selectivity, and stability are the essential parameters in the selection of the catalyst. Usually catalysts have porous structure and catalytically active sites on their surface to catalyze the reaction. Many phenomena such as adsorption/desorption, diffusion and interaction of reactant species to these active sites may take place during the reactions.

Different types of active sites exist on the catalyst and these active sites provide the reactions taking place with different reaction mechanisms. Some of these catalytically active sites might be metallic site (e.g. Ni, Pt, etc.), metal oxide site (e.g. TiO_2), sulfite site (e.g. WS_2) or acidic site (zeolites, γ-alumina). Catalysts that contain two types of active sites (e.g. both acidic and metallic) are called bifunctional catalysts. Bifunctional catalysts are used for catalyzing the different reactions in tandem. Some of the conventional catalysts and their applications are given in Table 2.1.

Table 2.1. *Conventional support materials and application area* (Chorkendorff & Niemantsverdriet, 2003)

Support	Catalytically Active Phase	Application
γ-Alumina	CoMoS, NiMoS, NiWS	Hydrotreating
	Pt, Pt-Re	Reforming
	Pt, Rh, Pd	Automotive exhaust cleaning
	Cu-ZnO	Methanol synthesis
	Cu-ZnO	Water gas shift reaction
	Ni	Steam reforming
	TiO_2	Dehydration
	Pd, Pt, Ru, Rh	Hydrogenation
	Cr_2O_3, Pt	Dehydrogenation
	Pd	Dehydrochlorination
	$CuCl_2$	Oxychlorination
η-Alumina	Pt	Reforming, isomerization
α-Alumina	Ni	Steam reforming
	Ag	Epoxidation
SiO_2	CrO_x	Polymerization
	H_3PO_4	Hydration
	V_2O_5	Oxidation
TiO_2	V_2O_5	DeNOx
Carbon	Pd, Pt	Hydrogenation

A proper selection of support material and active phase is the essential key to have a selective, high performance and stable catalyst.

2.1. Catalyst Supports

Catalysts usually consist of a support material to have a high surface area and dispersed active sites. The support material itself may also have catalytically active structure (e.g. acidic structure). Zeolites, γ-alumina, SiO_2, alumina silicates and ion exchange resins are the most common acidic porous materials.

Porous materials are characterized using several techniques. Physical properties of the materials are usually determined using nitrogen physisorption, which is based on adsorption and desorption of nitrogen under different relative nitrogen pressure and isothermal conditions. Adsorption/desorption and capillary condensation mechanisms in the physisorption are demonstrated in Figure 2.1.
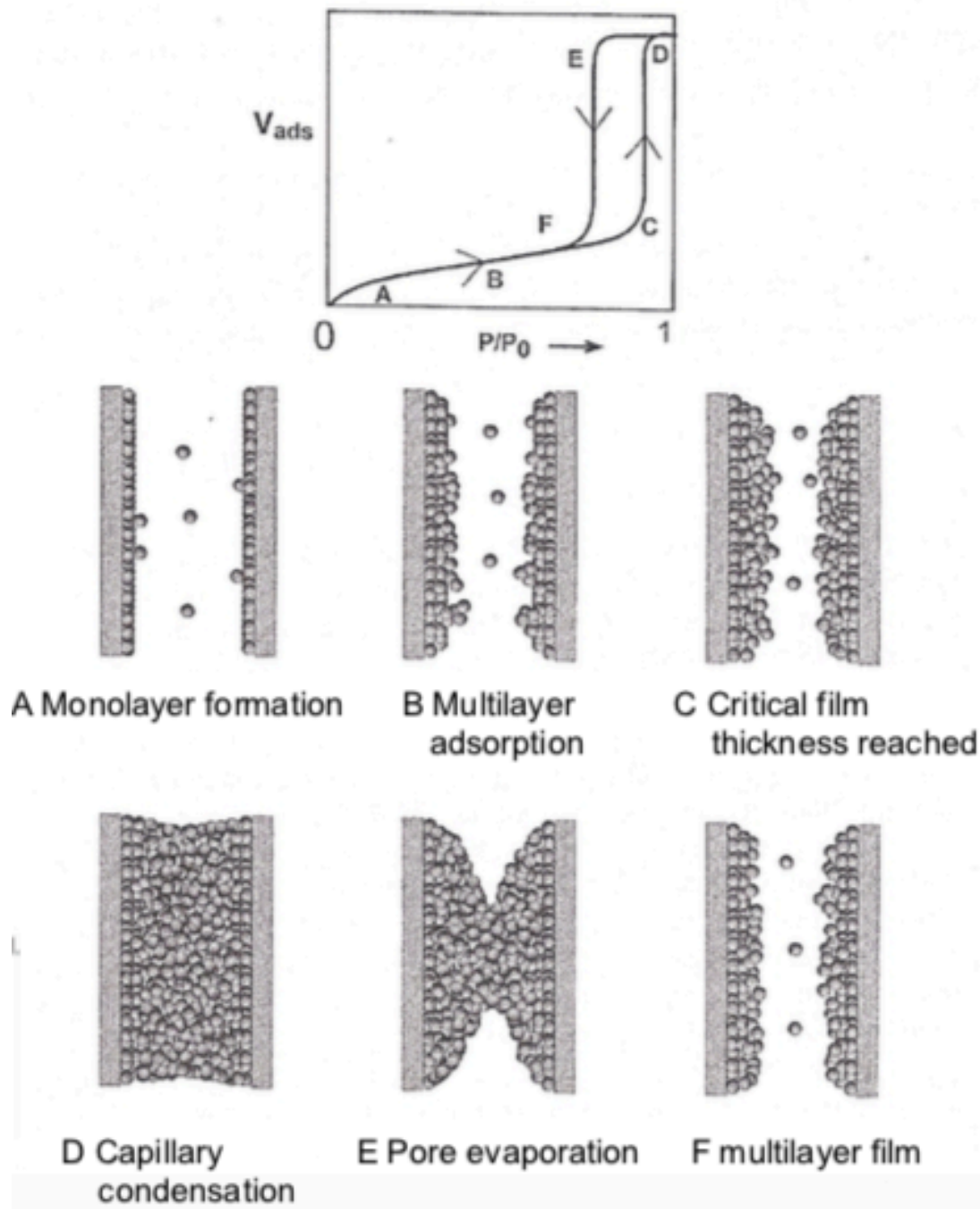
Figure 2.1. Capillary condensation mechanism (Trunschke, 2013)

Many information like surface area, pore size distribution, pore volume about the material can be obtained using the physisorption data. Porous structures are classified according to their pore diameter into three groups. IUPAC classification for the porous materials is given in Table 2.2.

Table 2.2. *UIPAC Classification for porous materials*

Pore size, nm	Classification
<2	Microporous
2-50	Mesoporous
>50	Macroporous

Zeolites usually have microporous structure, whereas SBA-15 and alumina support materials have mesoporous structure. Pore size and microporosity plays an important role for the diffusion limitation. Therefore, selection of the proper support material for the catalyst synthesis considering the physical properties (surface area, pore diameter, acidic nature) and stability is crucial.

2.1.1. Alumina Supports

Alumina supports are often used in many catalytic and adsorption applications. They are considered as very promising for many applications such as catalyst industry or ceramic industry. Conventionally alumina materials are made by thermal dehydration of aluminum hydroxides (Al(OH)$_3$; Gibbsite or Bayerite) or AlOOH (Boehmite). Alumina exists in several structure (Figure 2.2), among which only the α-alumina form is crystalline. The other structures of alumina are called transitional aluminas

and each has different crystallinity degree. Figure 2.3 shows the XRD patterns of
different types of alumina structures.
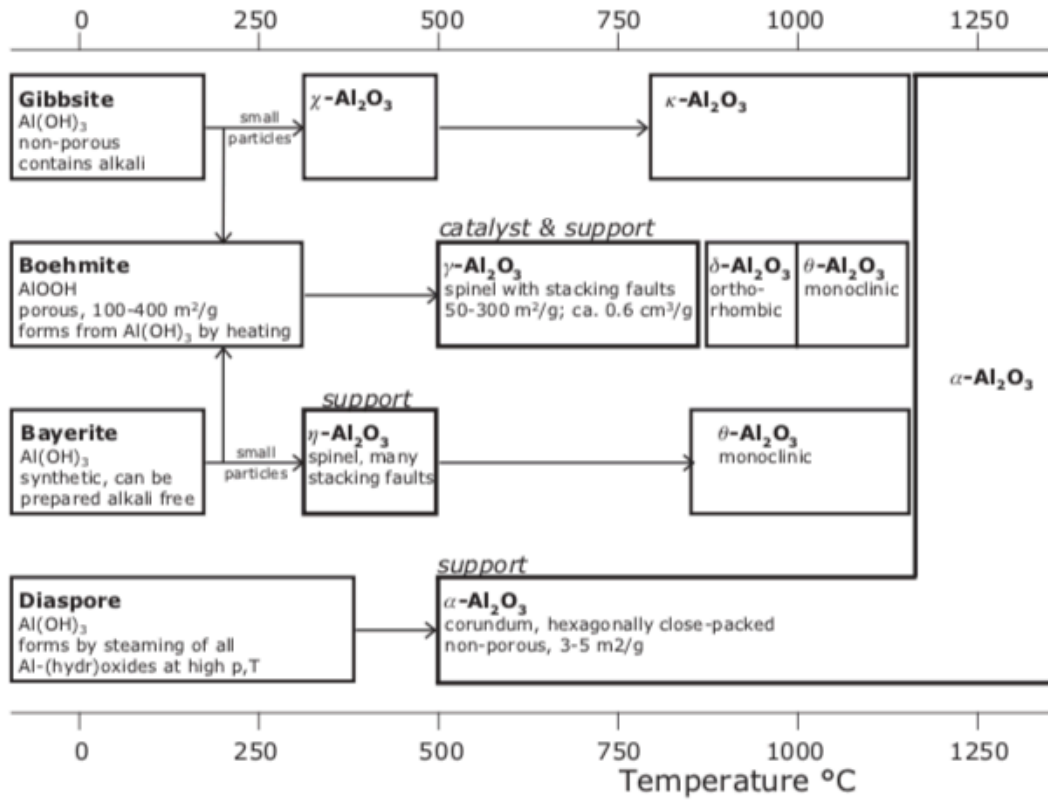
Figure 2.2. Transformations of alumina (adapted from (Chorkendorff & Niemantsverdriet, 2003))
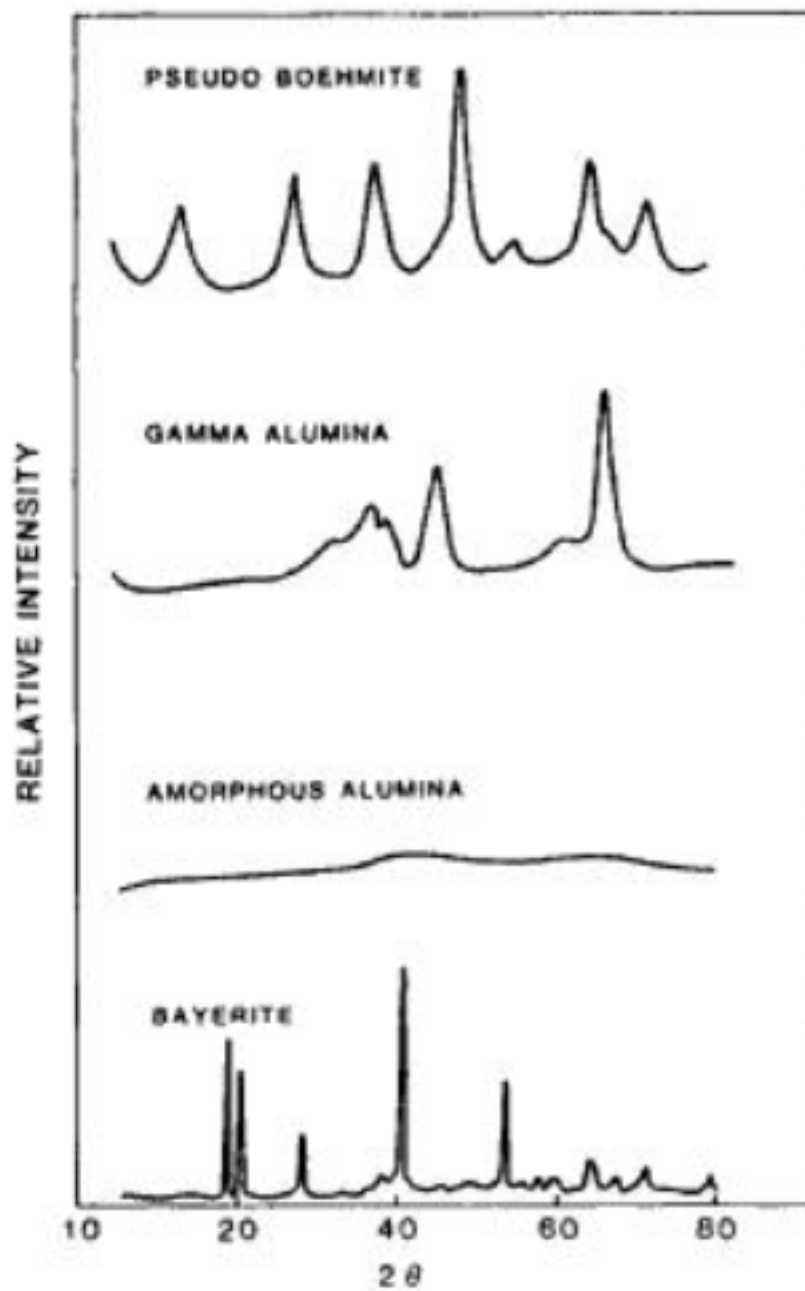
Figure 2.3. XRD patterns of different types of alumina structures (Richardson, 1989)

15

γ-alumina is the most common support material and it is used for its high acidic nature, high stability and high surface area with mesoporous structure. Calcination of amorphous alumina at low temperature yields γ-alumina instead of α-alumina structure. However, increase in the crystallinity of alumina decreases its surface area. Therefore, α-alumina, which is the most stable alumina crystal, has the lowest surface area and porosity among the other alumina types. Moreover, amorphous alumina has higher surface area and acidic nature compared to γ-alumina (Tavakoli et al., 2013; Wu et al., 2015). Hence, tuning the porosity and other physical properties of alumina material plays an important role in the catalyst development.

Mesoporous alumina support can be prepared by treating an aluminum source such as aluminum isopropoxide ($Al[OCH(CH_3)_2]_3$) in an alcohol–aqueous solvent with an organic template. The precipitate morphology determines the surface area of the final support.

2.2. Mesoporous Carbon (CMK-3)

CMK-3 is a carbon replica with superior properties such as high porosity and ordered structure, which make this material a good support material candidate. Unlike the traditional synthesis methods of carbon materials, CMK-3 can be synthesized using a nanocasting technique with inexpensive carbon precursor (such as sucrose) (Barrera et al., 2013).

Synthesis of mesoporous carbon is composed of four main steps. In the first step, inorganic porous material is used as a template and carbon precursor is impregnated. Drying of the composite is the second step. In the third step, composite material is pyrolyzed and in the final step the template is extracted by sodium hydroxide leaching (Barrera et al., 2013; Michorczyk et al., 2012; Xing et al., 2007).

Hence, synthesis of a template material with ordered porous structure is also required. SBA-15 is a good candidate for using as the template material due to its high thermal

stability and ordered porous structure. Additionally, removal of SBA-15 from the final structure is quiet easy due to solubility of Si in HF or NaOH solutions. Synthesized material using the SBA-15 as the template is the negative replica of the SBA-15 material with parallel interconnected carbon nanorods. This nanocasting technology is presented in Figure 2.4.
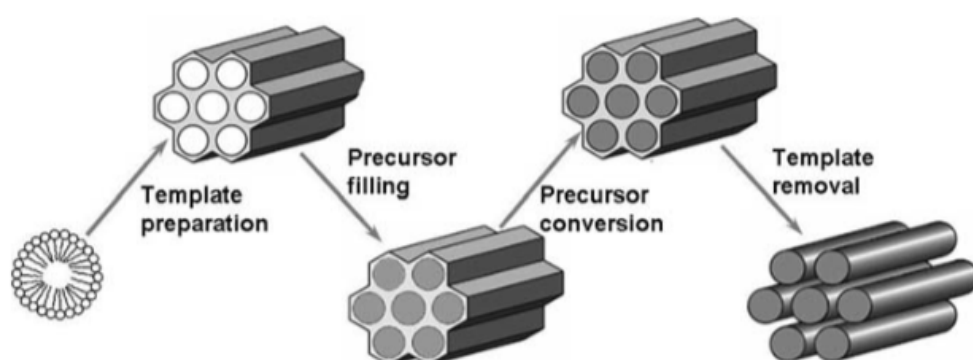
Figure 2.4. Schematic illustration of the nanocasting technology (de Jong, 2009)

It was reported that surface are of CMK-3 materials can reach above 1000 m^2/g (Barrera et al., 2013; Michorczyk et al., 2012; Xing et al., 2007).

It was also reported that synthesized mesoporous carbon materials exhibited a hydrophobic nature (Barrera et al., 2013; He et al., 2009). This unique feature of CMK-3 may enable the use of CMK-3 in the dehydration and reverse water-gas shift (WGS) reactions due to hindering the adsorption of water on the catalyst and shifting the thermodynamic equilibrium.

2.3. Methanol Synthesis Catalyst

Although it is well known that Cu/Zn based catalysts are the most catalytically active for the methanol synthesis, developing more active methanol synthesis catalysts operating at lower temperatures is the key to improve the methanol synthesis process (de Jong, 2009).

Copper is the active metal site for the methanol synthesis. However, catalysts containing only Cu metals were almost inactive (Kasatkin et al., 2007). The role of ZnO is the promoting and maintaining a high dispersion of Cu nanoparticles (de Jong, 2009). Industrial methanol synthesis catalysts consist of Cu/ZnO incorporated alumina catalysts with a surface area range of 60-100 m^2/g.

Reduction of the catalyst is required to obtain metallic Cu sites and it was reported that the reduction of CuO containing catalyst was completed at 200°C. It was also reported that Zn and Al metals remain as oxide forms after the reduction process (de Jong, 2009). The risk of sintering at high temperatures and favoring of low pressure reduction was also stated (de Jong, 2009).

2.4. Heteropoly Acids (HPA)

Heteropoly acids (HPA) are well-known for their strong Brønsted acidic nature therefore they are widely used as an acidic catalyst. More than 100 HPAs are available with different structure (Timofeeva, 2003).

Heteropoly acids are in crystal form and for the catalysis Keggin-type structures are preferred. They are represented by the formula of $XM_{12}O_{40}^{x-8}$ where X represents the central atom, x is the oxidation state and M is used for the metal ion. Center atom of the HPA typically is Si^{4+} or P^{5+}, whereas metal ion can be Mo^{6+}, W^{6+}, V^{5+}, Co^{2+}, Zn^{2+}, etc. The most common HPA types are silicotungstic acid (STA), tungstophosphoric acid (TPA) and molybdophosphoric acid (MPA). Order of acid strengths of these Keggin-type HPAs were reported as (Timofeeva, 2003; Varışlı, 2007);

18

TPA > STA >> MPA

The HPAs are very high soluble in polar solvents (Timofeeva, 2003; Varışlı, 2007).

2.4.1. Tungstophosphoric Acid (TPA)

It was reported that tungsten containing Keggin-type heteropoly acids showed remarkably high catalytic activity compared to other Keggin-type heteropoly acids. It was also reported that TPA was the most catalytically active HPA in the dehydration of isopropyl alcohol and it was also suitable for the methanol dehydration to methane. Figure 2.5 shows the Keggin-type structure of TPA.
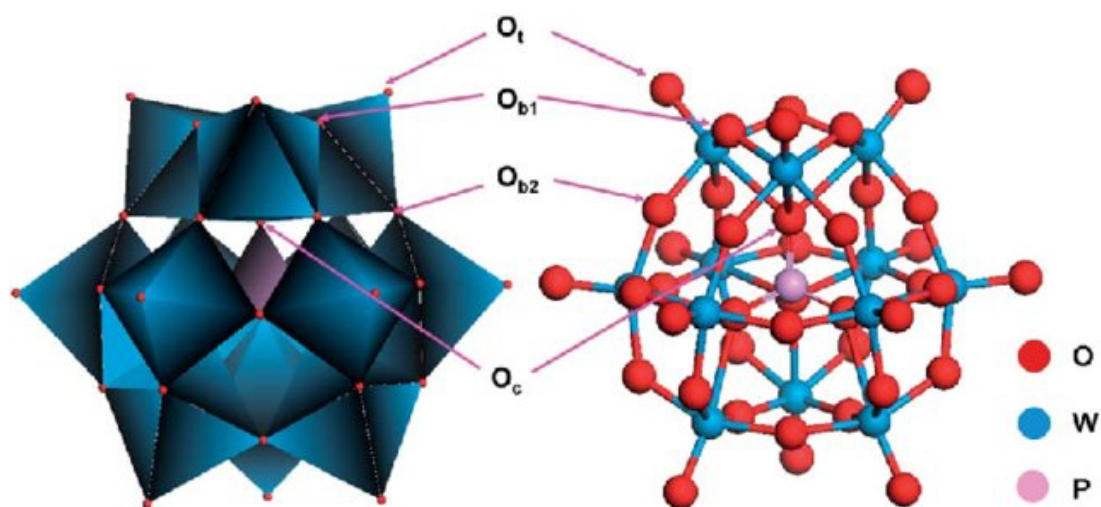
Figure 2.5. Keggin structure of TPA (Jiang, 2014)

However, the main drawback of TPA is its very low surface area and almost non-porous structure like other HPAs. Hence, the incorporation of TPA to a suitable support material is required to increase the surface area for heterogenous catalytic applications.

19

2.5. Catalyst Selection and Operating Condition in DME Production

Catalyst is the most important parameter that affects the performance of the reactions. Generally, commercial $Cu/ZnO/Al_2O_3$ and γ-Al_2O_3 solid catalysts are preferred for the methanol synthesis and methanol dehydration, respectively. Some examples of the catalysts used in the synthesis of DME in the literature are given as follows:

DME Development Co., Ltd, built a pilot plant with a liquid phase slurry reactor that produces 5 tons/day DME. Inlet feed composition was adjusted as H_2:CO ratio of 1:1 and operating conditions were 250°C, 50 bar with catalyst loading ratio to flow rate range of 3:1-8:1 (kgcatalyst.h/kgmole) (Ogawa et. al., 2004).

A theoretical analysis of fluidized bed for producing DME from syngas was carried out. The optimum temperature for CO conversion and DME productivity was given as 280-290°C. But it was stated that, to avoid thermodynamic limitations and catalyst deactivation, reactions should be operated at a temperature lower than 270°C (Lu et al., 2003).

Direct synthesis of DME from syngas requires bifunctional catalyst to accomplish the methanol formation and the methanol dehydration reactions in the same reactor. In the literature, mainly CuO and ZnO incorporated alumina based catalysts are used for this purpose (Lu et al., 2003; Moradi et al., 2011; Ng et al., 1999).

The direct synthesis of DME over a commercial $CuO/ZnO/Al_2O_3$ (methanol formation) and γ-alumina (methanol dehydration) catalysts at a temperature of 250°C and a pressure of 50 bar was investigated in an internal-recycle-type reactor. It was reported that increasing hydrogen in the feed, enhanced the methanol selectivity, whereas DME selectivity was decreased. Deactivation of catalyst caused by high space velocities and high dehydration catalyst loading was reported (Ng et al., 1999).

The thermodynamic analysis of the single-step DME synthesis from syngas over a bifunctional catalyst for different temperatures (200-240°C), pressures (20-50bar) and feed compositions (H_2:CO=1:1-2:1) was investigated. It was reported that using the

Soave–Redlich–Kwong (SRK) equation for the correction of non-ideal gas behavior was in good agreement with the experimental results. Physically mixed catalyst composed of $CuO/ZnO/Al_2O_3$ as a methanol synthesis catalyst and H-ZSM-5 as a methanol dehydration catalyst was used in the performance tests. Decrease in CO_2 selectivity with the increase in the H_2/CO ratio was also reported. About 95% CO conversion and 70% DME yield were obtained at temperature of 240°C and pressure of 50 bar under GHSV = 500 mL/(g-cat/h) with a H_2/CO ratio of 2. As the direct synthesis of DME was shifting the thermodynamic equilibrium, higher CO conversion and DME yield were observed (Moradi et al., 2011).

A lab scale fluidized bed reactor for producing DME from syngas over $Cu/ZnO/Al_2O_3$ and HZSM-5 catalyst was investigated. Catalytic activities were investigated for different temperatures and H_2/CO, and catalyst ratios. 40% CO conversion was obtained at 260°C temperature under 30 bar pressure with GHSV of 3000 ml/gcat.h and the H_2/CO ratio of 1/1. CO conversion was increased to approximately 50% under 40 bar pressure. It was mentioned that methanol synthesis was favored at high H_2/CO ratio, methanol dehydration, on the other hand, was favored at low H_2/CO ratio and the increase of H_2/CO ratio resulted in the accumulation of water and decreased DME selectivity finally. It was reported that, optimum $Cu/ZnO/Al_2O_3$:HZSM-5 ratio was found to be 5:1 between 250-270°C (Lu et al., 2004).

The catalytic performance of alumina impregnated SBA-15 and mesoporous aluminosilicate synthesized using one-pot hydrothermal method and a commercial catalyst in the dehydration of methanol to produce dimethyl ether was investigated. It was stated that alumina impregnated SBA-15, which has high Bronsted acidity, gave methanol conversion close to equilibrium and almost 100% DME yield at temperatures higher than 300°C (Tokay et al., 2012).

Tungstophosphoric acid incorporated silica structured mesoporous catalyst using one-pot hydrothermal synthesis procedure (TRC-W40) and MCM-41 catalysts (TPA@MCM-41) were investigated in the study of Çiftçi and co-workers. It was seen

that DME yield passed through a maximum at about 200°C in the presence of TPA@MCM-41 which has high Bronsted acidity. TRC-W40 was more stable and showed very good activity in the dehydration of methanol giving 100% DME selectivity at temperatures less than 300°C (Ciftci et al., 2012).

A study was carried out to investigate the activities of mesoporous nafion incorporated silica structured nanocomposite catalysts in the production of DME from the methanol dehydration reaction. Catalysts with a surface area range of 595 and 792 m^2/g showed Bronsted and Lewis acid sites as reported. Almost 100% selectivity of DME was achieved at temperatures higher than 180°C with this catalyst (Ciftci et al., 2010).

Developing a bifunctional catalyst, which is active and selective for DME to be used in the single-step DME synthesis from syngas is a challenging and getting attention in the recent years. Heteropolyacids are considered as one of the promising solid acid candidates in the literature due to their very strong Bronsted acidity, with very high proton mobility and good redox properties. They are considered as suitable catalysts for acid catalyzed reactions and selective oxidation reactions. On the other hand, mesoporous alumina and mesoporous carbon materials were considered to be suitable support material for their unique properties in order to use in the synthesis of bifunctional DME catalyst.

CHAPTER 3

THERMODYNAMIC ANALYSIS

Mainly four reaction take place in the single-step DME synthesis from syngas containing CO and H_2 mixture (R1, R2, R3, and R4).

$$CO + 2H_2 \leftrightarrow CH_3OH \qquad \Delta Hrxn = - 90 \text{ kJ/mol} \qquad (R1)$$

$$CO_2 + 3H_2 \leftrightarrow CH_3OH + H_2O \qquad \Delta Hrxn = - 49 \text{ kJ/mol} \qquad (R2)$$

$$2CH_3OH \leftrightarrow CH_3OCH_3 + H_2O \qquad \Delta Hrxn = - 25 \text{ kJ/mol} \qquad (R3)$$

$$CO + H_2O \leftrightarrow CO_2 + H_2 \qquad \Delta Hrxn = - 41 \text{ kJ/mol} \qquad (R4)$$

These reactions result in two overall direct DME synthesis reactions (R5 and R6).

$$3CO + 3H_2 \leftrightarrow CH_3OCH_3 + CO_2 \qquad \Delta Hrxn = - 246 \text{ kJ/mol} \qquad (R5)$$

$$2CO + 4H_2 \leftrightarrow CH_3OCH_3 + H_2O \qquad \Delta Hrxn = - 205 \text{ kJ/mol} \qquad (R6)$$

Methanol reactors and single-step DME reactors are conventionally operated at medium temperature and elevated pressure due to thermodynamic limitation of methanol formation reaction. Methanol formation and dehydration of methanol to DME are consequent reactions. Therefore, during the single-step DME synthesis, methanol is produced first and then it is consumed in the methanol dehydration. Hence, consumption of methanol shifts the thermodynamic equilibrium toward higher CO conversion. Therefore, compared to the two-step DME synthesis process, the direct process allows a higher CO conversion and a simple reactor design that results in much lower DME production (Azizi et al., 2014; Lu et al., 2004).

All of the reactions are exothermic, thus DME synthesis is favored at lower temperatures because the side product and coke formation are significant at high temperatures (Azizi et al., 2014). However, low reaction rates and low activity of

catalyst at low reaction temperatures require to determine optimum reactor operating conditions.

Typical range of operating conditions for the single-step DME reactors are usually between 240-300°C and 30-70 bar (Lu et al., 2004; Ogawa et al., 2004). Optimum reactor operating conditions are reported as 250-275°C, 50 bar in the literature (Ng et al., 1999; Ogawa et al., 2004).

In order to determine the operating conditions of the reactor, thermodynamic analysis of the reactions in the synthesis of DME is very important. Thermodynamic equilibrium calculations were carried out using ASPEN HYSYS software with Gibbs Reactor model. Different equation of states (EOS), can be described in Aspen since the gases are actually not ideal. Therefore, SRK EOS was chosen in Aspen to consider fugacity coefficients. All components involved in the reactions were introduced to the software and different case studies have been performed. A sample equilibrium conversion calculation for the methanol synthesis is given in Appendix A.

CO equilibrium conversions for methanol synthesis and the single-step DME synthesis cases were plotted separately in Figure 3.1. It is clearly seen that single-step DME synthesis increases significantly CO equilibrium conversion. This phenomena is called the synergic effect of the reaction.
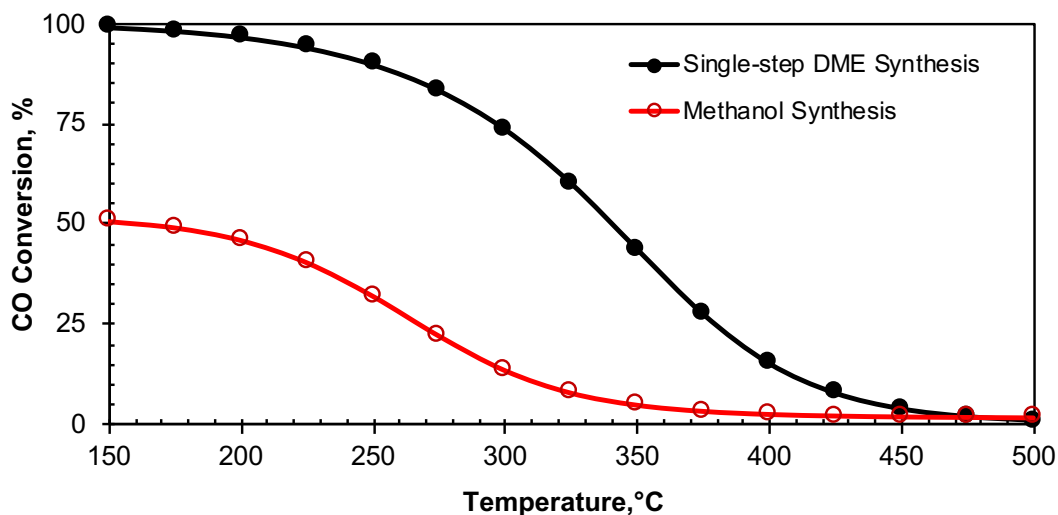
Figure 3.1. Comparison of CO equilibrium conversion for methanol and the direct DME syntheses (P: 50 bar, H_2/CO= 1/1,) (Filled symbols: the single-step DME synthesis and empty red symbols: methanol synthesis)

Effect of the reaction pressure and temperature on CO equilibrium conversion was investigated for molar H_2:CO ratio of 1:1 and presented in Figure 3.2. Increasing reaction pressure causes an increase in equilibrium conversion due to stoichiometric situation of the reactions. Increasing the reaction pressure shifts the overall reaction to the product sides, which increases the conversion because of the Le Chatelier principle. Hence, operating at high pressure is favored for the synthesis of DME from syngas to eliminate the thermodynamic limitations. The increase in conversion from 50 bar to 75 bar is very small compared to the increase in conversion from 30 bar to 50 bar at operating temperature range of 200-300°C. On the other hand, 75 bar is a very high pressure and it does not only increase the operating cost, but also it can lead to more operational risks. Therefore, operating pressure was chosen as 50 bar in the experiments.
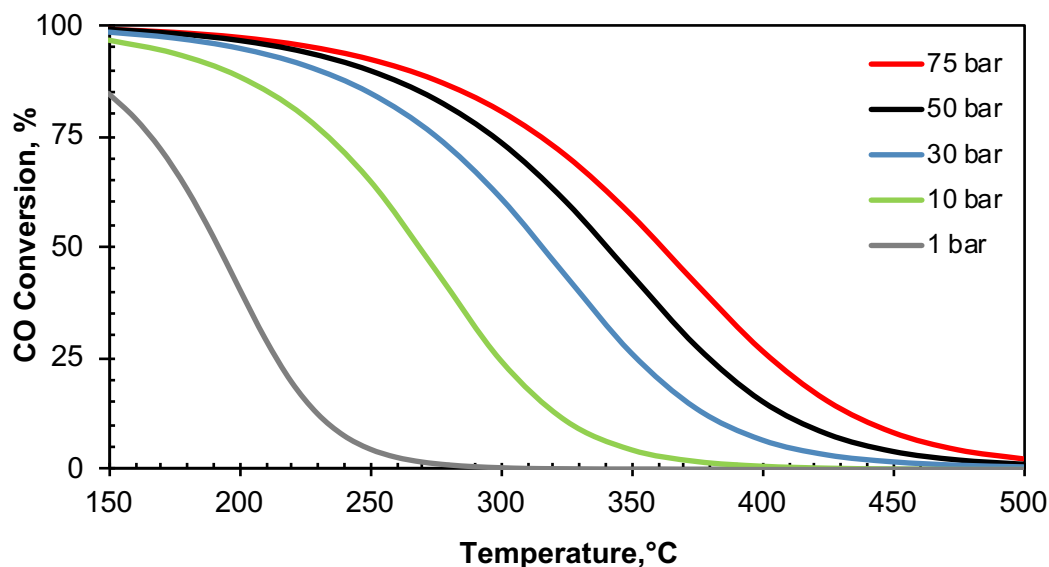
Figure 3.2. Effect of pressure on CO equilibrium conversion

According to the literature survey, thermodynamic analysis of reactions showed that besides temperature and pressure, feed composition is also important. The reactor performance is very sensitive to the molar CO:H_2 ratio (Peng et al., 1999). While the stoichiometric CO:H_2 ratio of 1:1 gives maximum equilibrium conversion for the R5 reaction, this ratio is 1:2 for R6 reaction (Azizi et al., 2014; Peng et al., 1999). In this scope, the effect of feed composition on equilibrium conversion was investigated and presented in Figure 3.3. According to these results, CO equilibrium conversion shows increasing trend with an increase in H_2:CO ratio in the feed up to 2:1 ratio. However, further H_2:CO ratio increase in the reactant mixture does not affect significantly CO equilibrium conversion after the CO:H_2 ratio of 1:2.
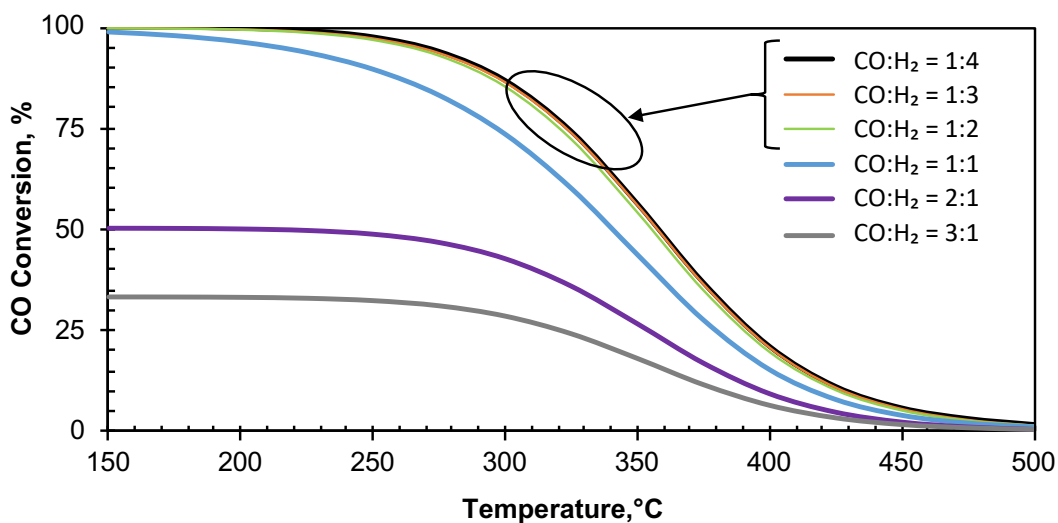
Figure 3.3. Effect of molar $CO:H_2$ feed ratio on CO equilibrium conversion at 50 bar

In addition, considering the high hydrogen prices, determination of the optimum $CO:H_2$ ratio is important in terms of DME production feasibility. Therefore, DME equilibrium mole fractions at reactor effluent and CO conversions for various $CO:H_2$ ratios were compared in Figure 3.4. It is clearly seen that an increase in $H_2:CO$ ratio favors more CO conversion. However, DME equilibrium mole fraction gives a maximum for $H_2:CO$ ratio of 1:1. This thermodynamic study indicates that maximum DME mole fraction can be obtained with a $CO:H_2$ ratio of 1:1.
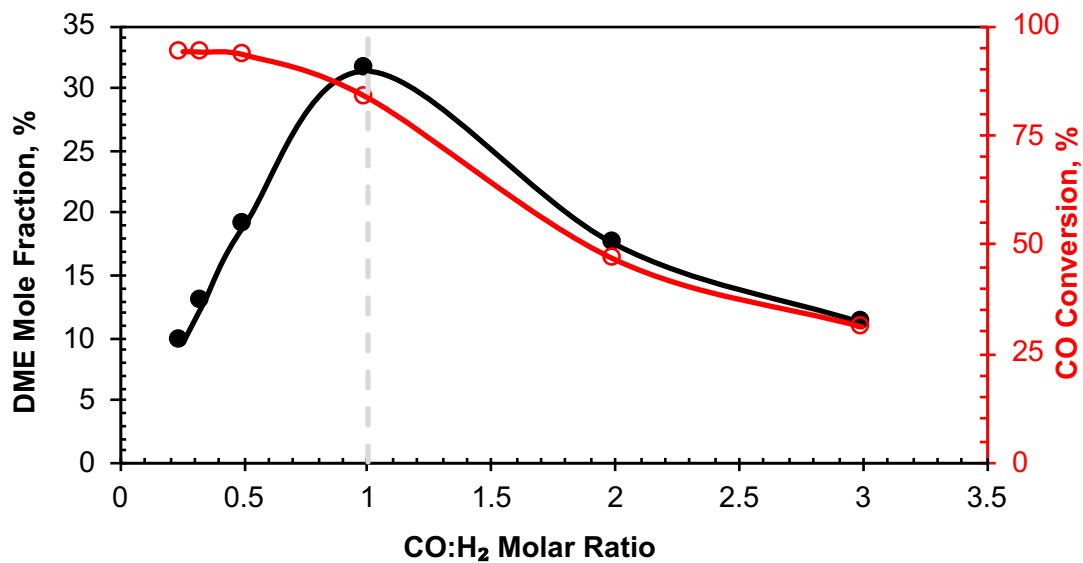
Figure 3.4. Effect of molar CO:H_2 ratio on DME equilibrium mole fraction and CO equilibrium conversion (P: 50 bar, T: 275°C, Filled symbols: DME equilibrium mole fraction, empty symbols: CO equilibrium conversion)

Gasification of coal and other hydrocarbons yields a composition of mainly CO, H_2 and CO_2 (Yates & Lettieri, 2016). In Figure 3.5, total equilibrium conversion (CO & CO_2) is presented for different CO_2/CO/H_2 ratios. Total equilibrium conversion is in inversely proportional to the CO_2 content in the syngas mixture.
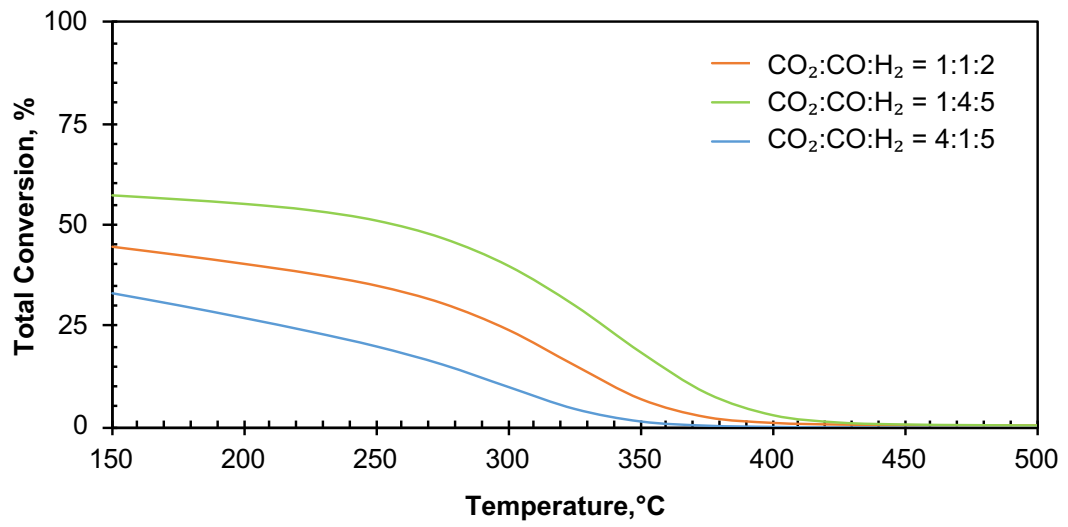
Figure 3.5. Effect of CO_2 composition in syngas on total conversion

It can be seen in Figure 3.6 that, similar to $CO+CO_2$ conversion, DME equilibrium mole fraction also decreases with an increase of CO_2 content in the reactant mixture.
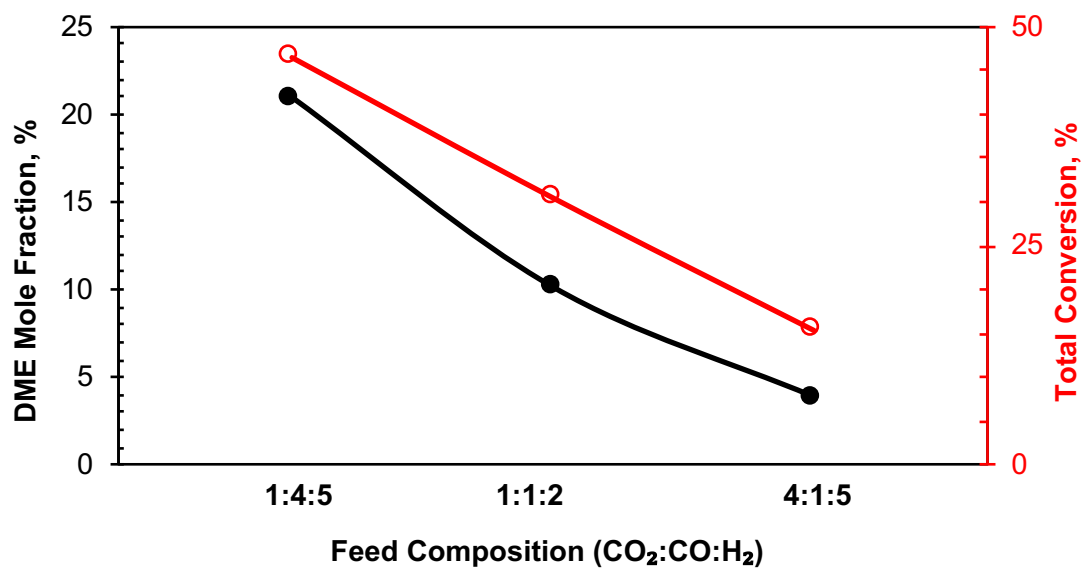
Figure 3.6. Effect of CO_2 composition in syngas on DME equilibrium mole fraction and total equilibrium conversion (P: 50 bar, T: 275°C, Filled symbols: DME equilibrium fraction, empty symbols: total equilibrium conversion)

CHAPTER 4

EXPERIMENTAL

Experimental studies were conducted in two parts: synthesis and characterization of the catalysts and catalyst performance tests on DME production. DME production system was constructed in Chemical Reaction Engineering Laboratory of METU.

4.1. Chemicals Used in the Study

Chemicals and gases, which were used in catalyst synthesis and reaction system are given in Table 4.1.

Table 4.1. *Chemicals used in this study*

Name	Chemical Formula	Purity (%)	Company
Pluronic P-123,	$EO_{20}PO_{70}EO_{20}$,	-	Sigma-Aldrich
Ethanol	C_2H_5OH	≥99.5	Merck
Nitric acid	HNO_3	65	Merck
Sulfuric acid	H_2SO_4	95-98	Merck
Hydrochloric acid	HCl	37	Merck
Aluminum Isopropoxide	$C_9H_{21}AlO_3$	≥98.0	Merck
Crystal Sugar	$C_{12}H_{22}O_{11}$	-	Torku
Copper(II) nitrate trihydrate	$Cu(NO_3)_2.3H_2O$	≥99.5	Merck
Zinc nitrate tetrahydrate	$Zn(NO_3)_2.4H2O$	-	Merck
Tungstophosphoric acid (TPA)	$H_3PW_{12}O_{40}$	-	Acros
Air	-	-	Oksan
Helium	He	99.9999	AirProducts
H_2 – Ar mixture	H_2-Ar	5	Linde
NH_3 – Helium mixture	NH_3-He	5	Oksan
Argon	Ar	99.99	Oksan
Carbon monoxide	CO	99.99	Oksan
Carbon dioxide	CO_2	99.995	AirProducts
Hydrogen	H_2	99.999	Habaş
Dimethyl ether (DME)	C_2H_6O	99.9	Linde

4.2. Synthesis of Catalysts

Synthesis of the catalysts can be divided into two parts; synthesis of support materials and metal loading to the support. Two different support materials, mesoporous alumina and mesoporous carbon, were synthesized. For the metal loading, impregnation and one-pot methods were used.

4.2.1. Synthesis of Mesoporous Alumina (EMA)

Synthesis of mesoporous alumina was carried out using Evaporation Induced Self-Assembly (EISA) method based on Yuan and coworker's study (Yuan et al., 2008). In this synthesis method, pluronic P-123 as surfactant, aluminum isopropoxide as metal salt source and ethanol as solvent were used. EISA synthesis method involves four main steps which are the preparation of synthesis solution, hydrolysis, drying and calcination, respectively. Representation of this method can be found in Figure 4.1.
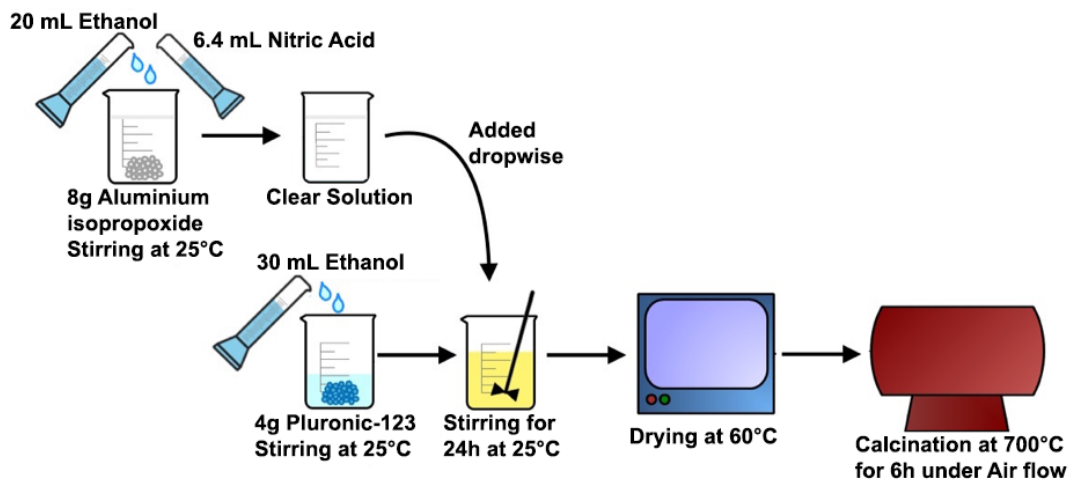
Figure 4.1. Synthesis of mesoporous alumina using EISA method.

The synthesis steps in EISA method were as follows: Firstly, Pluronic-123 was dissolved in ethanol and mixed at 275 rpm and room temperature in order to obtain homogenous solution. On the other side, aluminum isopropoxide, ethanol and nitric acid were mixed in the beaker and added to the pluronic-123 solution dropwise. Then final solution was mixed at 275 rpm and room temperature for 24 hours. After that, it was dried in a furnace at 60°C for 48h. After drying step, calcination process was conducted under dry air flow, at two different temperatures (700°C and 800°C) for 6 hours with a ramp of 1°C/min. At the end of calcination, pale yellow solid samples turned to white powder and mesoporous alumina was produced. Catalysts that were synthesized using this method were named EMA.

4.2.2. Synthesis of Mesoporous Carbon (CMK-3)

Mesoporous carbon (CMK-3) was synthesized using a nanocasting technique. In this procedure, ordered porous inorganic material SBA-15 was used as a template. SBA-15 was synthesized according to the recipe reported by Zhao (1998). Synthesis procedure was as follows: 8g surfactant P-123 was dissolved in 250 ml deionized water (DI) while it was stirred and 25 ml HCl (38%) was added dropwise. HCl addition helped to obtain a clean solution. After this step, pH should be less than 1.0. Dissolving of surfactant followed by addition of silica source. Therefore, 16.4 ml TEOS was added dropwise to this solution while it was stirred. The addition of TEOS turned transparent solution into white mixture. The mixture was kept at 40°C for 38 minutes. Then it was kept at 90°C and atmospheric pressure for 24 hours for hydrothermal treatment. White colored slurry was washed and filtered with DI until the pH of the solution reached 7.0. The sample finally dried overnight at room temperature and calcined at 600°C for 6 hours under airflow with a heating rate of 1°C/min.

Then sucrose as a carbon precursor was impregnated on SBA-15 in the synthesis of mesoporous carbon.

CMK-3 synthesis procedure was as follows: In the first step, impregnation of carbon source was carried out. Initially, powder sucrose was dissolved in deionized water at room temperature. Then, sulfuric acid was added dropwise to this solution while it was stirred. The solution was kept stirred and SBA-15, which was in powder form was added piecemeal to this solution. For the final slurry mixture, the mass ratio of SBA-15/sucrose/sulfuric acid/water was kept as 1/1.3/0.14/5. This mass ratio was used for 1g of SBA-15. The mixture was stirred for 1h at room temperature. The second step was the drying and carbon formation processes. The mixture was dried in an oven at 100°C for 6h then temperature was increased to 160°C and kept for 6h. White colored mixture turned to dark brown composite after this step. The first and the second steps were repeated to be sure that all carbons were placed into the pores of material. Therefore, dark brown material was crushed and added piecemeal to sucrose, sulfuric acid and water solution which had a mass ratio of 0.8/0.09/5, respectively. Then mixture was treated at the same drying and carbon formation conditions. Resulting composite was crushed to obtain a powder form. Then, the material was pyrolyzed at 900°C in tubular furnace with heating rate of 5°C/min under inert atmosphere with a flow rate of 120 ml/min for 6 h. Finally, the mesoporous carbon was recovered by leaching the silica based SBA-15 template with 1M NaOH solution (50 vol% ethanol-50 vol% water), filtered washed with boiling ethanol until pH=7 and dried at 120°C for 4h. Hence, dark black mesoporous carbon, CMK-3 powder was obtained.

During the filtration "MN 640 de" grade (very slow filtration for extremely fine precipitates) filter paper was used to increase the contact time. Washing was carried out with absolute ethanol due to the hydrophobic nature of the material. Boiling ethanol was used to remove NaOH and prevent its adsorption on the material.

4.2.3. TPA Loading on Mesoporous Alumina

For the loading of TPA heteropolyacid to the structure of mesoporous alumina, two different methods were used, which were namely impregnation and one-pot synthesis. These synthesis methods were described in detail below.

Impregnation method

Impregnation of TPA to the mesoporous alumina support material was shown in Figure 4.2. TPA impregnation method was as follows: a certain amount of TPA was dissolved in 10 mL deionized water at room temperature. On the other side, 1g EMA support was homogenously stirred in 15 mL deionized water at room temperature. Clear TPA solution was added dropwise to EMA mixture and the final solution was stirred at 30°C for 24h to obtain homogenized TPA distribution. Consequently, the solution was dried at 60°C and calcined at 280°C under air flow for 6 hours with 1°C/min temperature ramp.
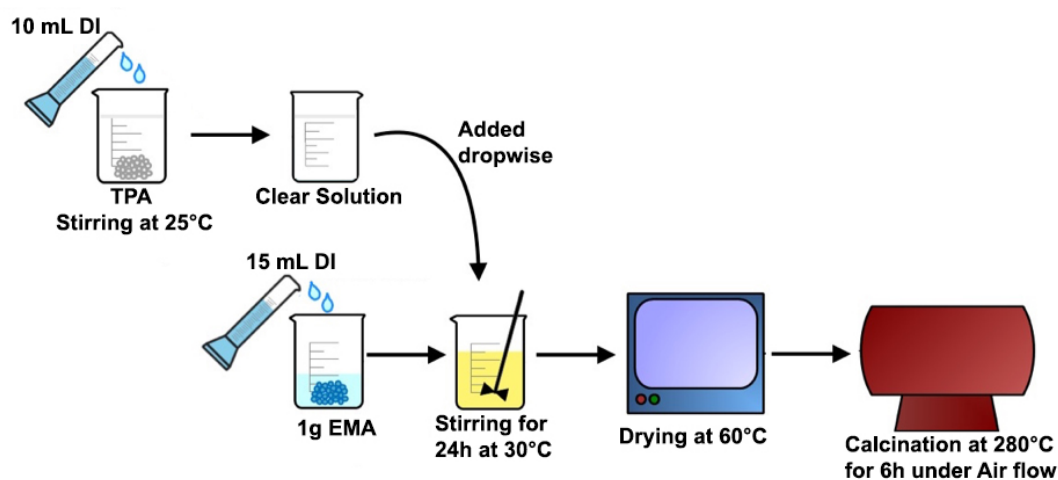
Figure 4.2. TPA loading on EMA support using impregnation method.

One-pot method

In the case of one-pot loading method, TPA was directly loaded to the structure during the synthesis of mesoporous alumina. One-pot TPA loaded EMA synthesis procedure had the similar synthesis steps as the EMA synthesis procedure as described in Section 4.2.1, a certain amount of TPA was dissolved in ethanol until a clear solution was obtained. Then, this TPA solution was added dropwise to pluronic P-123 solution simultaneously while aluminum isopropoxide solution was added during the synthesis of EMA. Rest of the synthesis procedure was same as the synthesis of EMA except the calcination temperature. After the loading of TPA to the alumina structure, calcination was carried out under dry air flow at 280°C for 6 hours with 1°C/min temperature ramp. TPA loading using one-pot method is shown in Figure 4.3.
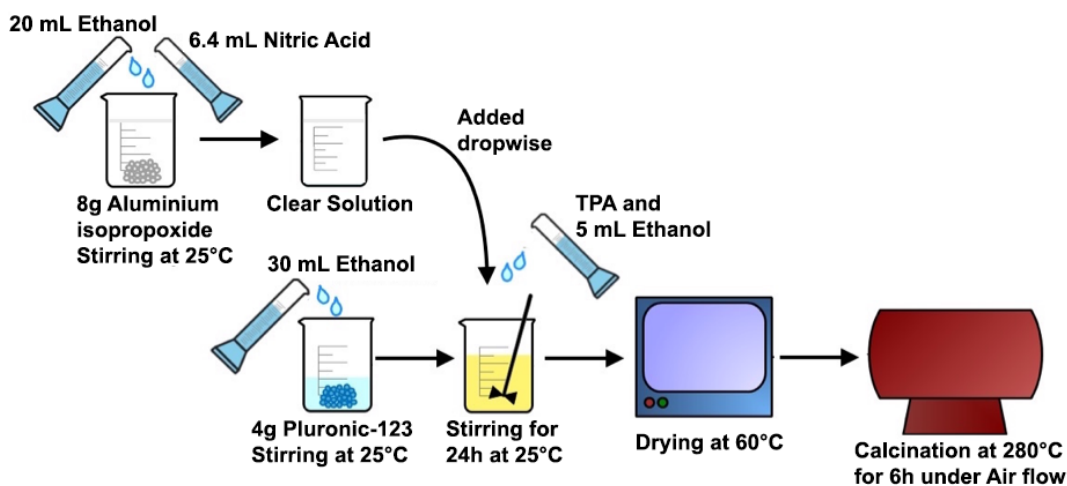
Figure 4.3. TPA loading on EMA using one-pot method.

4.2.4. Synthesis of Bifunctional DME Synthesis Catalysts

Use of Cu-Zn based catalyst for methanol synthesis and acidic catalyst for methanol dehydration to produce DME is common. However, the main challenge in the single-step DME synthesis is to design and synthesize bifunctional catalyst with the highest

activity and less side reactions. TPA and Cu-Zn containing bifunctional DME catalysts were synthesized using two different supports: EMA and CMK-3.

Bifunctional catalysts were synthesized using the impregnation method. The procedure was as follows: 1g of support was stirred in 15ml ethanol. Two stock solutions of Cu and Zn were prepared by dissolving $Cu(NO_3)_2.3H_2O$ and $Zn(NO_3)_2.4H_2O$ salts in 10 ml ethanol in two separate beaker. All solutions were stirred for 1h at 30°C. The stock solutions were added dropwise simultaneously to support mixture. Then clear solution of TPA dissolved in 10 ml ethanol was added dropwise to this mixture. Support/Cu/Zn/TPA mass ratio was kept as 0.27/0.28/0.21/0.25. Final mixture was stirred in ultra-sonic bath to ensure that the metals were well dispersed for 2 h at 30°C. The mixture was aged at 30°C water bath for 47 h and then calcined at 280°C for 6 h under He gas with a heating rate of 1°C/min. In order to prevent sintering of copper, calcination temperature did not exceed 280°C and helium was used instead of air since CMK-3 support has a carbonaceous structure.

4.2.5. Naming of the Catalysts

In the scope of this study, two different mesoporous alumina supports were used as methanol dehydration catalyst due to its acidic structure. Synthesized mesoporous alumina and commercial γ-alumina supports were named EMA and CA, respectively. Mesoporous carbon was also used as a support in the bifunctional DME synthesis catalyst and named CMK-3.

For the methanol synthesis reaction catalyst, a commercial methanol synthesis catalyst was used and named MSC.

TPA was loaded on these catalysts with different methods and different weight percentages. For the metal loaded with impregnation method, "@" symbol was used and for the metal loaded using one-pot method, "/" symbol was used in the naming. These synthesized catalysts were named in the following format XTPA@Y or XTPA/Y, where X indicates the TPA wt. % loaded on support and Y stands for support

type. For instance, 5 wt. % TPA impregnated mesoporous alumina was named as 5TPA@EMA. All the catalyst which were synthesized or used are listed in Table 4.2.

Table 4.2. *List of catalysts used in the DME production*

Name of Catalyst	Content (wt. %)			Description
	TPA	Cu	Zn	
MSC	-	35	20.7	Commercial methanol synthesis catalyst
CA	-	-	-	Commercial γ-alumina
EMA	-	-	-	Synthesized mesoporous alumina calcined at 700°C
EMA800	-	-	-	Synthesized mesoporous alumina calcined at 800°C
5TPA/EMA	5	-	-	One-pot TPA loaded mesoporous alumina
10TPA/EMA	10	-	-	
25TPA/EMA	25	-	-	
5TPA@EMA	5	-	-	TPA impregnated mesoporous alumina
10TPA@EMA	10	-	-	
25TPA@EMA	25	-	-	
TPA@Cu-Zn@EMA	25	28	20	TPA and Cu-Zn loaded mesoporous alumina
TPA@Cu-Zn@CMK-3				TPA and Cu-Zn loaded mesoporous carbon

4.3. Material Characterization

All synthesized materials were characterized with different techniques, in order to get information about crystal structure, elemental composition, pore size and volume, surface area, acid capacity, reducibility etc. Analysis methods were developed in TPD, TPR, BET techniques.

4.3.1. X-Ray Diffraction (XRD)

X-ray diffraction is mainly used to obtain information about crystal structure of materials, crystal size and unit cell. $CuK_{\alpha 1}$ radiation was used in analyses with a scanning rate of 0.2°/min between 5-90°. X-Ray was charged with 40 kV and 30 mA. Rigaku Ultima-IV diffractometer device at METU Central Laboratory was used to obtain XRD patterns.

4.3.2. Nitrogen Physisorption

Nitrogen physisorption analysis is widely used to determine porosity, pore size distribution, pore structure, surface area and pore volume of a variety of different solid materials. Analysis was carried out at 77K temperature with different nitrogen relative pressure ranges. Surface area was calculated from the monolayer capacity using Brunauer, Emmett and Teller (BET) theory between 0.05-0.3 P/P_o. Pore volume and pore size distribution were evaluated using Barrett, Joyner and Halenda (BJH) theory using desorption isotherms. All samples were dried and degassed before the analysis at 110°C for 4 hours at vacuum conditions. During the analyses, relative pressure range (P/P_o) was taken between $1x10^{-5}$ and 0.99. All analyses were performed using Micromeritics Tristar II 3020 at Chemical Engineering Department of METU.

4.3.3. Scanning Electron Microscopy and Energy Dispersed X-Ray (SEM-EDX)

SEM image helps to observe surface morphology and surface topology of the materials by collecting low-energy secondary electrons, which are inelastically ejected from material under electron beam. EDX analysis gives the information about the elemental content of the sample using the X-ray energy, which is unique for the element. Backscattering image is obtained by collecting high-energy electrons, which are elastically backscattered out of the material atom under electron beam. Backscattered electrons of samples with high atomic number are stronger than that of samples with low atomic number. Sample with the high atomic number gives a brighter image. This contrast difference helps to detect dispersion of the elements on the sample.

Each sample was hold on carbon adhesive tape and then coated with palladium and gold in order to prevent the charging of the samples under electron beam. Conventionally SEM-EDX analyses were carried out at vacuum conditions, in order to minimize scattering of the electrons with air and increase the intensity of signals. SEM imaging and Energy Dispersed X-ray analyses were performed using QUANTA

400F Field emission high resolution scanning electron microscope with 20 kV or 30 kV beam voltage and a resolution of 1.2 nm at METU Central Laboratory.

4.3.4. Thermal Gravimetric Analysis (TGA)

TGA provides information about the thermal stability of material and its volatile and combustible component fraction. Weight change of a material is monitored with respect to temperature with a heating ramp program under air or inert gas flow. Analyses were carried out with Shimadzu DTG-60H device at METU Chemical Engineering. Each sample was heated to 900°C with a heating rate of 5°C/min under 60 cc/min dry air or nitrogen flow.

4.3.5. Temperature Programmed Desorption (TPD)

The characterization of acidic nature of the materials was performed by NH_3-TPD. Ammonia, which is a basic gas chemisorbs on the acid sites of the materials. NH_3-TPD is based on monitoring desorption of adsorbed ammonia in a programmed temperature ramping of the sample. This analysis is widely used for characterization of site densities and acid capacities in solid acids. Conventionally this analysis is conducted by two method; either using ultra high vacuum chamber (UHV) at 10^{-9} torr coupled with temperature controller and quadrupole mass spectrometry (MS) (Figure 4.4a) or under a flow set-up inside in an oven followed by a TCD detector (Figure 4.4b).
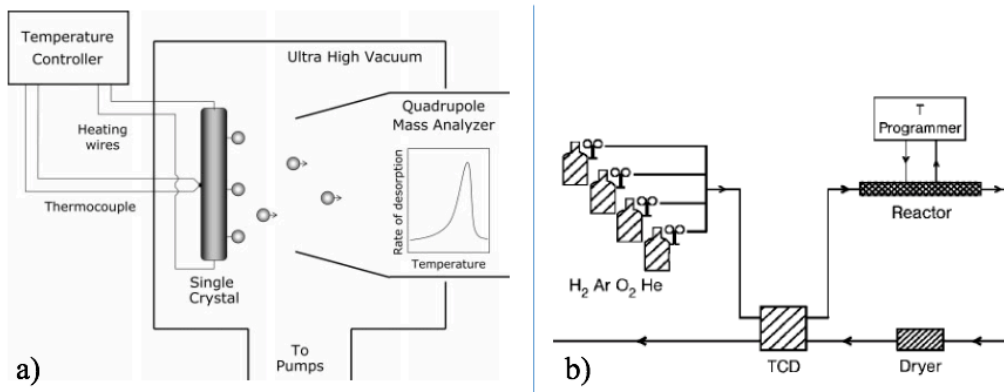
Figure 4.4. TPD set-up a) UHV chamber coupled with MS b) flow set-up coupled with TCD (adapted from (Niemantsverdriet, 2007))

Desorption of adsorbed probe molecules obeys Polanyi-Wigner Equation (3.*1*).

$$R_d = -\frac{d\theta}{dT} = \frac{v}{\beta} \theta^n \, e^{\left(\frac{-E_{des}}{RT}\right)}$$

(3.1)

where R_d, T, β, θ, E_{des} and R correspond to rate of desorption, temperature, heating rate, coverage, activation energy of desorption and gas constant, respectively.

In this study, TPD analyses were carried out in a flow set-up. In preparation process, initially each sample was dried for one hour at 280°C under 50 ml/min He flow, then samples were cooled and saturated for one hour with 5% NH_3 – 95% He (v/v) mixture with a flow rate of 50 ml/min at room temperature. Samples were then heated to 125°C with 20°C/min heating rate under 30ml/min He flow and waited at that temperature for 30 minutes to complete physical desorption. Finally samples were heated from 125°C to 600°C temperature with 10°C/min heating rate under 30ml/min He flow resulting an ammonia desorption curve.

Area under TDP curves is proportional to the quantitatively adsorbate coverage, which corresponds to acid capacity. Hence, in order to calculate the ammonia released by the material during TPD, ammonia calibration was carried out and a calibration curve was obtained using two different methods.

In the first method, a gas sampling bulb was first purged and then filled with gas mixture containing 5% NH_3 – 95% He (v/v) obtained from gas cylinder. This gas mixture was manually injected with a syringe to the TPD system with different amounts. During the injection, the TPD system was running under He flow without any solid sample.

In the second method, ammonia evaporation set-up was built (Figure 4.5). Concentrated ammonia solution (32% v/v) in the volumetric flask with condenser was heated to 40°C using a water bath and gaseous ammonia was collected in a gas sampler bulb. Circulating cooling water at 2°C was used in back condenser to condensate the water vapor. Gas washing bottle was also used after the condenser to adsorb water vapor, if available. Initially inlet and outlet valves of the sampling bulb were opened. Ammonia passed through the sampling bulb for 5 minutes before collecting ammonia to purge the impurities inside the sampling bulb. Then the outlet valve was closed and ammonia gas was collected inside the sampling bulb. Collected ammonia was manually injected with a syringe to the TPD system with different amounts. During the injection, the TPD system was running under He flow without any solid sample. Peak areas versus ammonia amounts were plotted. Hereby, calibration curve was obtained. Calibration curve is given in Appendix B. NH_3-TPD analyses were carried out at Chemical Reaction Engineering laboratory of METU using Micromeritics TPx Chemisorption 2720 equipped with a TCD.
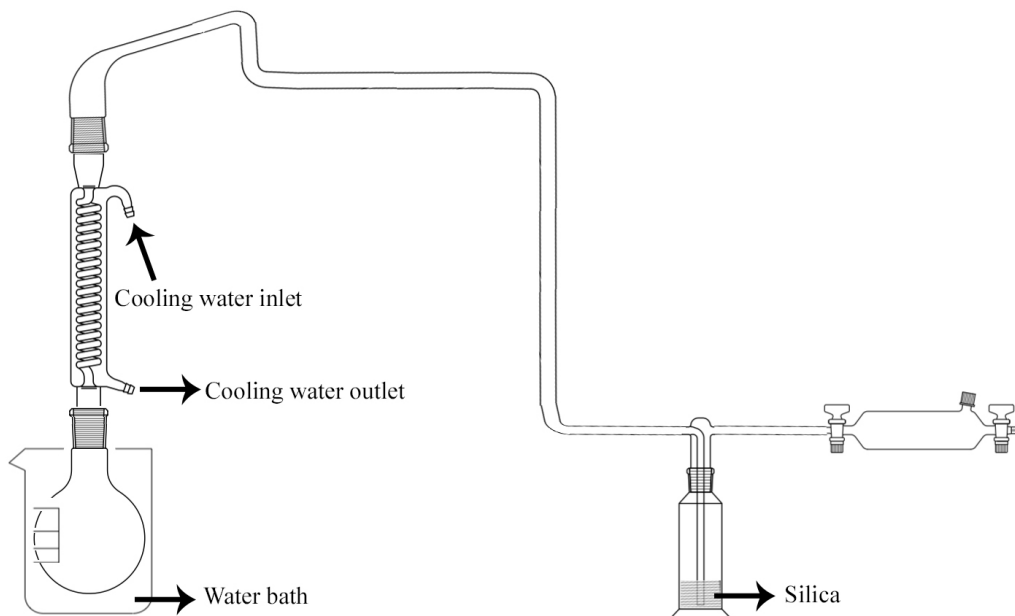
Figure 4.5. Ammonia purification set-up used in ammonia calibration

4.3.6. Temperature Programmed Reduction (TPR)

TPR is used to determine reduction temperature and reduction behavior of the metal loaded materials under hydrogen flow while monitoring the hydrogen consumption against temperature change. TPR analyses were performed at Chemical Reaction Engineering Laboratory of METU using Micromeritics TPx Chemisorption 2720 and hydrogen consumption was monitored using TC detector. The dried samples were first placed into the quartz tube in the system. Then the samples were heated to 300°C with a heating rate of 5°C/min under 50ml/min 5% H_2 and 95% Ar (v/v) gas mixture flow, hydrogen consumption curve was obtained. Each peak on the pictogram corresponds to reduction temperature of a metal, that is present in the sample.

4.4. DME Production System

High pressure, continuous flow lab-scale DME production set-up has been constructed in Chemical Reaction Engineering Laboratory of METU in order to test the activity of catalysts (Figure 4.6). 316 stainless steel with a diameter of ¼ inch was selected as a construction material in all tubing, valves and fittings. ¼ inch tubular reactor with a length of 60 cm was also made of stainless steel. Valves and fittings were selected to be compatible with the desired pressure and temperature. Four mass flow controllers (MFC) were calibrated for H_2, Ar, CO and CO_2 gases. Before each MFC, one pressure gauge was placed to measure the inlet pressure of each gas. System pressure is measured using a pressure gauge placed after the feed section (interconnection of MFCs).

Prior to be used in DME production system, each MFC was calibrated to adjust the desired flow rate. Two additional lines were constructed to be able to bypass feed section (MFCs) and reactor for pressurizing the system at the beginning of the operation. Reactor bypass system enables the pressurizing the reactor inlet and outlet streams simultaneously to prevent catalyst from moving in the reactor due to the sudden pressure changes. Reactor bypass line was also used to depressurize the system after the experiments. A vent line was constructed between the pressure gauges and MFCs to be able to depressurize each line after the experiment. Check valves having a cracking pressure of 1/3 psi were placed after each MFC and MFC bypass line to prevent backflow when a line had a lower pressure than the downstream pressure. However, it was important to underline that check valves were not considered reliable. System was equipped with a pressure relief valve (RV or pressure safety valve; PSV), which was set manually to 55 bar pressure to limit the pressure in the system.

System pressure and flow rate of gases were set using a metering valve and MFCs, respectively. Flow rate in the system was measured at the outlet using a soap bubble meter set-up.

A detailed leaking test procedure was applied in the system. After the installation of each line and valves, leaking test was performed gradually up to 55 bar pressure over

night to ensure that there was no leak in the system. Before the real feed testing, argon was used in the leak test due to the safety precautions. After leak test was completed, heating tapes and thermocouples (TC) were installed on the lines. Heating tapes and K-type thermocouples were equipped with a temperature controller. One heating system, which consists of heating band, TC and temperature controller was used per each section (pre-heating section and post-heating). Hence, temperature of each section can be independently controlled. Tubular reactor was placed in a tubular furnace to control the reaction temperature.

Argon gas was not only used in leak test, but also used to purge the lines after the experiments. A gas washing bottle was placed at the outlet of GC and it has multiple features. Methanol, water and trace amount of ethanol and formic acid were produced in the catalyst performance tests. This washing bottle was used as both gas scrubber and knockout drum before venting the flow to the atmosphere. By doing so, reactor effluent was cooled and liquid products were condensed and separated in this bottle to prevent any clogging in the vent line. It also indicated the existence of flow in the GC while bubbling in the liquid level.

Analyses of reactor effluent stream were performed continuously using Gas Chromatography (GC, Varian CP3800) with Porapak Q packed column and thermal conductivity detector (TCD). As a carrier gas in GC, argon was selected.
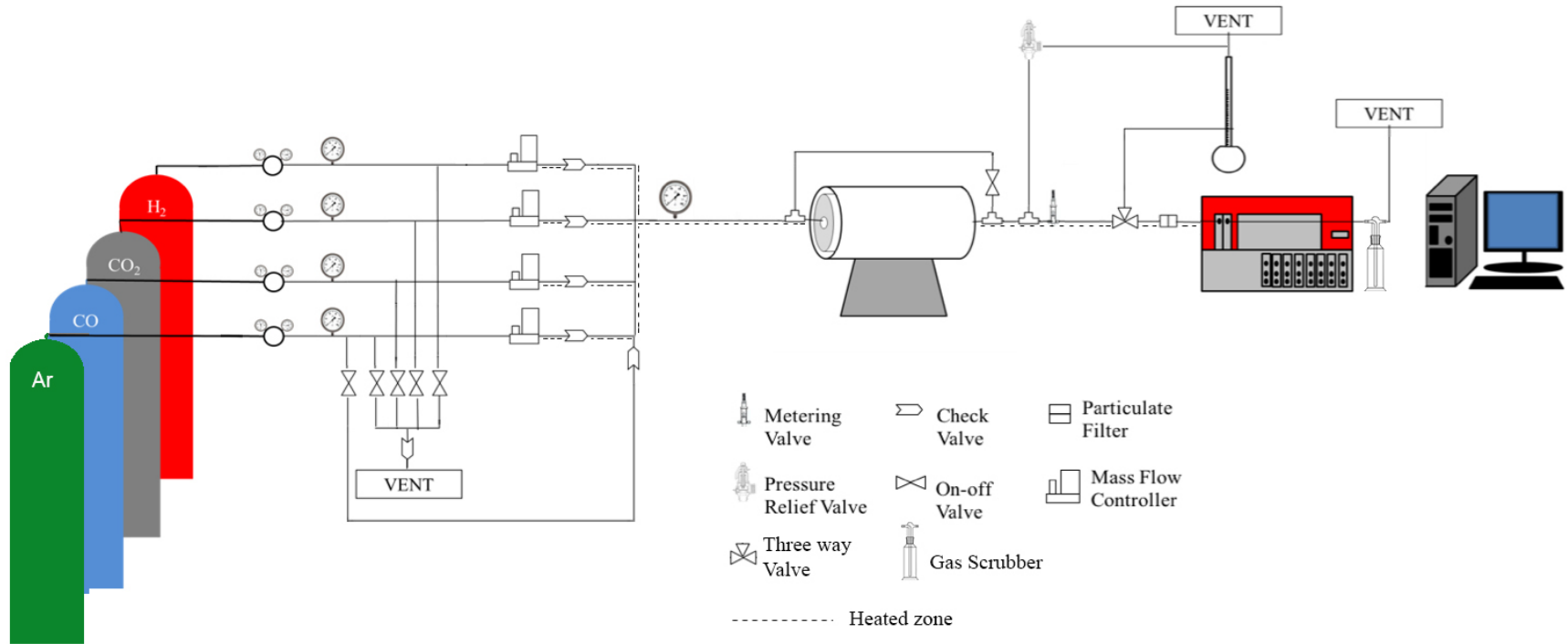
Figure 4.6. DME Production system

An analysis method with temperature ramping program was created and optimized, in order to have fast analysis, effective separation and to be able to carry out analyses in gas phase. Therefore, liquid product analysis was not required and all the reactor effluent was analyzed in gas phase. The GC analysis condition and column temperature program are given in Table 4.3 and Table 4.4. Products and reactants in the reactor effluent stream are presented in Table 4.5.

Table 4.3. *GC analysis condition*

	Temperature (°C)	Pressure (psi)	Flow (ml/min)	Carrier gas
TCD	200	-	30	Ar
Column	38-170*	5	-	Ar

*Detailed temperature program given in Table 4.4

Table 4.4. *GC Column temperature program*

Temperature (°C)	Hold duration (min)	Heating rate (°C/min)
38	6	-
120	1	4
130	0.1	1
170	0.4	20

Table 4.5. *Reactant and product identification*

Reactants	Products
Carbon monoxide (CO)	Methane (CH_4)
Hydrogen (H_2)	Carbon dioxide (CO_2)
Carbon dioxide (CO_2)	Formic acid (HCOOH, FA)
	Methanol (CH_3OH, MeOH)
	Dimethyl-ether (CH_3OCH_3, DME)
	Ethanol (C_2H_6O, EtOH)

In order to identify the retention time of the peaks in chromatogram, initially, calibration had to be performed. For this purpose, calibration of products and reactants was carried out in several techniques to ensure that the calibration factors were correct and calibration line was in still linear region.

In these calculations, calibration factor of CO was accepted as 1 and other calibration factors were calculated based on their relative peak area obtained from GC pictogram.

Initially, each gas reactant/product (CO_2, CH_4, H_2 and DME) was mixed with CO with different ratio and fed to GC as a binary mixture from the DME production system, analyzed online and calibration factor (β) of each of them was calculated.

Liquids at room temperature (methanol, formic acid, water and ethanol) were evaporated and also mixed with CO with different ratio and fed to GC online as a binary mixture in gas phase. In this procedure, each liquid was fed to the system from the reactor inlet bypass tee connection by a syringe pump followed by an evaporator while CO was flowing in the system. Therefore online analyses were carried out and β factor of each product was also calculated. Lines were heated to the temperature of 200°C to prevent condensation of liquids.

In the second method, a mixture was prepared in a gas sampling bottle (Figure 4.7) that contains 1% of all the species which were observed at the reactor outlet effluent stream with balanced argon gas. Initially gas sampling bulb was heated and kept at 200°C to prevent condensation. Then the sampling bulb was filled with argon gas and each gas species (CO, CO_2, H_2, CH_4 and DME) was manually injected using a gas tight syringe to the sampling bulb. Methanol, formic acid, water and ethanol were also manually injected to the sampling bulb using a liquid syringe. Finally, different amounts of this mixture (200-1000 μl) was manually injected to GC using a gas tight syringe and β factor of each component was calculated at the same time.

Additionally, a multi-component gas calibration standard that contains about 1% of each H_2, CO, CO_2, CH_4, C_2H_4, C_2H_6, C_3H_8 and 93 vol. % Ar was used to carry out calibration and compare the differences between calibration methods. β factors and retention times of C_2H_4, C_2H_6, C_3H_8 gases were also calculated in case of necessity.

Calibration factors of the species were tabulated in Table 4.6. Detailed calibration factor calculation is given in Appendix C.
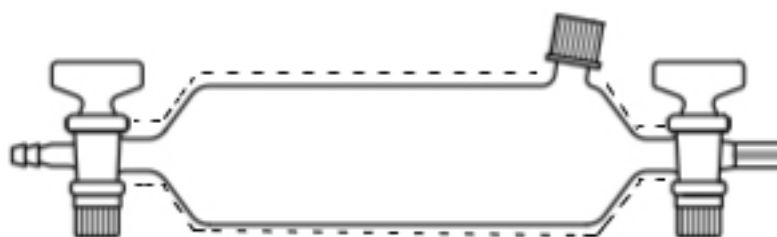
Figure 4.7. Gas sampling bottle (dashed lines indicates the heat zones)

Calibration factors for products and reactants which were observed at the reactor effluent stream are given in Table 4.6.

Table 4.6. *Calibration factors for products and reactants*

Component	Calibration Factor
CO	1.00
CH_4	0.31
CO_2	0.85
MeOH	1.70
DME	0.27
FA	0.46
EtOH	0.36
H_2	0.11

4.5. Experimental Procedure

Commercial methanol synthesis catalyst and commercial γ-alumina catalyst were crushed and then sieved in a 720 μm sieve. Synthesized catalysts were not subjected to sieving process, since they were in powder form. Before catalyst loading, methanol synthesis catalyst and methanol dehydration catalyst were physically mixed with a weight ratio of 1:1. However, bifunctional DME synthesis catalysts were directly placed. 0.3 g catalyst was loaded in the middle of the reactor and supported with ceramic wool from both ends. Then, the tubular reactor was placed into the tubular furnace. Reactor temperature was increased to 275°C with a heating rate of 10°C/min and a dwell time of 30 min under pure hydrogen volumetric flow rate of 12.5 ml/min at ambient pressure to perform the reduction of the catalyst. At the same time, all the lines were heated to a temperature of 200°C. After the reduction, hydrogen flow was turned off and the system was pressurized immediately using bypass lines with the

desired gas composition. When the reactor pressure reached 50 bar, valves on the bypass lines were closed. Pressurizing step should not exceed about 5 min to prevent the thermal damage, deactivation of the catalyst. Then the system pressure was monitored on the pressure gauge when the outlet lines of the system were closed for the leaking test for 5 min. Then gas flow rates were set using MFCs and outlet flow rate was measured using the soap bubble meter. Reactor effluent flow rate measurements using soap bubble and pressure changes in the system pressure gauge during the experiment help to reveal the leak in the system.

Pressurizing the reactor and the lines while they were at high temperature was preferred in order not to exceed minimum pressurization temperature (MPT). Thus, the risk of brittle fracture due to temperature embrittlement and H_2-assisted fracture was prevented (McLaughlin, 2006).

Each catalytic performance test run was 5 h. The effluent of the reactor stream was analyzed using GC with 50 minutes intervals during the performance test. Experimental parameters and catalysts are given in Table 4.7.

Table 4.7. *Experimental conditions for DME production*

Catalyst	CO₂/CO/H₂ ratio	Temperature (°C)	GHSV (ml/h.gcat)	Pressure (bar)
MSC	0/1/1	275	5000	50
CA+MSC*		275	5000	
CA+MSC		275	5000	
CA+MSC			3333	
CA+MSC**			5000	
CA+MSC**			5000	
CA+MSC		200	5000	
CA+MSC		250	5000	
CA+MSC		300	5000	
CA+MSC		350	5000	
EMA+MSC		275	5000	
EMA800+MSC		275	5000	
5TPA/EMA+MSC		275	5000	
10TPA/EMA+MSC		275	5000	
25TPA/EMA+MSC		275	5000	
5TPA@EMA+MSC		275	5000	
10TPA@EMA+MSC		275	5000	
25TPA@EMA+MSC		275	5000	
TPA@Cu-Zn@EMA		275	5000	
TPA@Cu-Zn@CMK-3		275	5000	
TPA@Cu-Zn@CMK-3	1/1/2	275	3333	
CA+MSC	1/4/5	275	5000	
CA+MSC	1/1/2	275	5000	
CA+MSC	4/1/5	275	5000	

(*: non-reduced test; **:repeatability tests)

CHAPTER 5

RESULTS AND DISCUSSION

Characterization and catalytic performance test results are presented and discussed in this chapter. All of the catalysts that have been used in this study, were characterized using different techniques to understand the effect of material properties on the catalytic activity.

5.1. Characterization Results

Several characterization methods were used to determine properties of materials. To make acidic dehydration catalyst, different amounts (5%, 10% and 25% by mass) of TPA were loaded to supports using different methods (impregnation and one-pot). Along with TPA, copper and zinc metals were also loaded to supports in the synthesis of bifunctional DME catalysts. Characterization of all materials were performed using XRD, nitrogen physisorption, SEM-EDX, TGA, TPD and TPR techniques. By this way, it is possible to get information about their crystal structure, acidity, surface area, pore size distribution, pore volume, reducibility, elemental composition and surface morphology. In this chapter, these characterization results are presented and discussed.

5.1.1. Characterization Results of Commercial Methanol Synthesis Catalyst

During single-step production of DME from syngas, a catalyst with a capability to produce methanol is primarily required. For this purpose, commercial methanol synthesis catalyst was also used as a catalyst. It was significant to characterize this catalyst to relate its catalytic activity to its properties. In order to identify the content

and crystal structure of the material, XRD was performed for the methanol synthesis catalyst.

In Figure 5.1, XRD pattern of commercial methanol synthesis catalyst is presented. MSC showed five peaks at 2θ values of 32.2°, 35.9°, 39.3°, 48° and 67°.

In XRD pattern of MSC, 2θ value of 31.8° was assigned to ZnO (1 0 0), whereas the broad peak between 35.5°-36.5° was assigned to CuO (- 1 1 1), CuO (0 0 2), ZnO (1 0 1) and Cu_2O (111) together. The peak at 2θ value of 39° was attributed to CuO (1 1 1), CuO (2 0 0) and γ-alumina together. The peak at 2θ value of 48° was assigned to ZnO (1 0 2) and CuO (-2 0 2) together. Broaden peaks with high intensities between 2θ value of 30-40° were observed due to overlapping of CuO, ZnO, Cu_2O and γ-alumina in the XRD pattern. According to the XRD analysis, nonreduced MSC does not contain metallic Cu, since the main peak of metallic Cu (1 1 1), which has a 2θ value of 43.3° was not observed in the XRD pattern of MSC.

Results revealed that metals were found to be in the oxidized form, therefore it was necessary to perform reduction before doing the activity tests. All XRD data for CuO, ZnO, Cu_2O, TPA and γ-alumina are given in Appendix D.
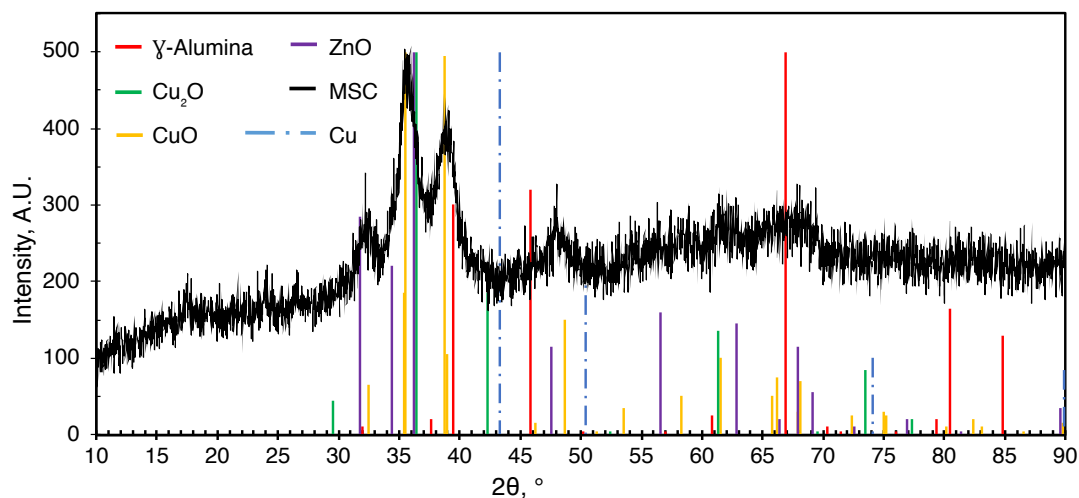
Figure 5.1. XRD pattern of commercial methanol synthesis catalyst (MSC) with XRD data of Cu$_2$O, CuO, ZnO and γ-alumina materials

Nitrogen physisorption isotherm of MSC is given in Figure 5.2. According to IUPAC classification, MSC exhibited a characteristic mesoporous Type IV isotherm with a hysteresis starting from about 0.65 P/P$_o$ value.
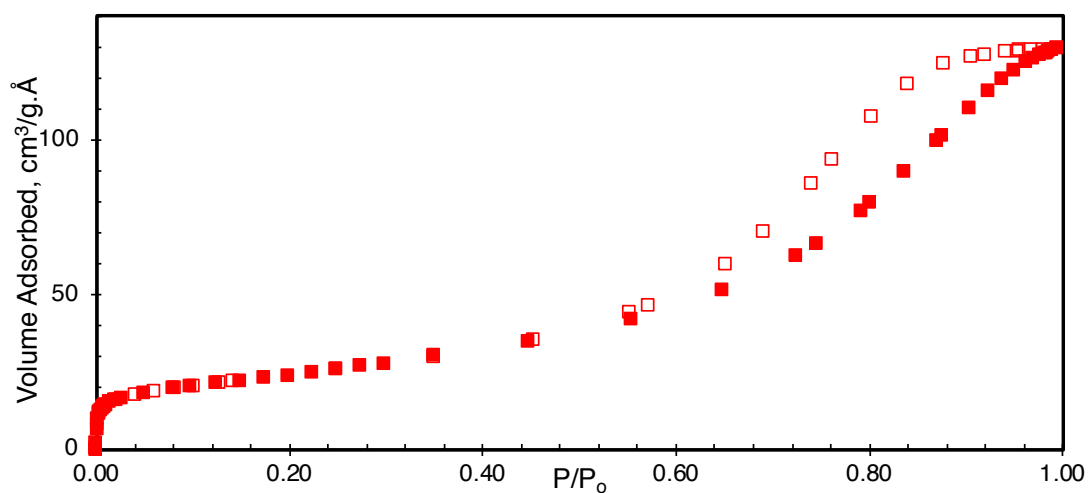
Figure 5.2. Nitrogen physisorption isotherm of MSC (filled symbols: adsorption and empty symbols: desorption branches)

Hysteresis is observed when capillary condensation occurs in mesopores and adsorption/desorption mechanisms deviate from one another. The isotherm of MSC exhibited any limiting adsorption at high P/P_o and could be classified as Type H2 loop, which indicates blocked or disordered pores. Relatively low surface area was expected due to the low N_2 adsorbed volume.

Figure 5.3 represents BJH desorption pore size distribution and Table 5.1 shows the physical properties of MSC. Average pore size and pore volume of MSC are 7 nm and 0.2 g/cm^3, respectively. Pore size distribution of MSC is in the range of mesoporous structure.
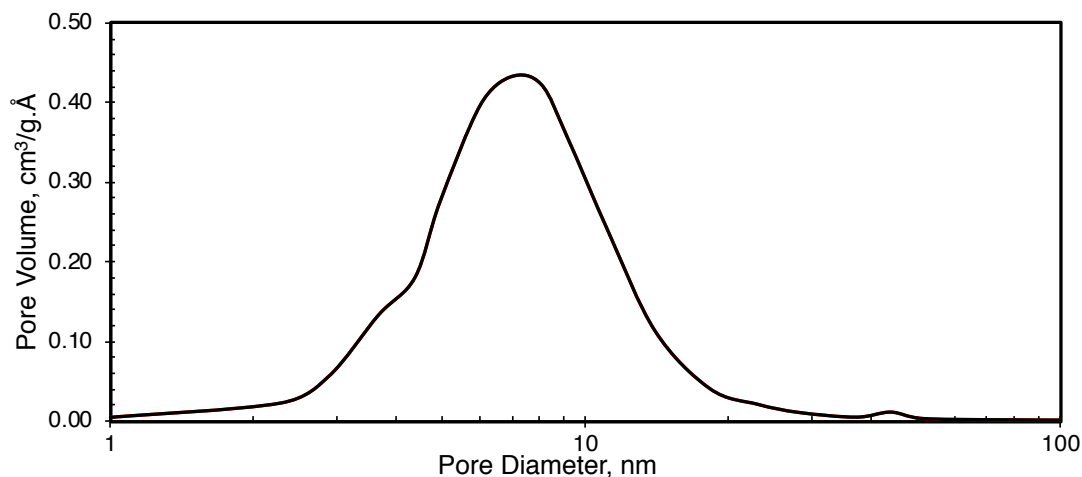
Figure 5.3. BJH desorption pore size distribution of MSC

Surface area of MSC is 87 m^2/g and this result is in accordance with low N_2 adsorbed volume in physisorption isotherm. N_2 adsorbed volume at 0.02 P/P_o was 16.34 cc/g whereas, N_2 adsorbed volume at 0.95 P/P_o was 122.74 cc/g. Microporosity of the sample was calculated as 13.3% using the ratio of N_2 adsorbed volume at 0.02 to N_2 adsorbed volume at 0.95 P/P_o.

Table 5.1. *Physical properties of commercial methanol synthesis catalyst*

Sample	Multipoint BET surface area, m^2/g	BJH Desorption pore volume, cm^3/g	BJH Desorption average pore diameter, nm	Micro-porosity, %
MSC	87	0.20	7.0	13.3

Hydrogen-TPR result of commercial methanol synthesis catalyst is given in Figure 5.4. TPR analysis of the sample was conducted up to 300°C with a heating rate of 5°C/min.
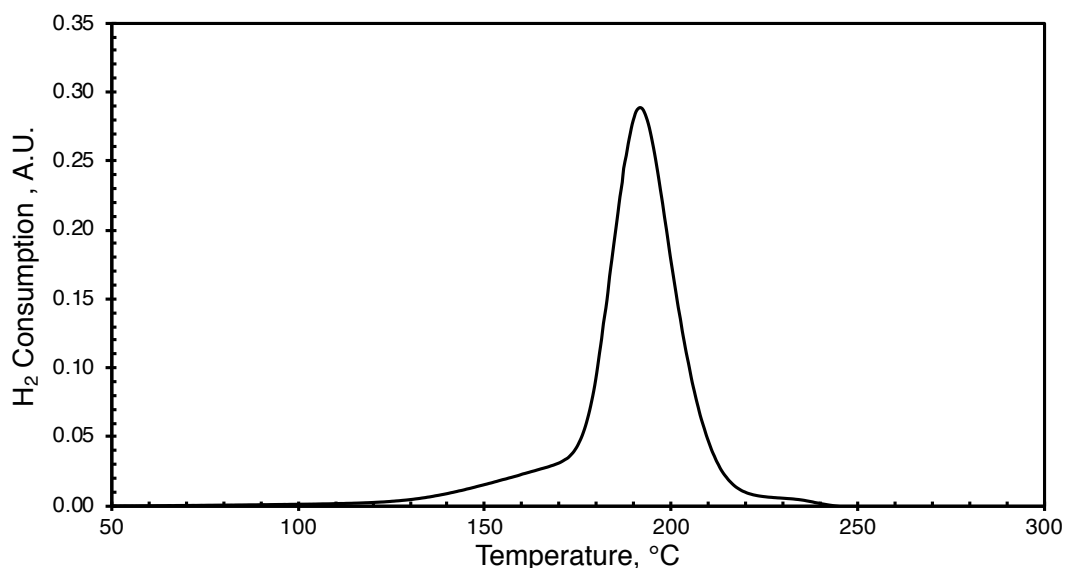
Figure 5.4. H_2-TPR analysis of commercial methanol synthesis catalyst

The shoulder of TPR curve showed that MSC has bimodal TPR profile. In contrast to TPD, reduction of metals is not a surface phenomenon but a bulk phenomenon (Fadoni & Lucarelli, 1999). Reactions taking place in the reactor are R7 and R8. R9 is the overall reaction, which is the result of two-step consecutive reactions (R7 and R8)

taking place in the reduction of MSC. Cu_2O is an intermediate product in the reduction of CuO to Cu. Therefore TPR curve of MSC was deconvoluted with Originlab Pro software using Gaussian method. It is reported that reduction of CuO to Cu_2O has a lower activation energy, resulting a reducibility at a lower temperature compared to the reduction of Cu_2O to Cu (Kim et al., 2014).

$$2CuO + H_2 \rightarrow Cu_2O + H_2O \qquad \Delta Hrxn = -100 \text{ kJ/mol} \qquad (R7)$$

$$Cu_2O + H_2 \rightarrow 2Cu + H_2O \qquad \Delta Hrxn = -71 \text{ kJ/mol} \qquad (R8)$$

$$CuO + H_2 \rightarrow Cu + H_2O \qquad \Delta Hrxn = -86 \text{ kJ/mol} \qquad (R9)$$

In the presence of hydrogen, CuO first starts to reduce, resulting in a buildup of Cu_2O and both increase in Cu_2O in the structure and the increase in temperature promotes the reduction reaction rate of Cu_2O, resulting in the TPR profile with a maximum. It was also reported that, a pseudo-direct reduction occurred instead of a sequential reduction under fast reduction conditions (Rodriguez et al., 2003). Hence, formation of Cu_2O is difficult to observe in the reduction of CuO at higher temperatures. These inferences are in good agreement with the deconvolution of the peak in TPR profile of MSC. Both XRD pattern of MSC (Figure 5.1) and deconvolution of the peak in TPR profile of MSC (Figure 5.5) proved the presence of Cu_2O in the structure. It was also seen that reduction of MSC was completed at 250°C. Deconvolution of TPR curve revealed that reduction temperature of CuO was 182°C, whereas reduction temperature of Cu_2O was 194°C.

Since deterioration of the structure and sintering of Cu clusters were reported in the literature under extreme reduction or calcination environment beyond 300°C temperatures, (Iranshahi et al, 2016), the reduction temperature was chosen as 275°C for MSC and bifunctional DME synthesis catalysts.
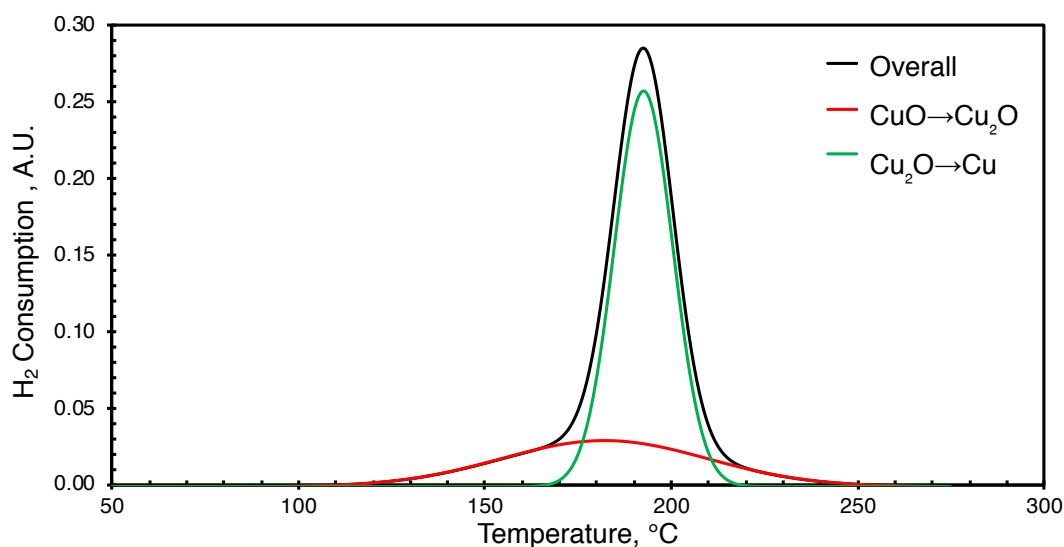
Figure 5.5. Peak deconvolution for TPR profile of MSC

5.1.2. Characterization Results of Mesoporous Alumina Supports

Three different alumina catalysts were used in this study, which were namely EMA, EMA800 and CA.

Synthesized alumina was calcined at two different temperatures to observe the effect of calcination temperature on the physical properties of alumina. Mesoporous alumina was calcined at 700°C and 800°C.

XRD patterns of three different alumina supports used in this study are given in Figure 5.6. Alumina (EMA) calcined at 700°C had no sharp peak, in fact the broad peak was observed at 2θ value range of 25°- 35°. The synthesized material was in amorphous structure. This result is in good agreement with the literature (Cava et al., 2007; Gonçalveset al., 2017). Commercial alumina (CA) showed peaks at 2θ values of 37°, 39.4°, 45.9°, 60°, and 67°. These peaks belong to γ-alumina (XRD cards in Appendix D), which indicates well crystalline γ-alumina structure. Two peaks at 2θ values of 45.9° and 67° were observed for alumina (EMA800) calcined at 800°C in the XRD pattern. These two peaks are the first two characteristic peaks of γ-alumina. Peak

61

intensities of commercial alumina were higher than that of synthesized alumina, which indicates higher crystallinity.

Crystal structure of mesoporous alumina depends on the calcination temperature. Calcination temperature higher than 700°C, γ-alumina crystalline phase forms due to the dehydration and desorption hydroxyl groups from the surface (Cava et al., 2007).
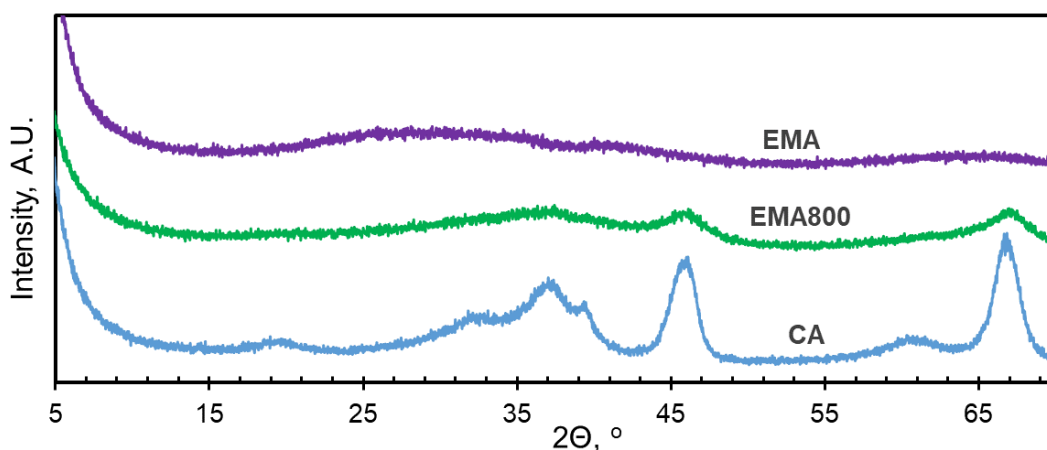
Figure 5.6. XRD patterns of alumina supports

Nitrogen physisorption isotherms for the three alumina materials are given in Figure 5.7. Based on IUPAC classification, all three materials had Type-IV isotherm and H1 hysteresis, which implies that the material had mesoporous structure. According to the nitrogen physisorption isotherm of EMA, hysteresis was observed at 0.71 P/P_o, whereas hysteresis was observed at 0.6 P/P_o in the nitrogen physisorption isotherm of EMA800 support. Since the starting point of hysteresis of EMA800 was slightly lower than EMA support, EMA had higher average pore size than EMA800. In addition to that, similar pore size distribution was expected for EMA and CA samples, due to having close hysteresis starting point. Since the adsorbed volume of CA was considerably lower than synthesized mesoporous alumina supports, it was implied that

CA had lower pore volume and surface area compared to synthesized mesoporous alumina supports.
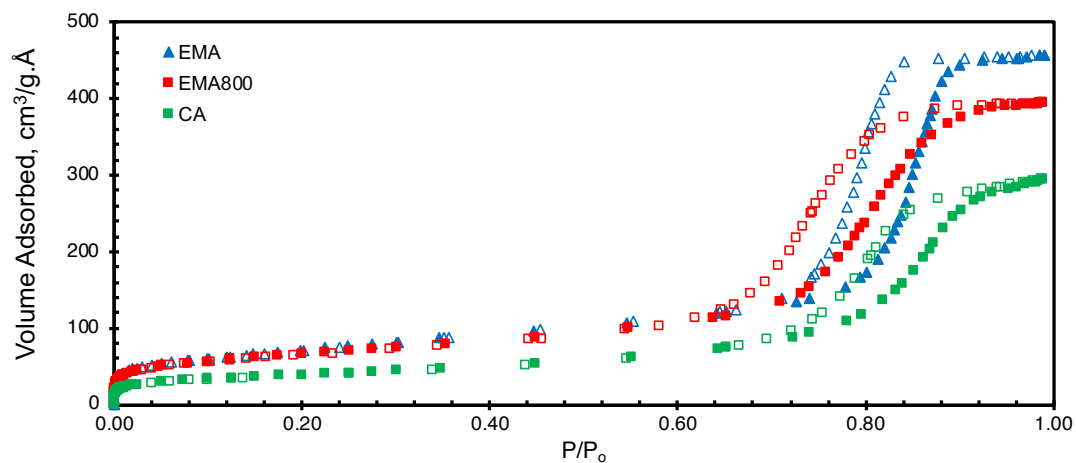
Figure 5.7. Nitrogen physisorption isotherms of alumina support (filled symbols: adsorption and empty symbols: desorption branches)

As it can be clearly seen in Figure 5.8, average pore size for EMA is very close to 10 nm. The CA material has slightly higher diameter than the EMA support. It can be seen that EMA800 has an average pore diameter of 7.8 nm. When the average pore sizes of materials calcined at different temperatures were compared, it can be said that an increase in calcination temperature reduces the pore size.
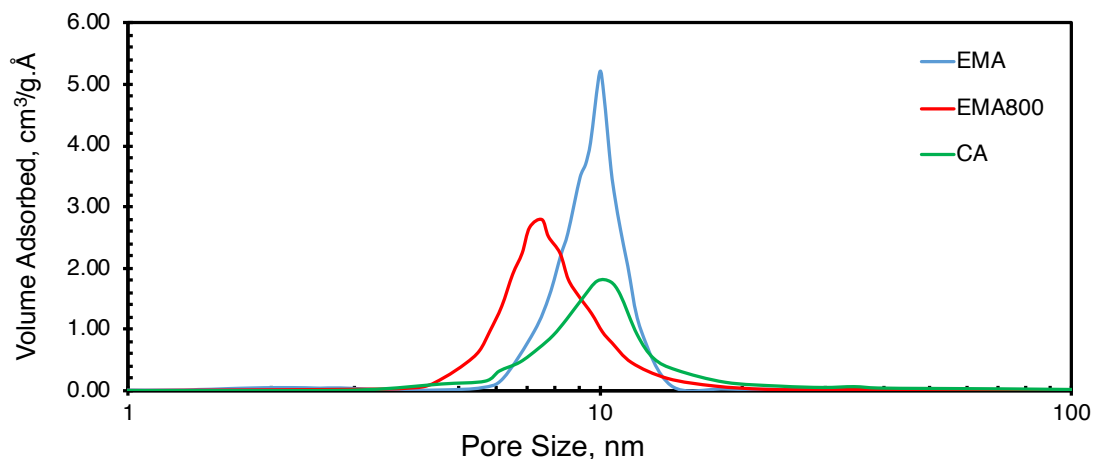
Figure 5.8. BJH desorption pore size distribution of mesoporous alumina materials

Table 5.2 shows the physical properties of mesoporous alumina materials. EMA had BET surface area of 256 m^2/g, whereas EMA800 had 231 m^2/g and CA had 137 m^2/g. EMA support calcined at 700°C had the highest pore volume and surface area among all three mesoporous alumina samples, as expected since it had the highest volume adsorption in the nitrogen isotherm.

Table 5.2. *Physical properties of mesoporous alumina samples*

Sample	Multipoint BET surface area, m^2/g	BJH Desorption pore volume, cm^3/g	BJH Desorption average pore diameter, nm	Micro-porosity, %
EMA	256	0.71	10.0	10.1
EMA800	231	0.61	7.8	11.0
CA	137	0.46	10.5	8.9

TGA was conducted for uncalcined EMA sample under air atmosphere to investigate the changes in the material during the calcination process. Figure 5.9 shows the TGA

curve of uncalcined mesoporous alumina. In TGA curve, the weight loss up to 125°C results from the physically adsorbed H_2O molecules on the material. The second peak around 190-200°C is attributed to conversion of isopropoxides to oxides. The third peak and forth peak, which can be seen between 200-250°C and 275-350°C, are related to decomposition of triblock copolymer P-123 and dihydroxylation of OH-groups, respectively (Gonçalves et al., 2017). There was not any weight change after the temperature of 500°C

During the synthesis of alumina support, about 80% weight loss was observed after the calcination process, i.e., 0.2 g sample was remained after the calcination of 1g sample and this result is in good agreement with TGA result.
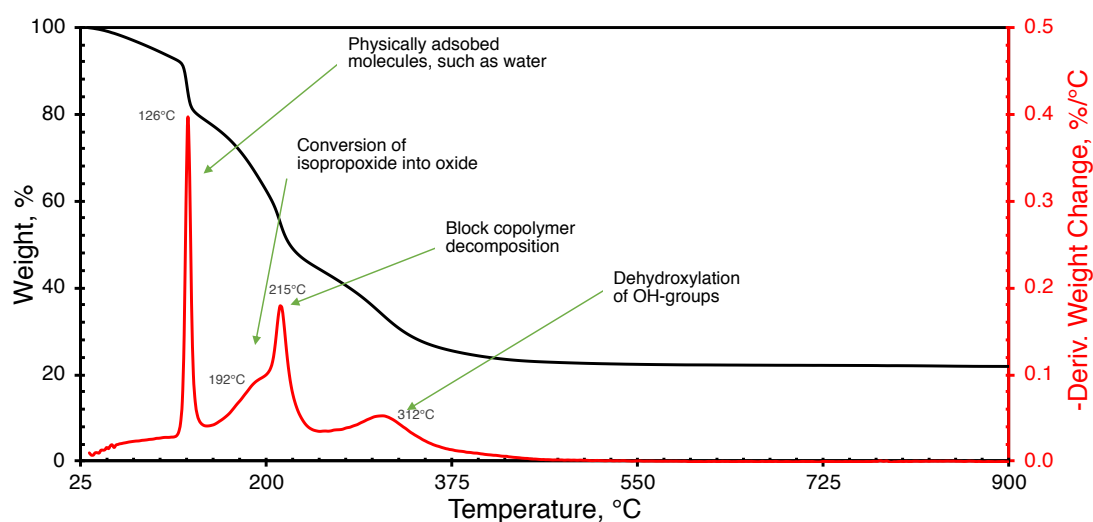
Figure 5.9. TGA curve of uncalcined mesoporous alumina

Determination of surface acidity and number of acid sites on the material helps to establish a relation between the material nature and catalytic activity. Figure 5.10 represents NH_3-TPD analysis result of commercial alumina (CA) and mesoporous

alumina (EMA) that was calcined at 700°C. Furthermore, total acid capacities of each support are presented in Table 5.3. When Figure 5.10 is examined, the first sharp peaks (40-100°C) shows the physical ammonia desorption, whereas the peaks at higher than 100°C represent the chemically adsorbed ammonia desorption. In the literature, it was stated that peaks at a temperature range of 200-400°C represent the moderate acidity, peaks higher than 400°C correspond to the strong acidity (Llanos et al., 2008; Srinivas et al., 2016). It was observed that, EMA support had three different acid sites in chemisorbed region with a main peak at 350°C. The CA sample also showed three different acid sites in chemisorbed region, however they formed as a broad peak in the TPD curve of CA sample.

Area under the desorption curves is proportional to the amount of ammonia released by the material. By looking at Figure 5.10, it is possible to say that EMA material has higher total acid capacity. Acid capacities of the samples were calculated using the TPD area values and the NH_3 calibration curve, which is given in Appendix B. This result is in good agreement with the total acidity results given in Table 5.3. Commercial alumina had a higher peak end compared to EMA sample, indicating stronger acidity.
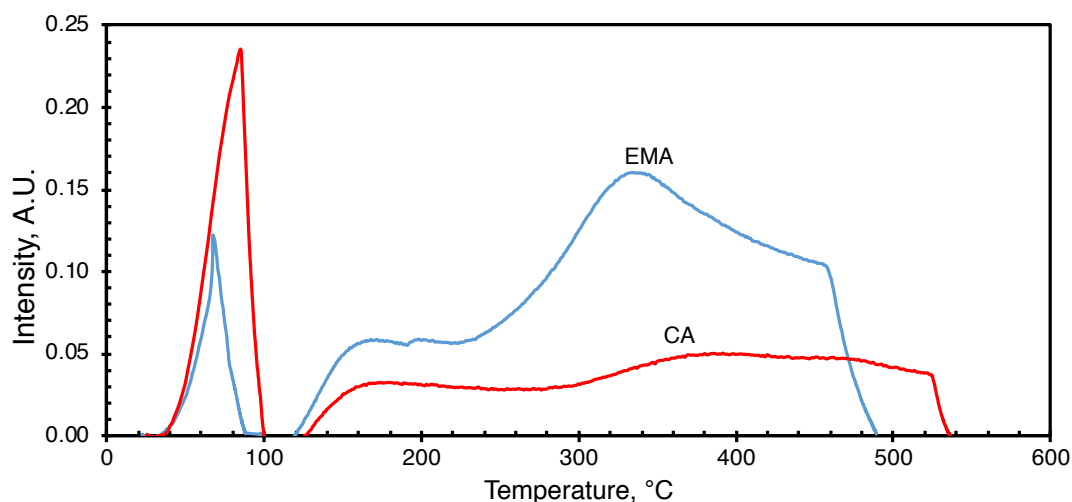
Figure 5.10. NH_3-TPD curves of mesoporous alumina supports

Table 5.3. *Total acid capacities of mesoporous alumina materials*

Sample	Total Acid Capacity, mmol/g
EMA	0.79
CA	0.46

SEM images of EMA supports with different magnifications are given in Figure 5.11. Figure 5.11 shows the agglomerated particles. Apart from the pores of the structure, gaps between these agglomerated alumina particles lead to different pore size distributions in the material.
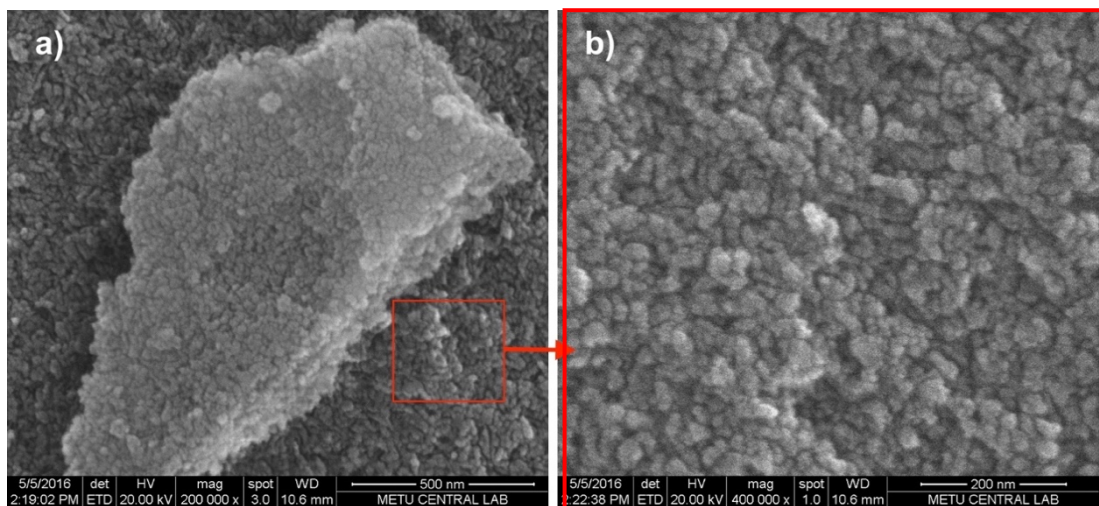
Figure 5.11. SEM images of EMA at different magnifications: (a) 200,000 and (b) 400,000

EDX result of EMA is given in Figure 5.12. Aluminum and oxygen elements are coming from mesoporous alumina. Al/O atomic ratio was found to be 2/3 from the EDX result. The Al/O atomic ratio was in good agreement with the atomic ratio of Al_2O_3, it can be said that mesoporous alumina synthesis was accomplished. Carbon element (C) is coming from the tape which was used to stick the sample to the holder for the analysis. Gold (Au) and palladium (Pd) elements were observed due to coating of sample.
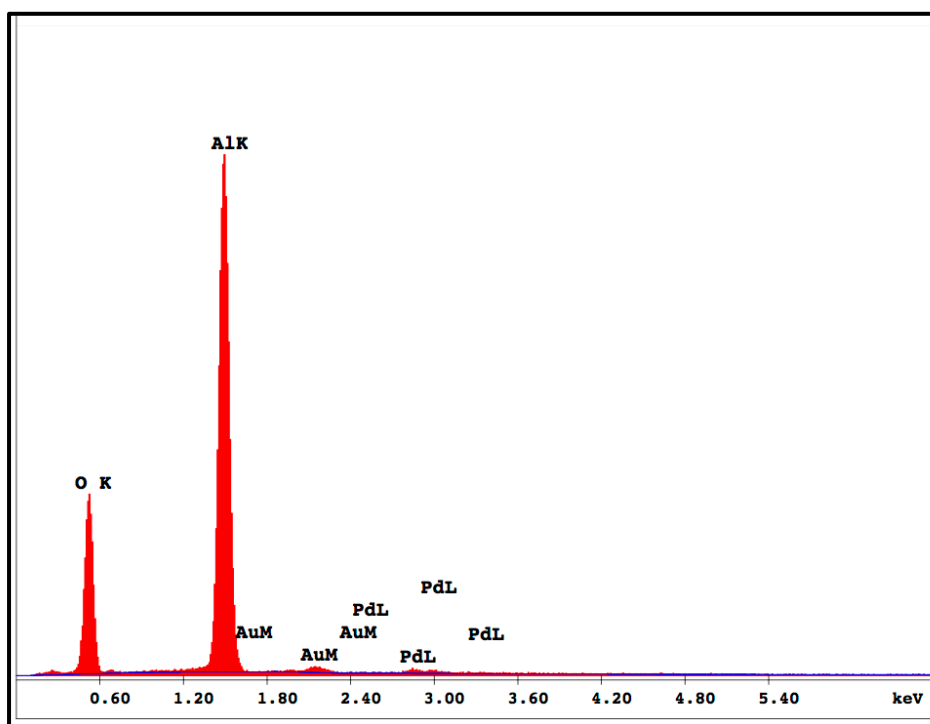
Figure 5.12. EDX spectrum of EMA support

SEM images from different parts of CA sample are given in Figure 5.13 whereas EDX spectrum of CA is given in Figure 5.14. It is seen that CA material had a uniform morphology. Morphology differences between CA and EMA materials can also be observed from SEM images. This result is in good agreement with XRD patterns of

mesoporous alumina materials (Figure 5.6), since EMA material was in amorphous form, whereas CA was in crystalline form.
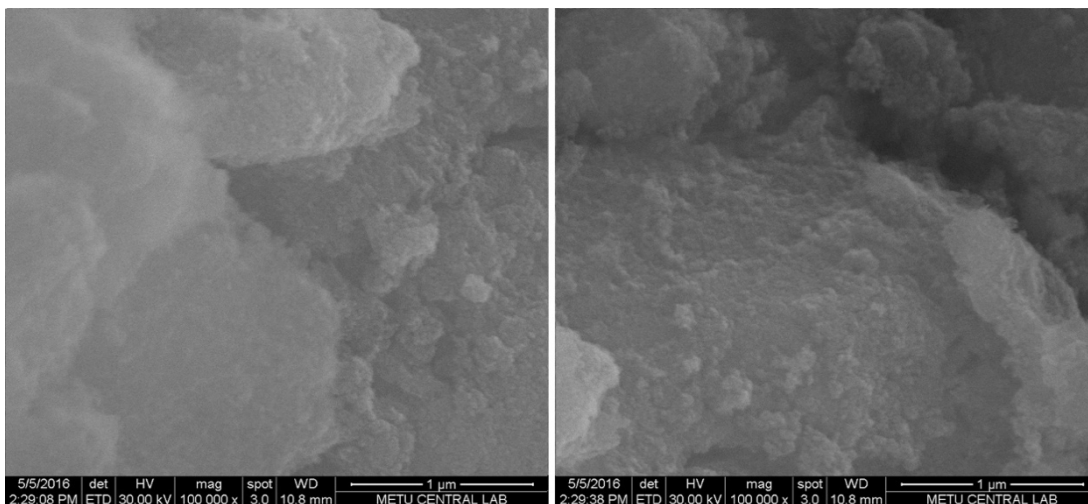
Figure 5.13. SEM images of CA samples from different parts

In the EDX spectrum of CA (Figure 5.14), only aluminum and oxygen elements were observed. Al/O atomic ratio of the material corresponds to 2/3, therefore this material can be classified as alumina and this result is in good agreement with XRD pattern of CA (Figure 5.6). Other than that, gold and palladium elements were observed due to coating of the material.
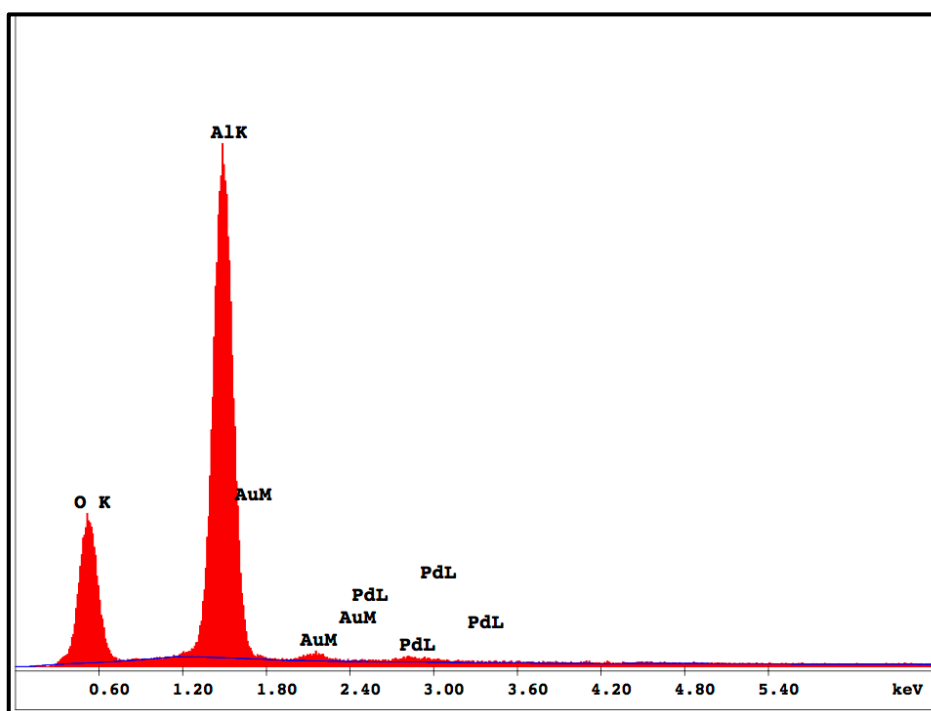
Figure 5.14. EDX spectrum of commercial alumina material

5.1.3. Characterization Results of TPA Loaded Mesoporous Alumina Catalysts

TPA was loaded into EMA support using two different methods, which were namely impregnation and one-pot. These TPA loaded EMA catalysts were characterized using different techniques. XRD analysis for pure TPA was carried out and presented in Figure 5.15. XRD data is given in Appendix D. The first three characteristic peaks of TPA were observed at 2θ values of 8.76°, 8° and 28.26°.
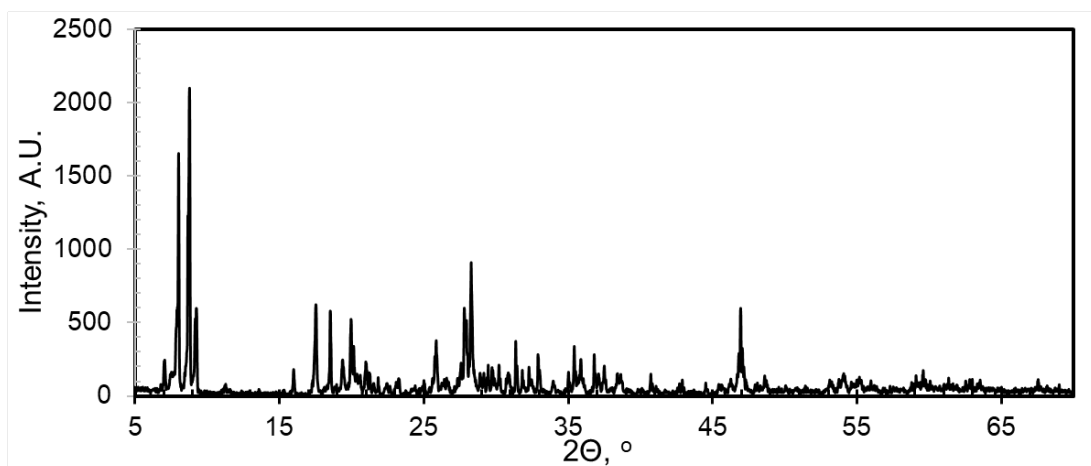
Figure 5.15. XRD pattern of pure TPA

In addition to XRD pattern of the mesoporous alumina support, XRD patterns of TPA impregnated alumina catalysts are given in Figure 5.16. 25TPA@EMA catalyst had an amorphous structure as confirmed by the broad peak between 2θ values of 25-35° as in EMA support. Since no peak of TPA was observed in XRD pattern of 25TPA@EMA sample, TPA was well dispersed in the structure. 5TPA@EMA and 10TPA@EMA samples showed peaks at 2θ values of 13°, 18°, 28°, 38°, 49° and 65°. Characteristic peaks of TPA at 2θ values of 18°, 28°, 38° and 49° were observed in the XRD pattern of 5TPA@EMA and 10TPA@EMA samples. This indicates that TPA was not dispersed well on these samples. Main peaks of TPA between 2θ values of 6-8° were not observed due to high intensity at high intensity background. Peak at 2θ value of 13° and 65° were unassigned peaks in the XRD patterns of TPA impregnated alumina catalysts.
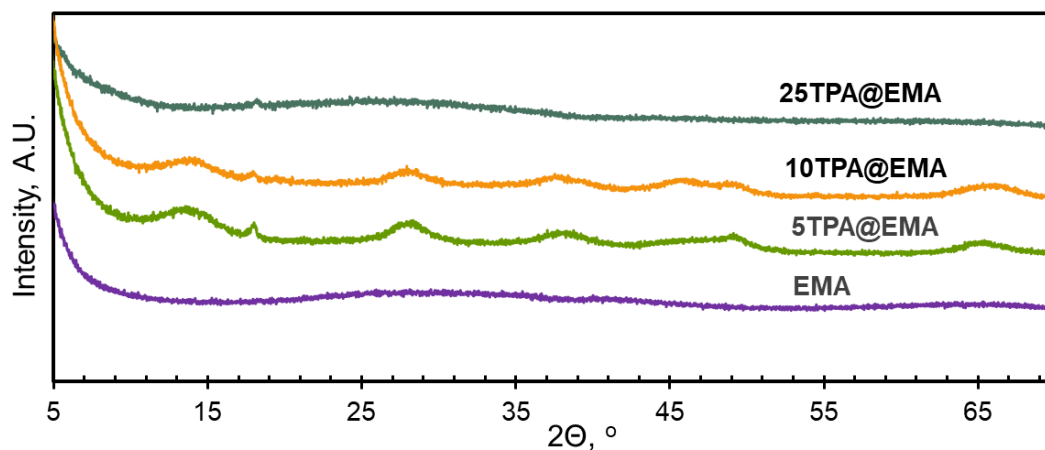
Figure 5.16. XRD patterns of TPA loaded alumina catalysts using the impregnation method

XRD patterns of TPA loaded alumina catalysts using one-pot method are given in Figure 5.17. All TPA loaded catalysts using one-pot method had amorphous structure as confirmed by the broad peak between 2θ values of $25\text{-}35°$. It can be said that TPA was well dispersed on alumina material, regardless of TPA amount. Moreover, one-pot method ensures that TPA disperse in the structure of the alumina.
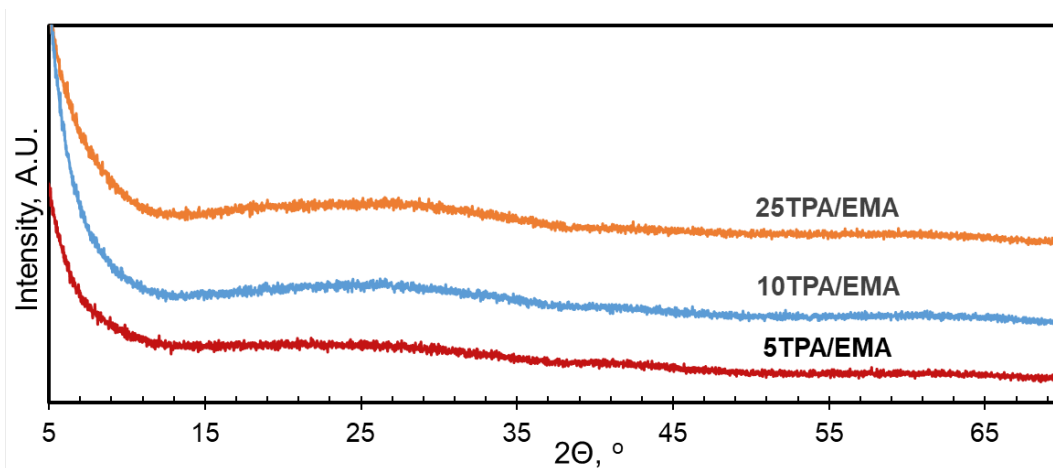
Figure 5.17. XRD patterns of TPA loaded alumina catalysts using the one-pot method

Nitrogen adsorption/desorption isotherms of EMA support and TPA impregnated alumina catalysts are given in Figure 5.18. All materials, showed Type-IV isotherm according to IUPAC classification, which indicates mesoporous material. Mesoporous alumina support and 25TPA@EMA showed H1 hysteresis, whereas 5% and 10% TPA impregnated ones showed H4 hysteresis. Hysteresis formation can originate from capillary condensation on mesopores. In H1 hysteresis, adsorption and desorption branches are parallel to each other and this hysteresis is the sign of ordered narrow pore size; on the other hand, H4 hysteresis can indicate the thin and narrow pores in the microporous region.

For the alumina support, formation of hysteresis was detected at P/P_o value of 0.65. However, with the impregnation of 5% and 10% TPA (by mass) into the alumina support, this value decreased to 0.40. This behavior might be the location of TPA in the structure of alumina support. This shifting to the left indicates a decrease in pore diameter of catalyst with an increase in TPA impregnation amount. TPA might be located in the mesopores, as a result, microporosity of the material was increased. Shifting of hysteresis was not observed with the impregnation of 25% TPA (by mass) into alumina support but the gap between isotherms become narrow.
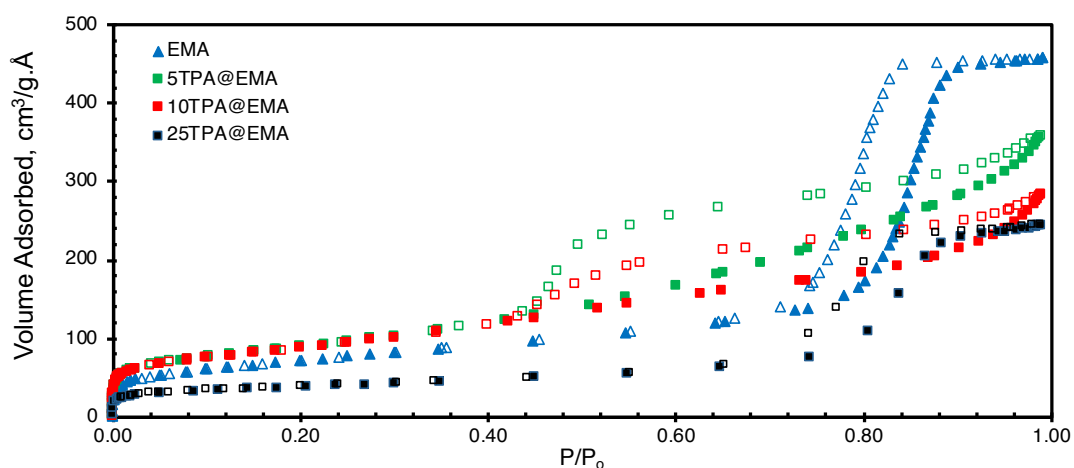
Figure 5.18. Nitrogen adsorption/desorption isotherms of EMA support and TPA impregnated EMA catalysts (filled symbols: adsorption and empty symbols: desorption branches).

Pore size distributions of the TPA impregnated EMA catalysts and EMA support are given in Figure 5.19. Results revealed that impregnation of 25% TPA only decreased the pore volume, not the average pore diameter, while 5% and 10% impregnation not only decreased the average pore diameter but also decreased pore volume. It was mentioned that the impregnation of 5 wt. % and 10 wt. % TPA to the pure alumina affected the pore size distributions by shifting them to the left side, which indicates the decrease in pore sizes. This shifting in pore size distribution can be explained by shifting in hysteresis formations of impregnated catalysis samples (Figure 5.18). Therefore, pore size distribution is in good agreement with the isotherm.
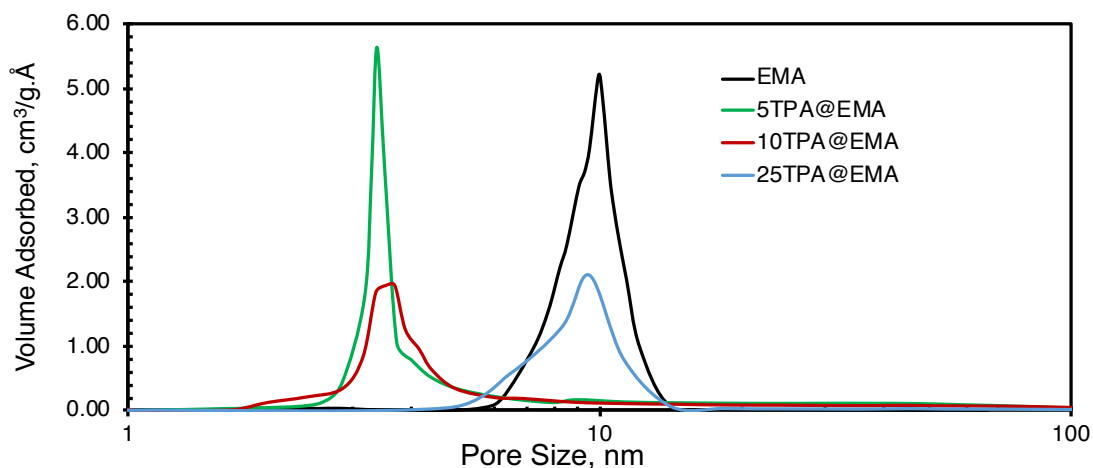
Figure 5.19. BJH desorption pore size distribution of EMA support and TPA loaded EMA catalysts

Physical properties of TPA impregnated EMA catalysts are given in Table 5.4. A decrease in pore volume with an increase in TPA loading amount due to blockage of mesopores was expected considering the isotherm and pore size distribution. Therefore, an increase in microporosity was also expected. For this reason, values in Table 5.4 matched with both isotherm and pore size distribution results. With an increase in TPA loading, surface area of all catalysts increased. However, only 25 wt. % TPA loaded sample had lower surface area than EMA support, despite having

74

higher TPA amount. Considering this result, it can be said that TPA might block the inside of the catalyst pores.

Table 5.4. *Physical properties of TPA impregnated EMA catalysts*

Sample	Multipoint BET surface area, m^2/g	BJH Desorption pore volume, cm^3/g	BJH Desorption average pore diameter, nm	Micro-porosity, %
EMA	256	0.71	10.0	10.1
5TPA@EMA	320	0.56	3.4	18.7
10TPA@EMA	314	0.45	3.7	23.9
25TPA@EMA	132	0.38	9.5	11.5

Nitrogen adsorption/desorption isotherms of one-pot TPA loaded catalysts are given in Figure 5.20. All materials showed Type-IV isotherm according to IUPAC classification, which indicates mesoporous structure. 10 wt. % and 25 wt. % TPA loaded catalysts using one-pot method show H1 hysteresis, whereas 5 wt. % TPA loaded one showed H4 hysteresis.

In one-pot method, all samples catalysts hysteresis starting at around P/P_o value of 0.45. In this case, it was expected that these TPA loaded alumina catalysts might have lower pore diameter compared to alumina support (EMA).
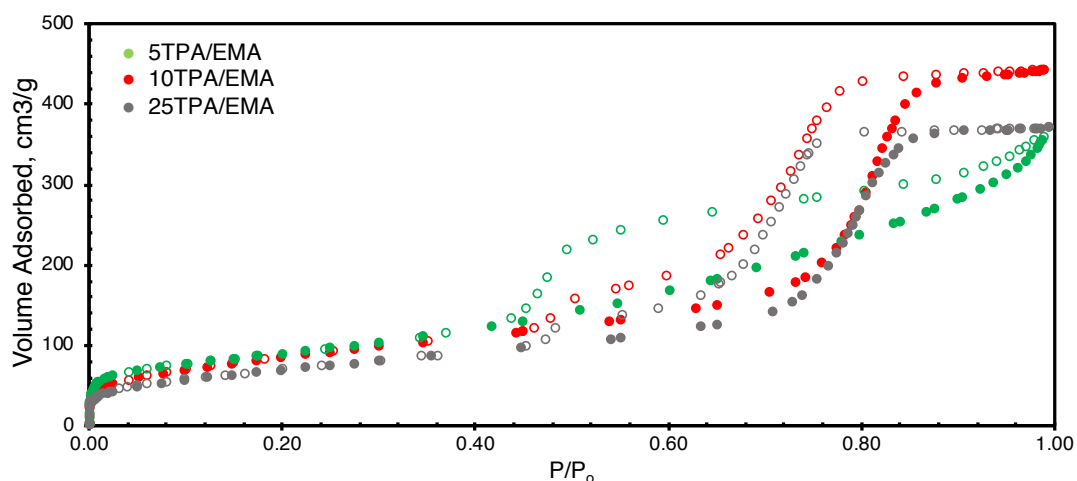
Figure 5.20. Nitrogen adsorption/desorption isotherms of TPA loaded EMA catalysts using one-pot method (filled symbols: adsorption and empty symbols: desorption branches).

Pore size distribution of TPA loaded catalysts using one-pot method are given in Figure 5.21. Physical properties of these samples are given in Table 5.5. Two types of average pore diameter were observed for 10 wt. % and 25 wt. % TPA loaded alumina samples in pore size distribution. These samples were bimodal, whereas 5 wt. % TPA loaded sample was mono type. Therefore, average pore diameter of 5TPA/EMA catalyst should be lower than the others. Pore diameter distribution of 10TPA/EMA and 25TPA/EMA catalysts were similar.
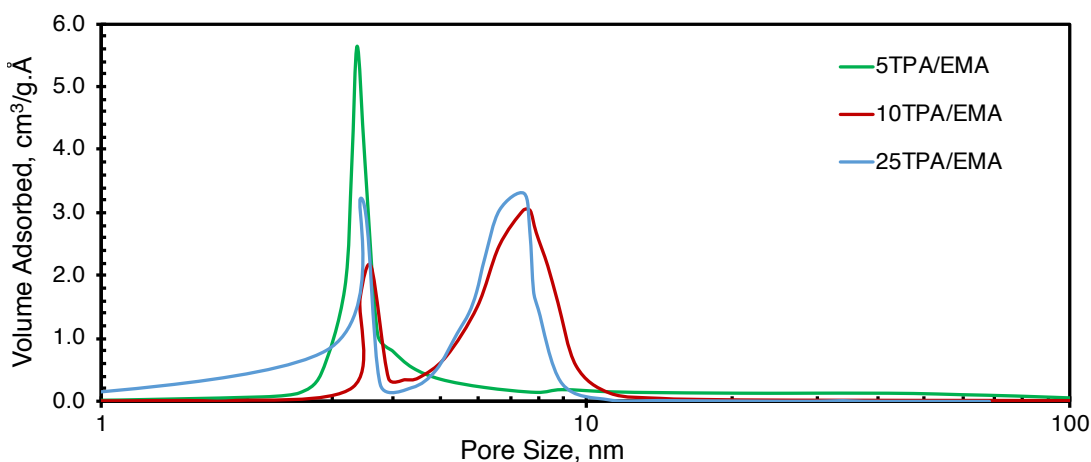
Figure 5.21. BJH desorption pore size distribution TPA loaded EMA catalysts using the one-pot method.

Although surface areas of 5 wt. % and 10 wt. % TPA loaded catalysts were close to each other, pore diameter and microporosity values were much similar between 10% and 25 wt. % TPA loaded samples.

5 wt. % TPA loaded sample has the highest microporosity in all one-pot synthesized catalysts due to the presence of H4 hysteresis compared to other catalysts. H4 hysteresis may indicate narrow slit pore size and microporous structure. This also coincides with the results of microporosities.

It was seen that both 5% and 10% TPA loaded catalysts either using one-pot or impregnation had the similar surface area values. However, taking into account the pore volume, pore size and surface area of the catalysts, TPA loaded catalysts using one-pot method had superior properties than TPA impregnated catalysts.

Table 5.5. *Physical properties of TPA loaded mesoporous alumina catalysts using one-pot method*

Sample	Multipoint BET surface area, m^2/g	BJH Desorption pore volume, cm^3/g	BJH Desorption average pore diameter, nm	Micro-porosity, %
5TPA/EMA	309	0.52	3.3	16.8
10TPA/EMA	310	0.69	3.6 & 7.4	11.2
25TPA/EMA	255	0.57	3.4 & 7.5	11.0

NH_3-TPD curves of EMA support and TPA impregnated EMA catalysts are given in Figure 5.22. Major peak of all samples were at around 320-360°C, which were attributed to moderate acidity. The 25TPA@EMA catalyst showed similar ammonia desorption behavior, except the end of the peak was shifted to the right, indicating a stronger acidity. It can be said that 25% TPA impregnation did not cause a significant change on the acidity of EMA support. 10% TPA impregnation into EMA support not only increased the total area under the NH_3 desorption curve, which corresponds to total acidity, but also shifted the NH_3 desorption curve to a higher temperature.

By looking at the area under curves, the 10TPA@EMA catalyst had the highest both weak and strong acidity peaks among the samples. This result is in good agreement with the total acidities given in Table 5.6. In Table 5.4, surface area of the 10TPA@EMA catalyst was much higher than the 25TPA@EMA catalyst, indicating much more active site per unit mass of sample. This result was found to be matching with total acidity result.
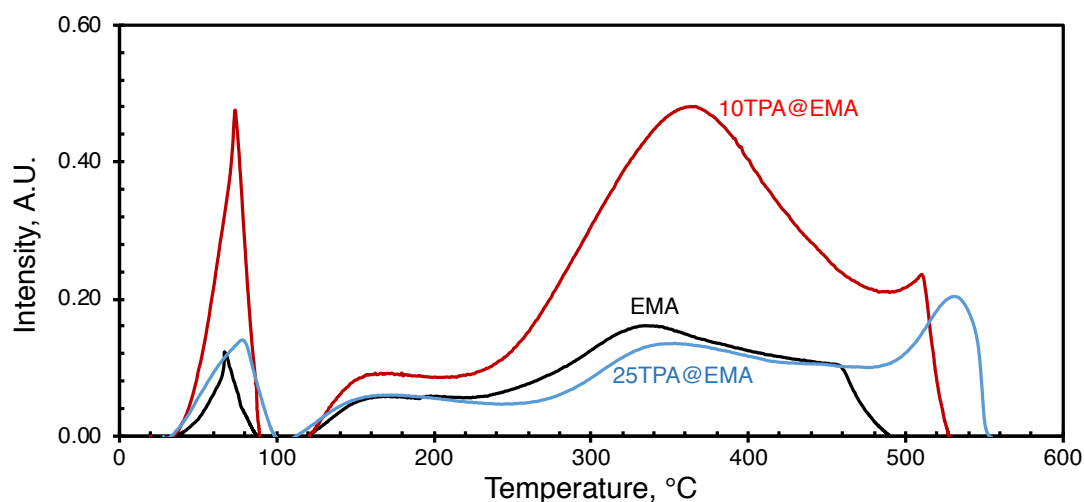
Figure 5.22. NH₃-TPD curves of EMA support and TPA impregnated EMA catalysts

Table 5.6. *Acid capacities of EMA support and TPA impregnated EMA catalysts*

Sample	Total Acid Capacity, mmol/g
EMA	0.79
10TPA@EMA	2.00
25TPA@EMA	0.87

Peaks in TPD profiles of the EMA support and 10TPA@EMA catalyst were deconvoluted using Gaussian method in Originlab Pro software (Figure 5.23).

EMA support had four peaks at 72°C, 180°C, 360°C and 450°C, whereas 10TPA@EMA catalyst had four peaks at 73°C, 181°C, 375°C and 510°C in deconvoluted TPD profiles. No additional peak was observed in deconvoluted TPD profile of 10TPA@EMA catalyst compared to EMA support. All peak intensities increased with the TPA loading in 10TPA@EMA catalyst. The first peaks in both TPD profile correspond to physical desorption. TPA loading did not shift the first and

the second peaks and they remained almost constant. However, about 15°C and 60°C shift to higher temperature was seen in the desorption of third and fourth peaks.
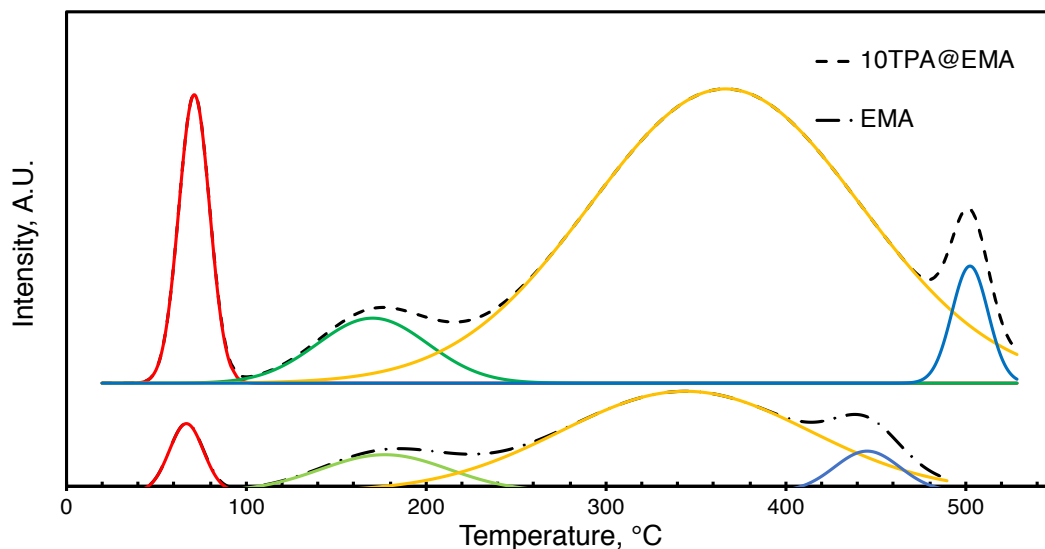
Figure 5.23. Deconvoluted TPD profiles of EMA support and 10TPA@EMA catalyst (dashed lines: original TPD curves, solid lines: deconvoluted peaks)

Considering nitrogen physisorption analysis and TPD analysis, 10TPA@EMA sample is considered the most promising catalyst compared to other impregnated catalysts due to having higher acidity and better physical properties.

NH_3-TPD analysis curves of EMA support and one-pot TPA loaded EMA samples are given in Figure 5.24. 25 wt. % TPA loaded sample showed the highest physical ammonia desorption peak, whereas 10 wt. % and 25 wt. % TPA loaded catalysts showed similar chemical ammonia desorption behavior. 10TPA/EMA sample had four peaks at 73°C, 154°C, 394°C and 470°C, whereas there were four peaks of 25TPA/EMA at 66°C, 170°C, 416°C and 481°C.

A successful peak deconvolution was not achieved in the case of one-pot synthesized catalysts. However, it can be seen that maximum point of third and fourth peaks of

EMA structure have been shifted to higher temperatures, whereas significant shift in the peak ends was not observed for any sample.

All physical desorption peaks of TPA loaded catalysts using one-pot method (Figure 5.24) had different maximum temperature values, compared to impregnated catalysts (Figure 5.22). Additionally, fast heating rate for physical desorption may lead shifting in the physical desorption peaks. However, lower heating rates were applied to prevent shifting in chemical desorption region.

Results revealed that 10 wt. % TPA loading using one-pot method significantly increased the total acidity of EMA support compared to 25 wt. % TPA loaded EMA catalyst using one-pot method. These results are in good agreement with total acidity values given in Table 5.7.
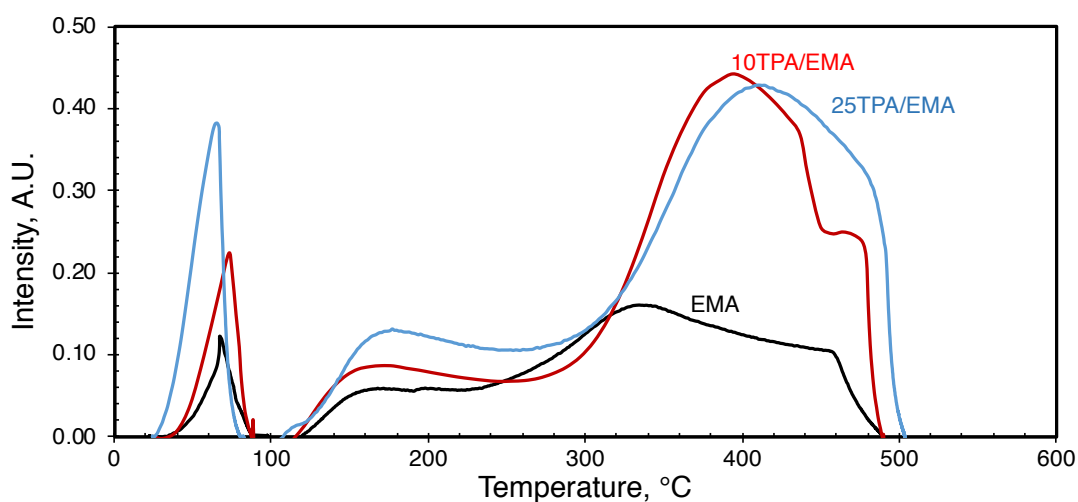
Figure 5.24. NH3-TPD curves of EMA support and TPA loaded EMA catalysts using one-pot method

Table 5.7. *Acid capacities of one-pot TPA loaded EMA samples*

Catalyst	Total Acid Capacity, mmol/g
EMA	0.79
10TPA/EMA	1.78
25TPA/EMA	1.96

Figure 5.25 shows the SEM images of 5 wt. % TPA impregnated sample at different magnifications. Differences in the morphology between EMA support and the 5TPA@EMA catalyst can be clearly seen in the SEM images.
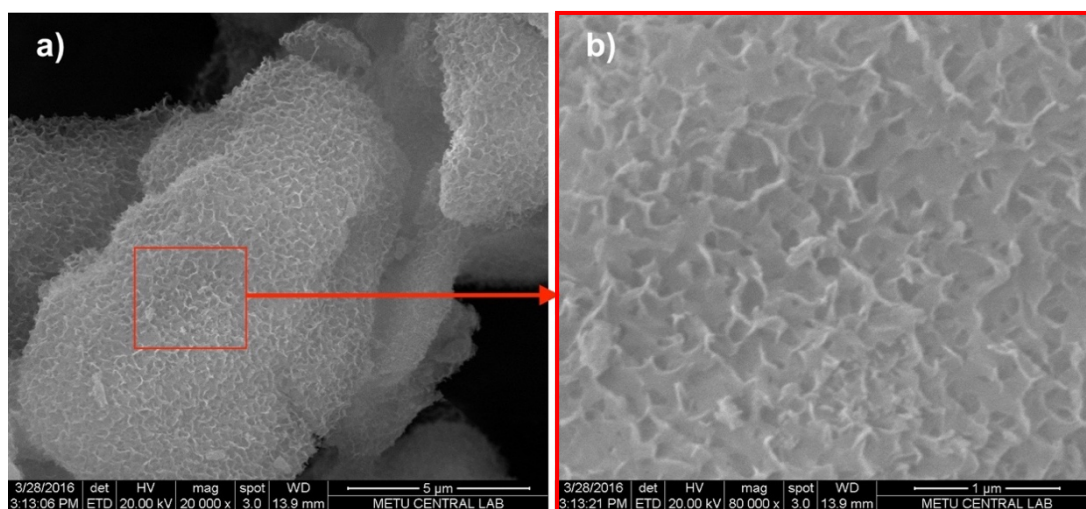
Figure 5.25. SEM images of 5TPA@EMA at different magnifications: (a) 20,000 and (b) 80,000

Addition to aluminum and oxygen, tungsten peak was also seen in EDX spectrum of 5 wt. % TPA impregnated sample, which is given in Figure 5.26. Tungsten peak was coming from TPA. Since tungsten has Mα energy of 1.775 keV and aluminum has Kα energy of 1.485 keV, two peaks are very close to each other. Considering the

loading amount, the relative amount of phosphorus in TPA, it is out of the range of detection limit of EDX analysis and therefore phosphorus was not observed in the spectrum. One should also notice that, oxygen peak intensity is higher than that was observed in EMA (Figure 5.12) since some oxygen content is also coming from TPA structure. EDX results showed that about 5 % TPA was successfully loaded into EMA support.
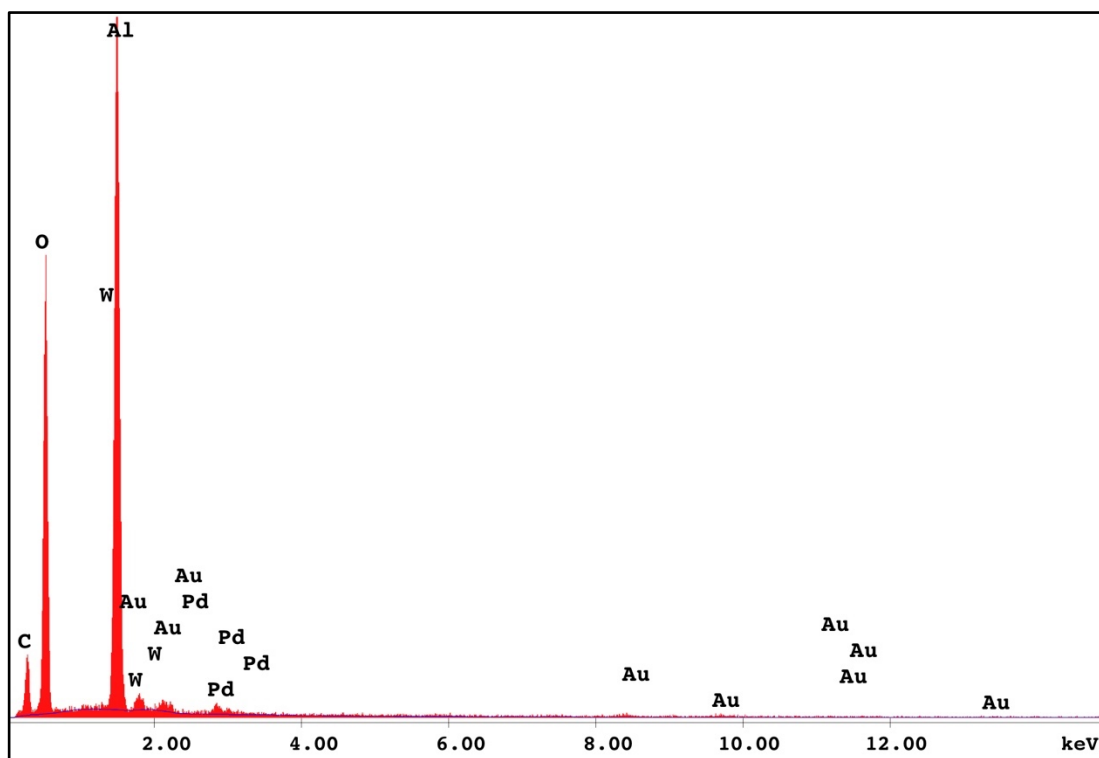
Figure 5.26. EDX spectrum of 5TPA@EMA

SEM image of 10TPA@EMA at 200,000 magnification is given in Figure 5.27a and backscattered electron image is given in Figure 5.27b.
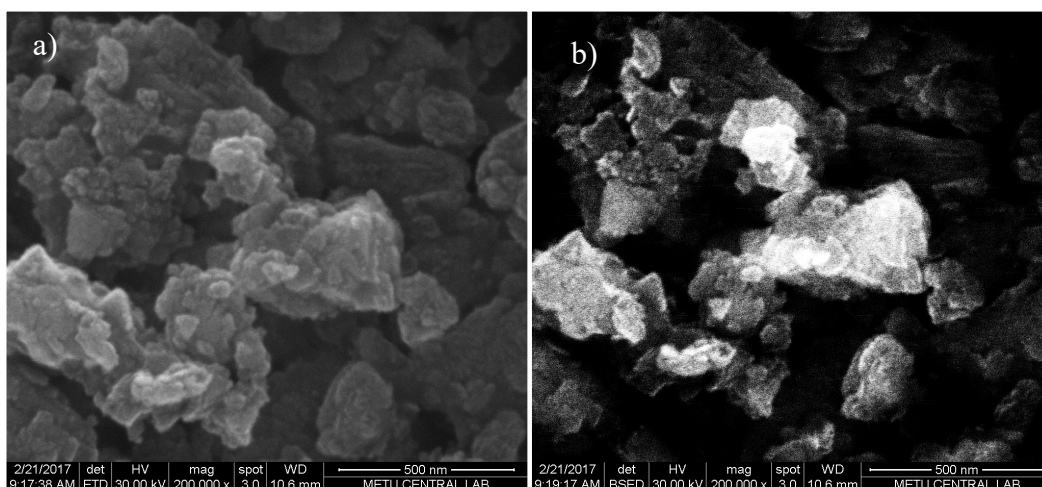
Figure 5.27. SEM (a) and backscattered electron (b) images of the 10TPA@EMA catalyst at 200,000 magnification

SEM image of 10TPA/EMA at 400 magnification is given in Figure 5.28a and backscattered electron image is given in Figure 5.28b. Differences in the morphology between the 10TPA/EMA catalyst and the 10TPA@EMA catalyst is clear in these images. TPA is well dispersed on the 10TPA/EMA catalyst.
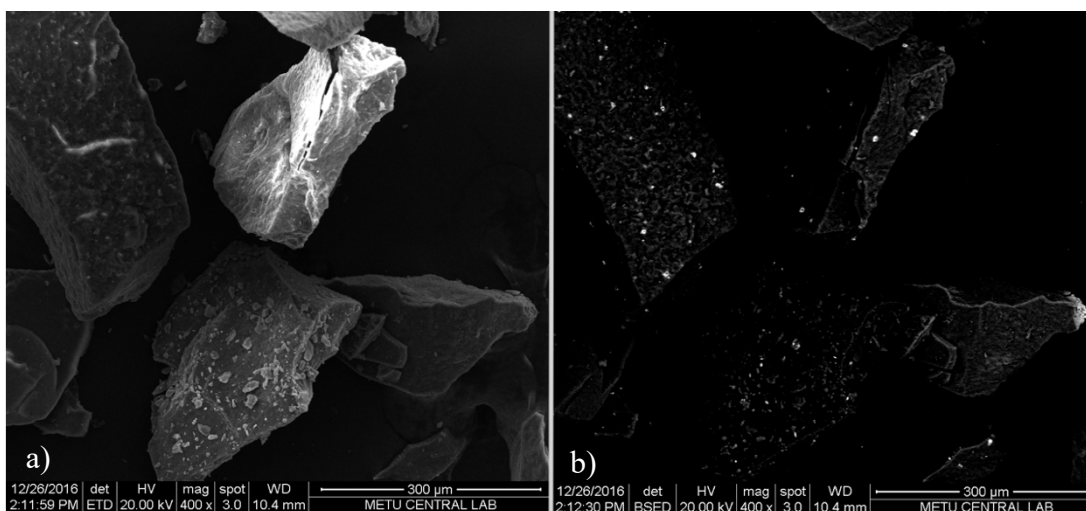
Figure 5.28. SEM (a) and backscattered electron (b) images of the 10TPA/EMA catalyst at 400 magnification

SEM image of 25TPA/EMA at 400 magnification is given in Figure 5.29a and backscattered electron image is given in Figure 5.29b. It was seen that TPA dispersion per unit area was increased with the increase in TPA loading amount. TPA was better dispersed on the 25TPA/EMA compared to the 10TPA/EMA catalyst. However, morphology of the both catalysts were similar.
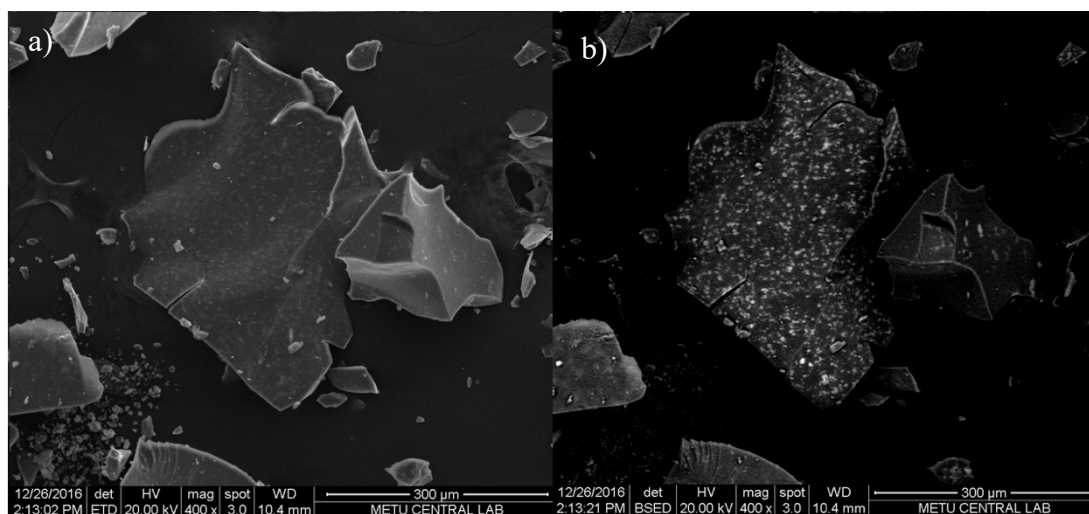
Figure 5.29. SEM (a) and backscattered electron (b) images of the 25TPA/EMA catalyst at 400 magnification

Based on XRD and SEM-EDX analysis, TPA was well dispersed on the catalysts synthesized using one-pot method compared to TPA impregnated catalysts.

Elemental composition of the catalysts are given in Table 5.8. Values were normalized and only aluminum and oxygen elements were considered for the alumina supports, whereas aluminum, oxygen and tungsten elements were considered for the TPA loaded catalysts. TPA were successfully loaded to EMA support material using both methods. However, less tungsten amount was observed for 10% TPA loaded samples compared to 25% TPA loaded sample.

Table 5.8. *Elemental compositions of the synthesized catalysts*

Catalyst	Element (wt. %)		
	Al	O	W
EMA	54.8	45.2	-
CA	49.6	50.4	-
5TPA@EMA	37.3	58.7	4.0
10TPA@EMA	38.9	54.4	6.7
10TPA/EMA	33.4	61.1	5.6
25TPA/EMA	39.2	36.2	24.6

5.1.4. Characterization Results of Synthesized CMK-3 Catalysts

CMK-3 was synthesized using the SBA-15 material as the template. The XRD pattern of CMK-3 sample is given in Figure 5.30. Amorphous structure of CMK-3 was confirmed by the broad peak between 2θ values of 20-30°.
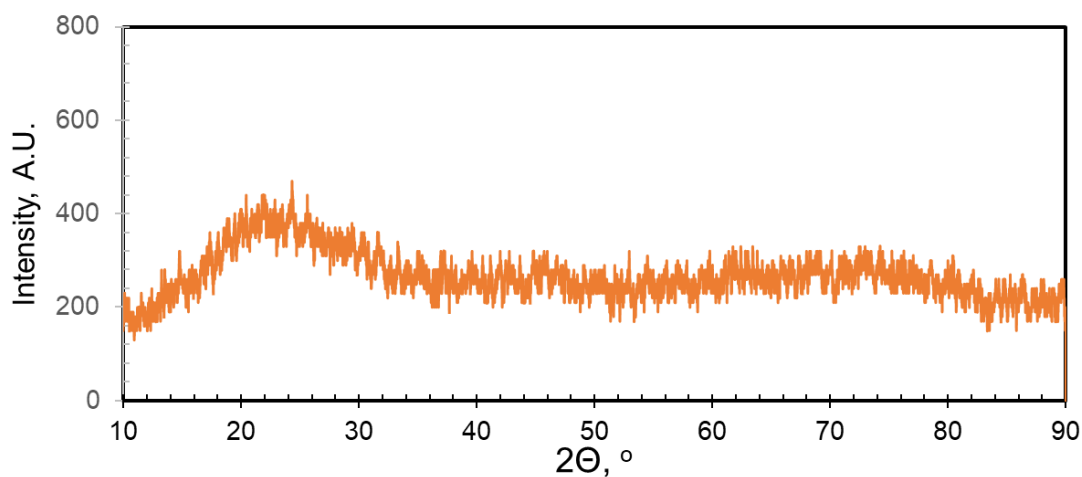
Figure 5.30. XRD pattern of CMK-3 support.

Nitrogen physisorption isotherm CMK-3 is given in Figure 5.31. CMK-3 support exhibited Type IV isotherm, indicating mesoporous structure. Formation of hysteresis was detected at P/P_o value of 0.44. Type H2 hysteresis was observed for CMK-3 support. A microporous structure was expected due to high adsorption at very low pressures ($P/P_o < 0.05$) indicating the micropore filling. Microporosity of CMK-3 was 36.4%.
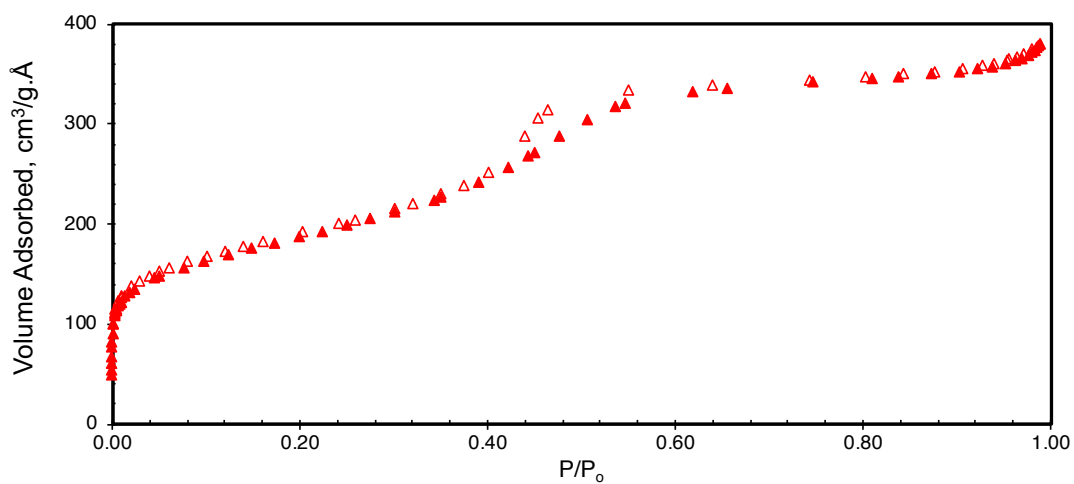
Figure 5.31. Nitrogen physisorption isotherm of CMK-3 support (filled symbols: adsorption and empty symbols: desorption branches).

Pore size distribution of CMK-3 support is given in Figure 5.32. Average pore diameter of CMK-3 was 3.5 nm.
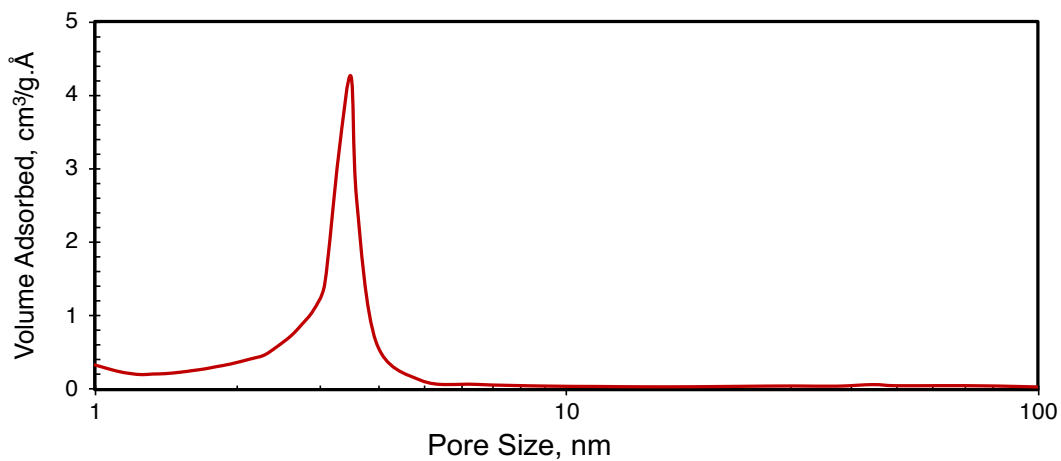
Figure 5.32. BJH desorption pore size distribution of CMK-3 support

89

CMK-3 had multipoint BET surface area of 652 m^2/g, BJH desorption pore volume of 0.62 cm^3/g.

SEM images of CMK-3 support at different magnifications are given in Figure 5.33.

SEM images of CMK-3 showed the rod-like morphology. Images revealed that the rod-like CMK-3 was 600-900 nm in length and 250-350 nm in diameter. These results were in good agreement with the literature (Barrera et al., 2013; He et al., 2009).

EDX analysis of CMK-3 (Figure 5.34) showed that CMK-3 contained 95 wt. % C and balanced Si, Na and O elements, confirming the success of the synthesis of the sample. The trace amount of Si was the indication of SBA-15 remained in the structure and the trace amount of Na was the indication of adsorption of NaOH during the sample preparation. Oxygen element was coming from both SBA-15 and NaOH.
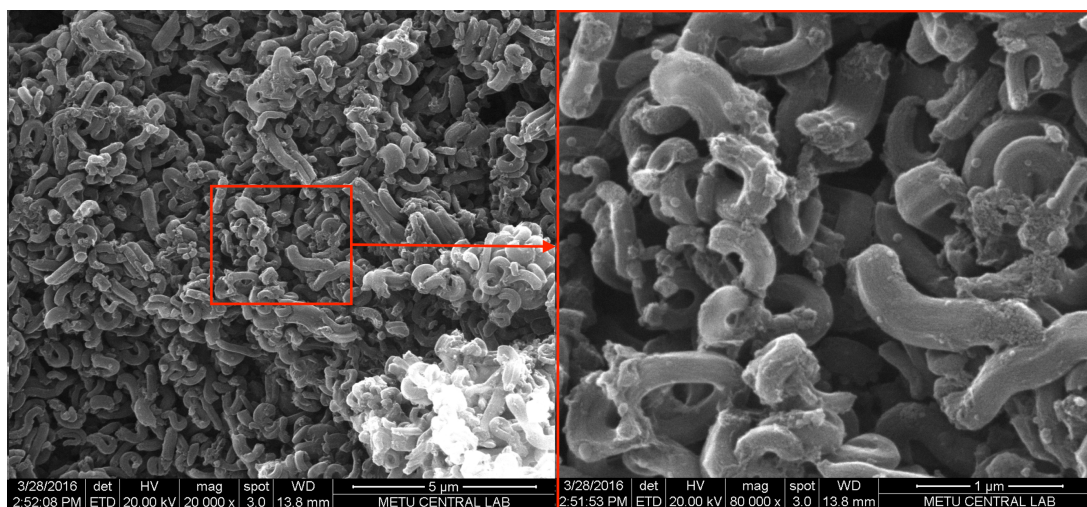
Figure 5.33. SEM images of CMK-3 catalyst at different magnifications: (a) 20,000 and (b) 80,000
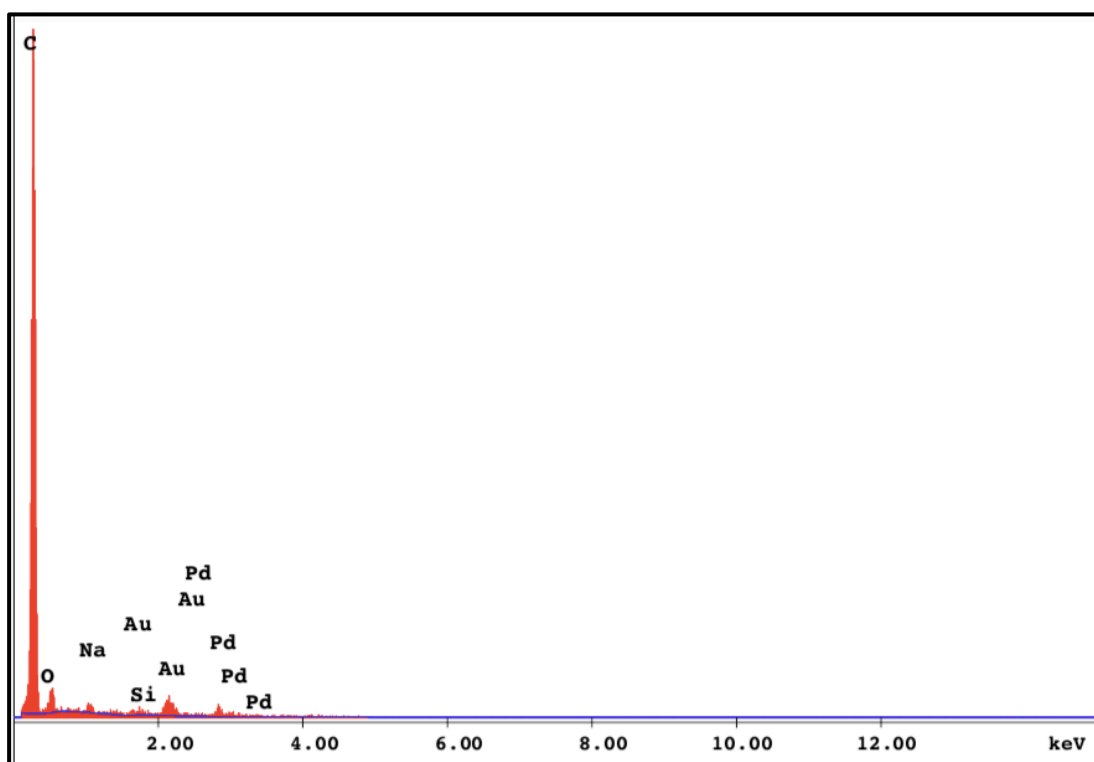
Figure 5.34. EDX spectrum of CMK-3 support

5.1.5. Characterization Results of Bifunctional DME Synthesis Catalysts

Bifunctional DME catalysts were synthesized using two different supports, which were namely EMA and CMK-3. Cu-Zn metals were loaded to supports for the methanol synthesis and TPA was also loaded to supports in order to increase acidity of the catalysts. Nitrogen physisorption isotherms of the TPA@Cu-Zn@EMA and TPA@Cu-Zn@CMK-3 catalysts are given in Figure 5.35-Figure 5.36. Both isotherms exhibited Type IV isotherm. Adsorption isotherm of TPA@Cu-Zn@EMA exhibited monolayer and multilayer adsorption and capillary condensation. Additionally, both adsorption and desorption isotherms were parallel to each other. Adsorption and desorption loop of TPA@Cu-Zn@CMK-3 catalyst did not exhibit any limiting adsorption at high P/P_o value. H1 and H3 hystereses were observed for the TPA@Cu-Zn@EMA and TPA@Cu-Zn@CMK-3 catalysts, respectively. Starting P/P_o value of

91

hysteresis of TPA@Cu-Zn@EMA catalyst (0.65) was lower than that of TPA@Cu-Zn@CMK-3 catalyst (0.90). Therefore the TPA@Cu-Zn@EMA catalyst had a lower pore size than that of TPA@Cu-Zn@CMK-3 catalyst. N_2 adsorption volumes of both catalysts were significantly lower than the support materials, indicating a decrease in surface area values with the addition of TPA and Cu-Zn metals.
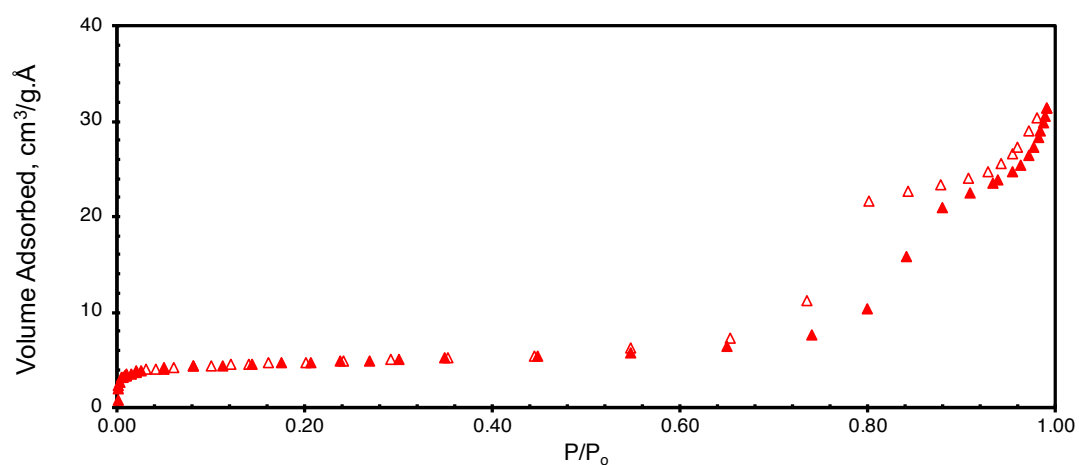
Figure 5.35. Nitrogen physisorption isotherm of TPA@Cu-Zn@EMA bifunctional DME catalyst (filled symbols: adsorption and empty symbols: desorption branches)
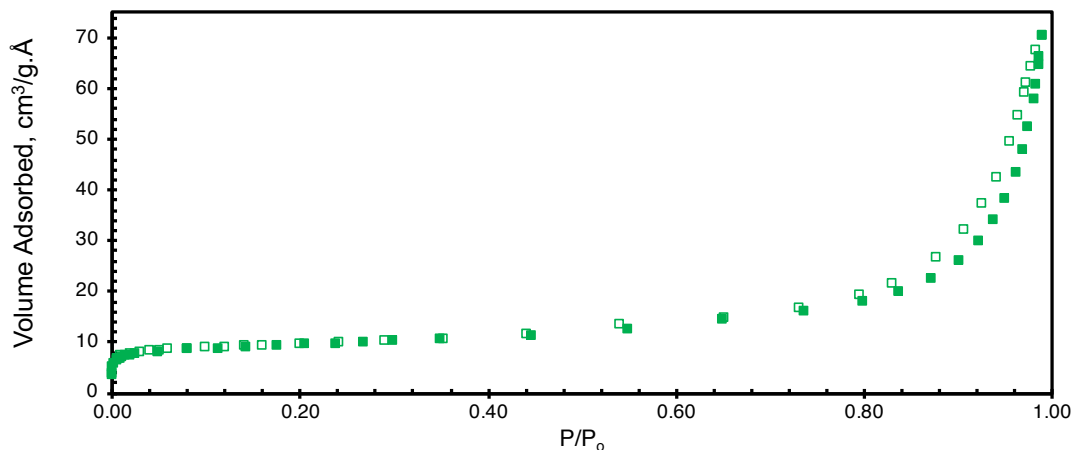
Figure 5.36. Nitrogen physisorption isotherm of TPA@Cu-Zn@CMK-3 bifunctional DME catalyst (filled symbols: adsorption and empty symbols: desorption branches)

Pore size distributions of the bifunctional DME synthesis catalysts are given in Figure 5.37-Figure 5.38 and physical properties of these catalysts are tabulated in Table 5.9. N_2 adsorption pore volume decreased significantly after TPA and Cu-Zn loading compared to the pore size distribution of EMA support. This is an indication of decreasing of pore volumes and surface areas.
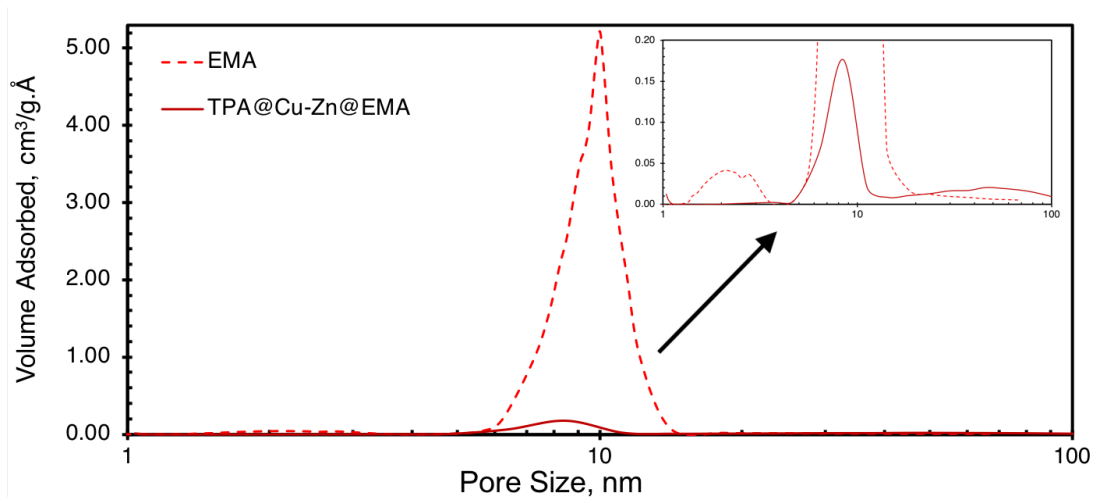
Figure 5.37. BJH desorption pore size distributions of EMA support and TPA@Cu-Zn@EMA bifunctional DME catalyst

TPA@Cu-Zn@CMK-3 catalyst showed bimodal pore size distribution. Average pore diameters were 3.9 nm and 38.5 nm. It was seen that mesopores around 3.5nm in the structure of CMK-3 support were mainly blocked and pores in the macropore range became dominant. This result is in good agreement with Table 5.9. Microporosity of CMK-3 support decreased significantly from 36.4% to 15.1%. This is an indication of metals being placed mainly on micropore and mesopores.
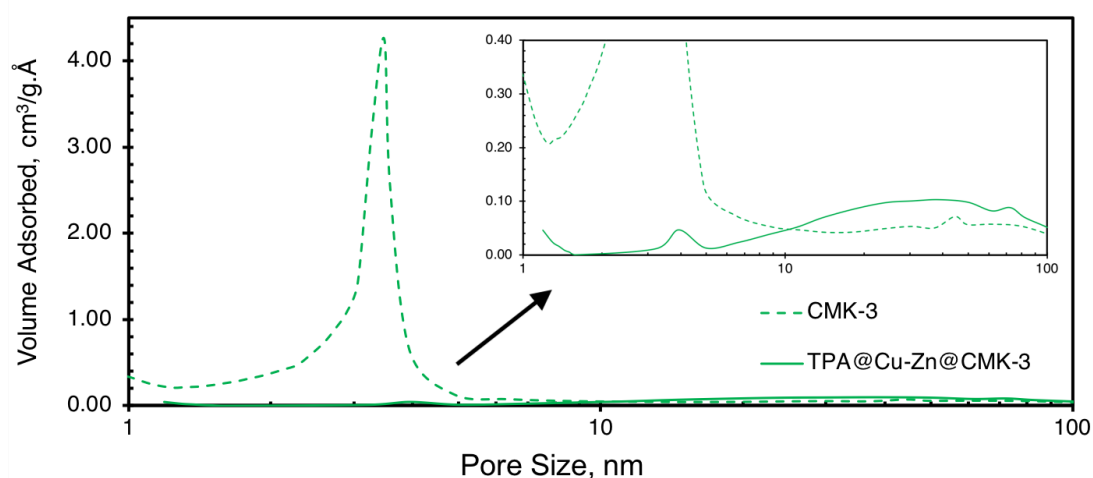
Figure 5.38. BJH desorption pore size distributions of CMK-3 support and TPA@Cu-Zn@CMK-3 bifunctional DME catalyst

The TPA@Cu-Zn@CMK-3 catalyst had surface area of 31 m^2/g, whereas the TPA@Cu-Zn@EMA catalyst had surface area of 15 m^2/g. Both catalysts had the similar microporosity. However, the TPA@Cu-Zn@CMK-3 catalyst had wide range pore size distribution. The properties of TPA@Cu-Zn@CMK-3 were better than that of TPA@Cu-Zn@EMA catalyst.

Furthermore, low calcination temperature (280°C) may also insufficient for removing the impurities from the structures.

Table 5.9. *Physical properties of bifunctional DME synthesis catalysts*

Catalyst	Multipoint BET surface area, m^2/g	BJH Des. pore volume, cm^3/g	BJH Des. avg. pore diameter, nm	Micro porosity, %
TPA@Cu-Zn@EMA	15	0.05	8.45	14.21
TPA@Cu-Zn@CMK-3	31	0.11	3.9 & 38.5	15.10

NH_3-TPD desorption curves of these samples are given in Figure 5.39. TPD curve of TPA@Cu-Zn@EMA was deconvoluted and given in Figure 5.40.

TPA@Cu-Zn@EMA catalyst had five chemical desorption peaks at around 155°C, 257°C, 290°C, 365°C and 530°C. Unlike deconvoluted TPD curve of EMA support and 10TPA@EMA catalyst (Figure 5.23), two additional peaks were observed at 257°C and 290°C in deconvoluted TPD curve of TPA@Cu-Zn@EMA. Observed peaks at around 155°C, 365°C and 530°C were coming from the EMA support. These two peaks might be coming from the Cu-Zn loading. However, it is important to underline that, the possibility of having mass transfer resistance because of the complex structure and re-adsorption phenomena during TPD analysis may also lead to have these two additional peaks. Further investigation should be carried out either using UHV chamber with different exposures and monolayer parameters or flow set-up with different flow rate-to-sample ratio to ensure that there is no re-adsorption phenomena.

TPA@Cu-Zn@CMK-3 catalyst had one main peak at around 535°C. The rapid drop at around 535°C is the evident that all ammonia molecules have desorbed.This type of behaviour was observed when the desorption order is zeroth order. Hence, the desorption of ammonia is independent from the coverage and the desorption rate increases exponentially with the temperature.
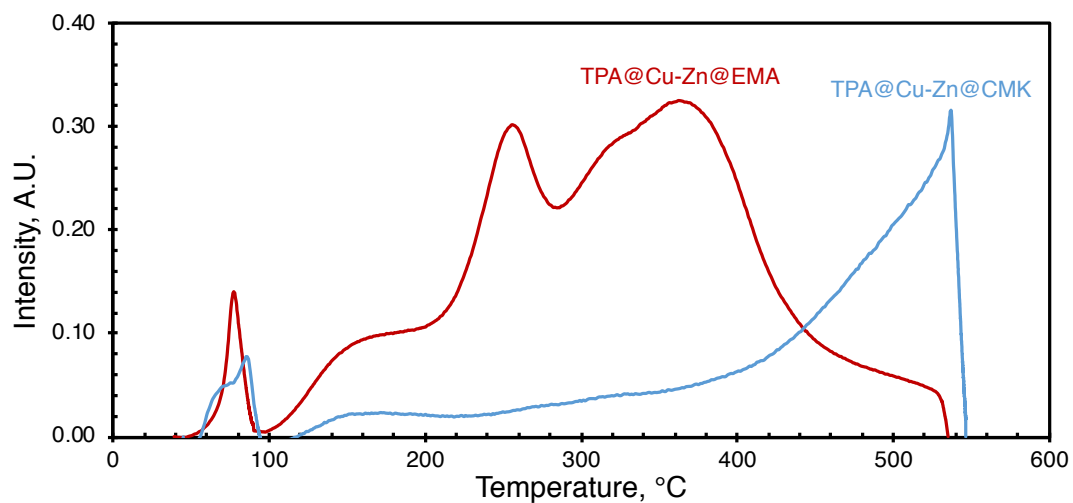
Figure 5.39. NH₃-TPD curves of bifunctional DME catalysts
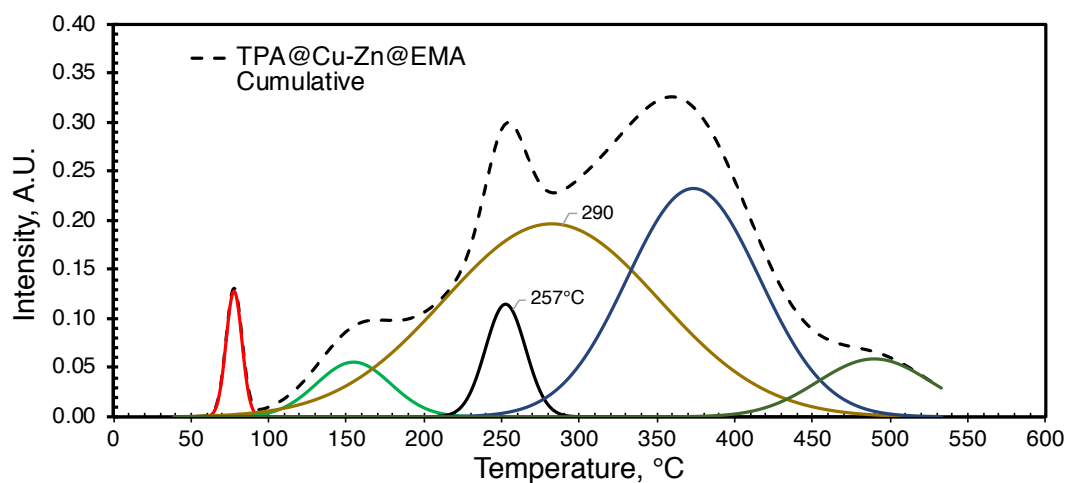
Figure 5.40. Deconvoluted TPD curve of TPA@Cu-Zn@EMA catalyst (dashed lines represents cumulative curves, solid lines represents deconvoluted peaks)

Total acid capacities of the catalysts were presented in Table 5.10. It was seen that the TPA@Cu-Zn@EMA catalyst had about 28% more acid capacity than that of the TPA@Cu-Zn@CMK-3 catalyst.

Table 5.10. *Acid capacities of bifunctional DME synthesis catalysts*

Catalyst	Total Acid Capacity, mmol/g
TPA@Cu-Zn@EMA	1.25
TPA@Cu-Zn@CMK-3	0.94

SEM and backscattered electron images of bifunctional TPA@Cu-Zn@EMA at different magnifications are presented in Figure 5.41-Figure 5.42. Differences in micro-structures between EMA support (Figure 5.11) and TPA@Cu-Zn@EMA is clearly seen. This is due to high TPA and Cu-Zn content in the material. However, images in the red rectangular in the SEM images of TPA@Cu-Zn@EMA had the same morphology as the EMA support. This result is in good agreement with the backscattered images since backscattered electron images of these region had a less brightness, indicating no metal was loaded into these region. In both backscattering images, TPA and Cu-Zn metals were dispersed on the EMA support. These SEM images were taken before the reduction process. Thus, less bright regions were observed since copper was in oxide form.
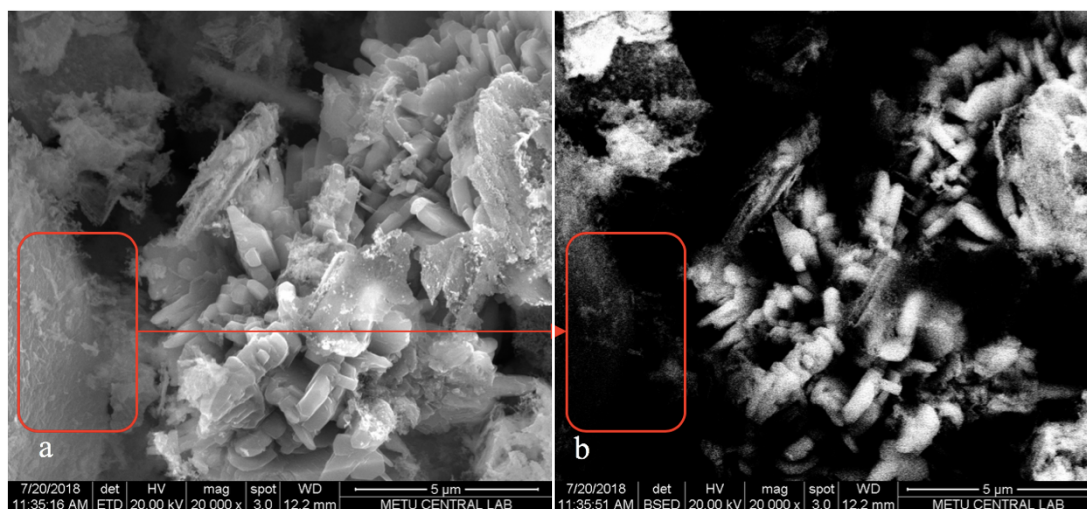
Figure 5.41. SEM (a) image and backscattered (b) images of TPA@Cu-Zn@EMA catalyst at 20,000 magnification
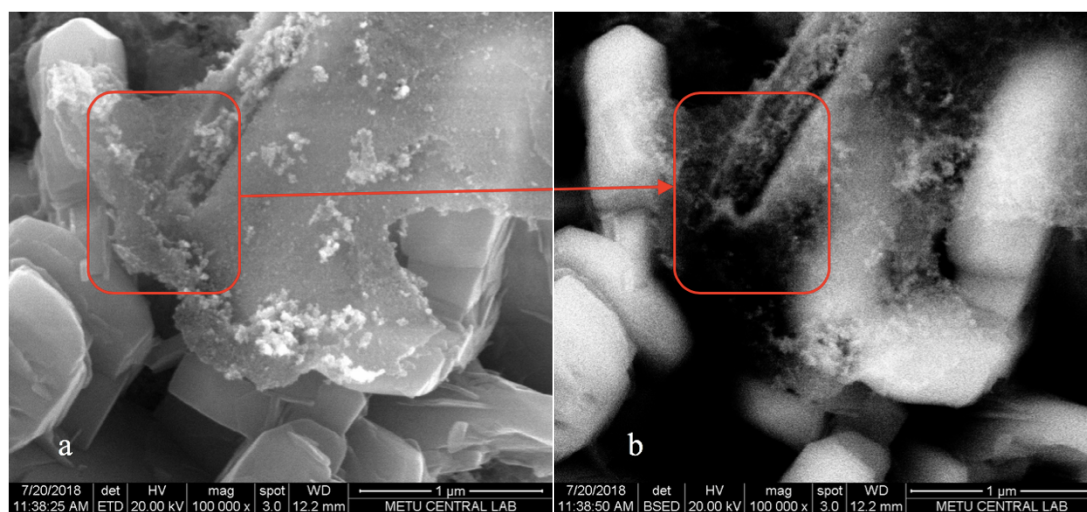
Figure 5.42. SEM (a) and backscattered electron (b) images of TPA@Cu-Zn@EMA catalyst at 100,000 magnification

EDX spectrum of this sample is given in Figure 5.43. Al, O, Cu, Zn, W peaks were observed in the EDX spectrum. W, Cu, Zn loaded to the catalyst and Al coming from the support are the elements in the material.
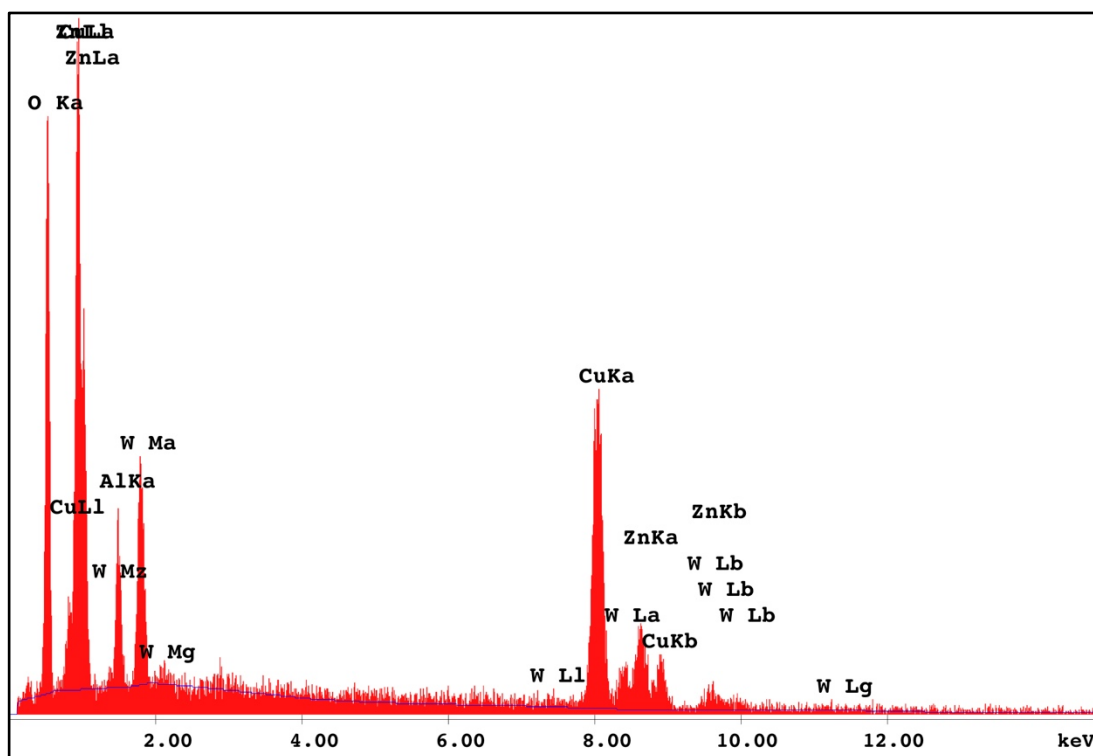
Figure 5.43. EDX spectrum of the TPA@Cu-Zn@EMA catalyst

SEM and backscattered images of the TPA@Cu-Zn@CMK-3 catalyst at different magnifications are presented in Figure 5.44-Figure 5.45. SEM images of TPA@Cu-Zn@CMK-3 (Figure 5.44a and Figure 5.45a) revealed that morphology of CMK-3 support (Figure 5.33) was completely changed after Cu, Zn and TPA loading.

The less bright images in the red rectangular shapes in the backscattered electron images (Figure 5.44b and Figure 5.45b) indicates the absence of Cu-Zn and TPA in these regions. These regions had the similar morphology with the CMK-3 support (Figure 5.33). However, cluster of metals were also not observed in the backscattered electron images of the TPA@Cu-Zn@CMK-3 catalyst.
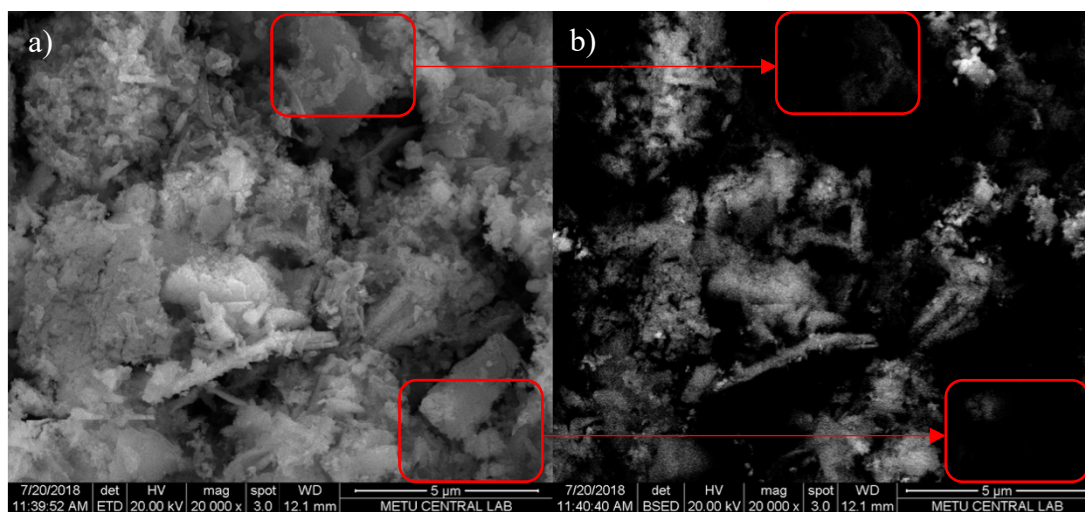
Figure 5.44. SEM (a) and backscattered electron (b) images of TPA@Cu-Zn@CMK-3 catalyst at 20,000 magnification
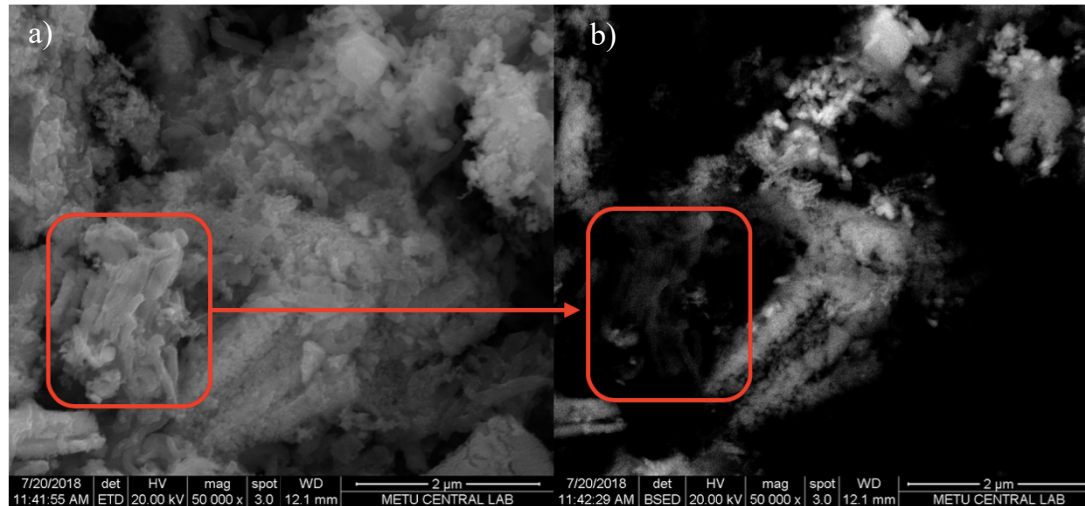
Figure 5.45. SEM (a) and backscattered electron (b) images of TPA@Cu-Zn@CMK-3 catalyst at 50,000 magnification

EDX spectrum of this sample is given in Figure 5.46. Cu, Zn and W loaded to the catalyst and C coming from the CMK-3 support were the elements available in the material.
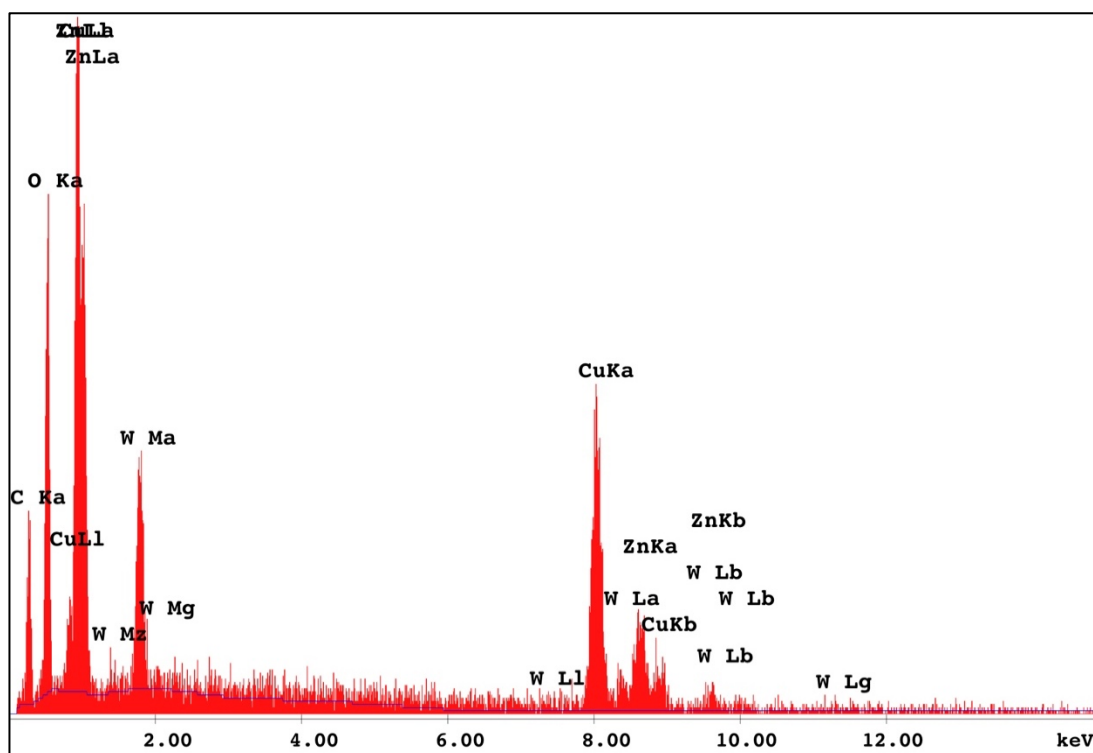
Figure 5.46. EDX spectrum of the TPA@Cu-Zn@CMK-3 catalyst

Elemental compositions of the bifunctional catalysts are given in Table 5.11. Aluminum and some of oxygen content of the TPA@Cu-Zn@EMA catalyst was coming from the alumina support. Since copper and zinc were oxidized after calcination, rest of oxygen content was coming from metal oxides and TPA. All oxygen content of the TPA@Cu-Zn@CMK-3 catalyst was coming from TPA and oxide forms of copper and zinc since CMK-3 support consists of pure carbon. That was the reason that the TPA@Cu-Zn@CMK-3 catalyst contained less oxygen than

101

the TPA@Cu-Zn@EMA catalyst. EDX results proved that TPA and Cu-Zn metals successfully loaded to both mesoporous alumina and mesoporous carbon supports.

Zn content of the two catalyst was very close, whereas Cu and W content of the TPA@Cu-Zn@EMA catalyst was higher than that of the TPA@Cu-Zn@CMK-3 catalyst.

Table 5.11. *Elemental compositions of bifunctional catalysts*

Catalyst Element	TPA@Cu-Zn@EMA	TPA@Cu-Zn@CMK-3
	wt. %	
Al	4.62	-
C	-	21.14
O	19.07	16.65
Cu	43.47	34.51
Zn	13.64	14.37
W	19.19	13.33

5.2. DME Production Results

Catalyst performance tests were carried out using DME production system at 275°C, 50 bar and 5000 ml/h.gcat GHSV unless otherwise stated. In the catalytic performance tests, effect of reaction parameters (reaction temperature, GHSV, feed gas composition) on selectivity of DME was also investigated. Reduction procedure was carried out at 275°C before the performance tests, unless otherwise stated. Reaction time for DME production was 5 hours. Reactor effluent streams were analyzed

continuously using GC and the outlet stream compositions were calculated using the calibration factors of the components.

Fractional conversion for CO and product selectivities were calculated. In case of CO_2 containing syngas feed, total fractional conversion (CO and CO_2) was calculated. Conversion and selectivity calculation methods are given in Appendix E. Average conversion and selectivity values were calculated using the last 5 data points where the system reached steady state.

Preliminary DME production experiments were conducted at 275°C, 50 bar and 5000 ml/h.gcat GHSV over MSC and CA (1/1 wt. ratio) catalysts. From the GC analysis, the chemical composition of the reactor stream was evaluated. In addition to the carbon monoxide and hydrogen gases, the formation of CH_4, CO_2, HCOOH (formic acid), CH_3OH (methanol), DME and C_2H_5OH (ethanol) were detected as products in the effluent stream of the reactor. The presence of those gases showed that the following reactions may take place in the reactor.

$CO + 2H_2 \leftrightarrow CH_3OH$ (R1)

$CO_2 + 3H_2 \leftrightarrow CH_3OH + H_2O$ (R2)

$2CH_3OH \leftrightarrow CH_3OCH_3 + H_2O$ (R3)

$CO + H_2O \leftrightarrow CO_2 + H_2$ (R4)

$CO_2 + H_2 \leftrightarrow HCOOH$ (R10)

$2CO + 4H_2 \leftrightarrow C_2H_5OH + H_2O$ (R11)

$CO + 3H_2 \leftrightarrow CH_4 + H_2O$ (R12)

Besides main products, namely: methane, carbon dioxide, methanol and dimethyl-ether, trace amount of formic acid and ethanol were also observed. Both ethanol and

formic acid mole fractions were not more than 0.28% in any physically mixed catalyst tests that were carried out at 275°C. Therefore, selectivities of these products were not shown in the figures, unless otherwise stated.

In all catalytic reaction tests carried out at 275°C temperature with CO and H_2 mixture, maximum ethanol and formic acid were found to be 1.6% and 4.4%, respectively over the TPA@Cu-Zn@EMA catalyst at a pressure of 50 bar and GHSV of 5000 ml/h.gcat.

5.2.1. Repeatability Tests Results

DME production experiments were carried out three times to check whether experiments were repeatable or not. Experiments were conducted over a mixture of MSC and CA catalysts with a weight ratio of 1:1 at the temperature of 275°C, the pressure of 50 bar, the GHSV of 5000 ml/h.gcat. Using conversion values of three runs, standard deviation was calculated. The average CO conversion of these three runs with the standard deviation was plotted as a function of time (Figure 5.47).

Results showed that system reached steady state within 100 minutes. Average fractional CO conversion of three experiments was 70%. The DME production system is consistent and these results are in agreement with each other. In other words, it produces repeatable results.
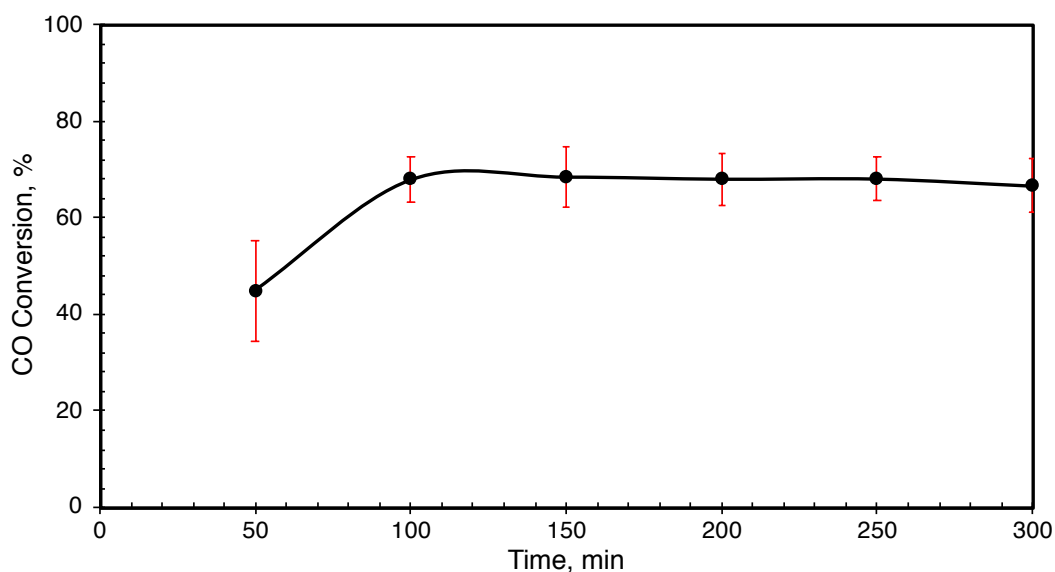
Figure 5.47. Average CO conversion of three runs with respect to time for DME repeatability tests (P: 50 bar, T: 275°C, $H_2/CO= 1/1$, GHSV: 5000 ml/h.gcat, Catalyst: MSC + CA (1/1 by wt.))

Average product distribution of three runs with standard deviation is given in Figure 5.48. The same products obtained from the preliminary tests were observed in the reactor effluent stream and the same products were also formed in the repeated experiments. Product distribution also confirms that the system reaches steady state within 100 minutes and product distribution results were also in consistency with each other.

Average product selectivities of the three repeated tests with standard deviation are given in Figure 5.49. In all three experiments, product selectivity results were close to each other. Average DME selectivity was 53% whereas average CO_2 selectivity was about 33%.

For all three test results, error percentage was not more than 5%. Products other than DME and methanol, showed that side reactions also occur in the reactor. Formation

105

of CO_2 was due to water-gas shift reaction and CH_4 formed from the methanation reaction.
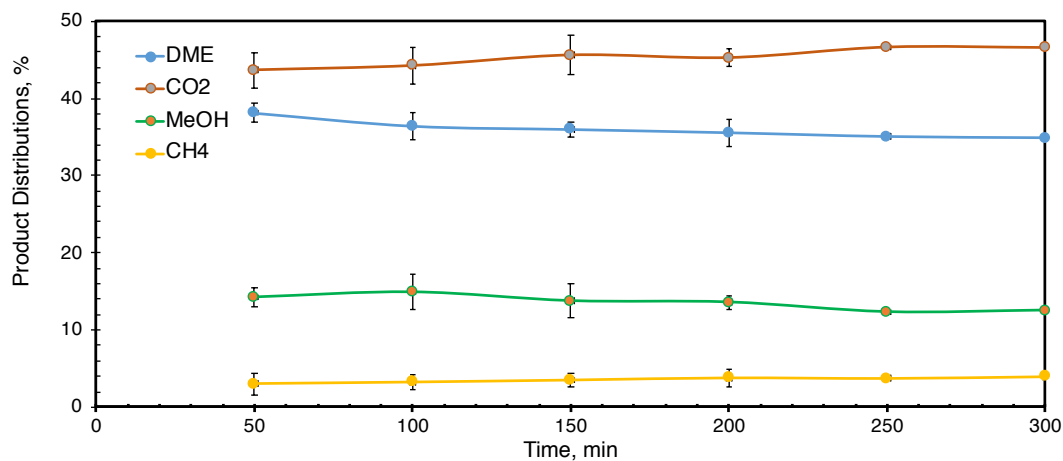
Figure 5.48. Product distribution of three runs with respect to time for DME repeatability tests (P: 50 bar, T: 275°C, $H_2/CO= 1/1$, GHSV: 5000 ml/h.gcat, Catalyst: MSC + CA (1/1 by wt.))
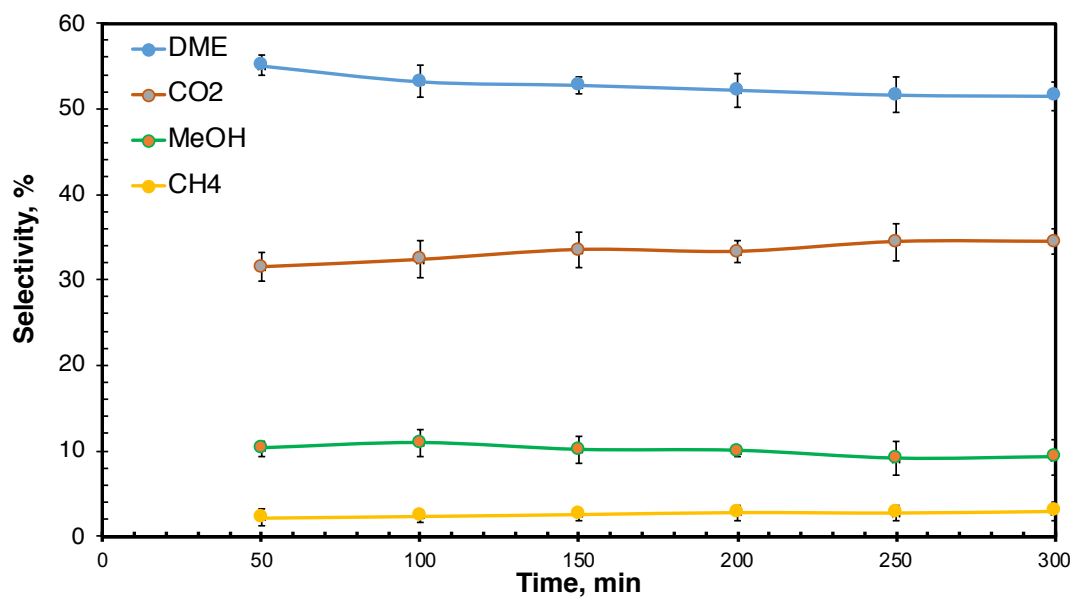
Figure 5.49. Product selectivities of three runs with respect to time for DME repeatability tests (P: 50 bar, T: 275°C, $H_2/CO= 1/1$, GHSV: 5000 ml/h.gcat, Catalyst: MSC + CA (1/1 by wt.))

5.2.2. Synergic Effect of Single-step DME Synthesis on Thermodynamic Limitation

Methanol formation is highly limited by the thermodynamic limitations as discussed in Chapter 3. In the single-step DME synthesis, metallic site of the bifunctional catalyst triggers the methanol formation and the methanol is dehydrated instantaneously over the acid sites of the bifunctional catalyst. Consumption of the methanol in R3 enhances R1 and water produced from R3 is consumed in WGS reaction and hydrogen formed from R4 enhances R1 which is called a synergic effect.

Single-step DME synthesis from syngas in the same reactor uses the synergic effect and shifts the thermodynamic equilibrium towards the products.

$$CO + 2H_2 \leftrightarrow CH_3OH \tag{R1}$$

$$2CH_3OH \leftrightarrow CH_3OCH_3 + H_2O \tag{R3}$$

$$CO + H_2O \leftrightarrow CO_2 + H_2 \tag{R4}$$

Three different tests were completed to demonstrate the effect of bifunctional catalysts to overcome thermodynamic limitation under the same conditions. In the first test, only methanol was synthesized over commercial methanol synthesis catalyst. In the second and third tests, MSC was physically mixed with synthesized EMA catalyst or commercial alumina catalyst and used in the single-step DME synthesis, respectively. Tests were performed at constant GHSV values and catalysts were mixed 1/1 (wt./wt.) CO conversion values obtained from three different catalysts are given in Figure 5.50.

For the MSC catalyst, average CO conversion was approximately 14%. When the MSC catalyst was mixed with the EMA catalyst, average CO conversion value increased by 2.4 times. For the mixture of MSC & CA catalysts, average CO conversion increased by 2 times compared to the MSC & EMA catalyst mixture.
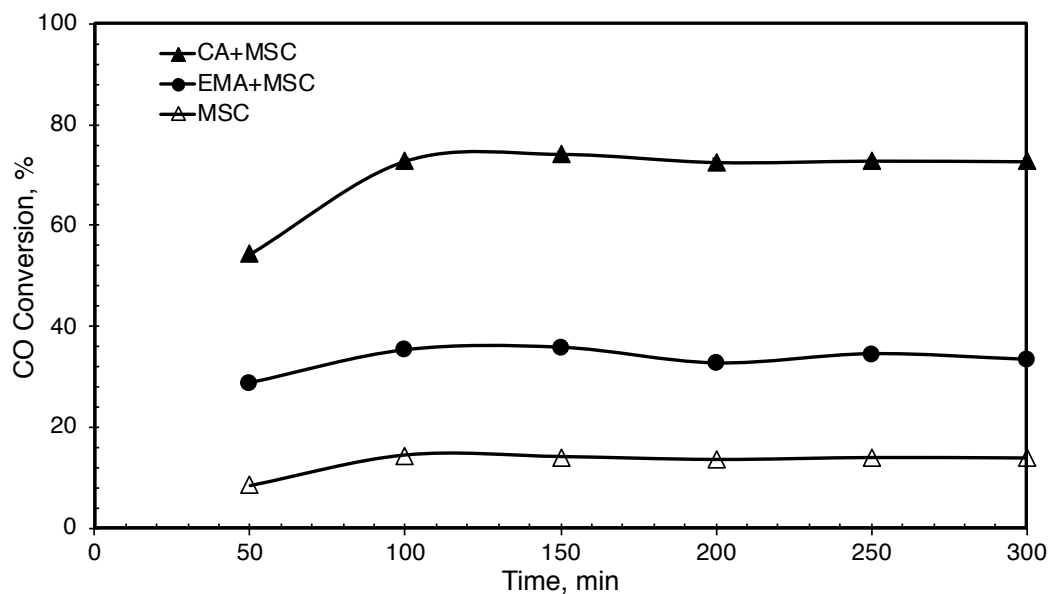
Figure 5.50. Effect of single-step DME synthesis on CO conversion over different catalysts (P: 50 bar, T: 275°C, $H_2/CO= 1/1$, GHSV: 5000 ml/h.gcat).

Average product selectivites are given in Figure 5.51. Methanol, CH_4 and CO_2 gases were observed in the presence of the MSC catalyst. Due to absence of acid sites in the catalyst, trace amount of DME formed, as expected. Main reactions taking place in the reactor were R1, R4, and R12. With the use of methanol dehydration catalysts, CO conversion increased from 14% to 33% and 70% depending on type of methanol dehydration catalyst. Furthermore, methanol selectivity decreased and CO conversion and DME selectivity increased significantly. This result showed that methanol dehydration (R3) became dominant in the reactor, and the presence of acid sites in the catalyst promoted the WGS reaction to produce CO_2.

108

$$CO + 2H_2 \leftrightarrow CH_3OH \qquad\qquad\qquad\qquad (R1)$$

$$2CH_3OH \leftrightarrow CH_3OCH_3 + H_2O \qquad\qquad\qquad (R3)$$

$$CO + H_2O \leftrightarrow CO_2 + H_2 \qquad\qquad\qquad\qquad (R4)$$

$$CO + 3H_2 \leftrightarrow CH_4 + H_2O \qquad\qquad\qquad\quad (R12)$$

Both MSC+CA and MSC+EMA catalyst couples showed similar DME selectivity values. However, CO conversion value in the presence of MSC+CA catalyst, was higher than the CO conversion value in the presence of MSC+EMA catalyst. Therefore, the CA catalyst was more active compared to the EMA catalyst. Both alumina based catalysts had physical and structural differences. The EMA catalyst was in amorphous structure, whereas the CA catalyst was in γ-alumina phase. It is known that the crystalline phase of the alumina effects its physical properties. EMA catalyst was superior than CA in terms of surface area and total pore volume and both catalyst had similar pore size. Total acid capacity of the EMA catalyst was higher than the CA catalyst, however the CA catalyst had a higher peak end temperature at around 550°C which is an indication of stronger acidity. These results showed that the acid strength and crystal structure of the alumina catalyst may effect the methanol dehydration.
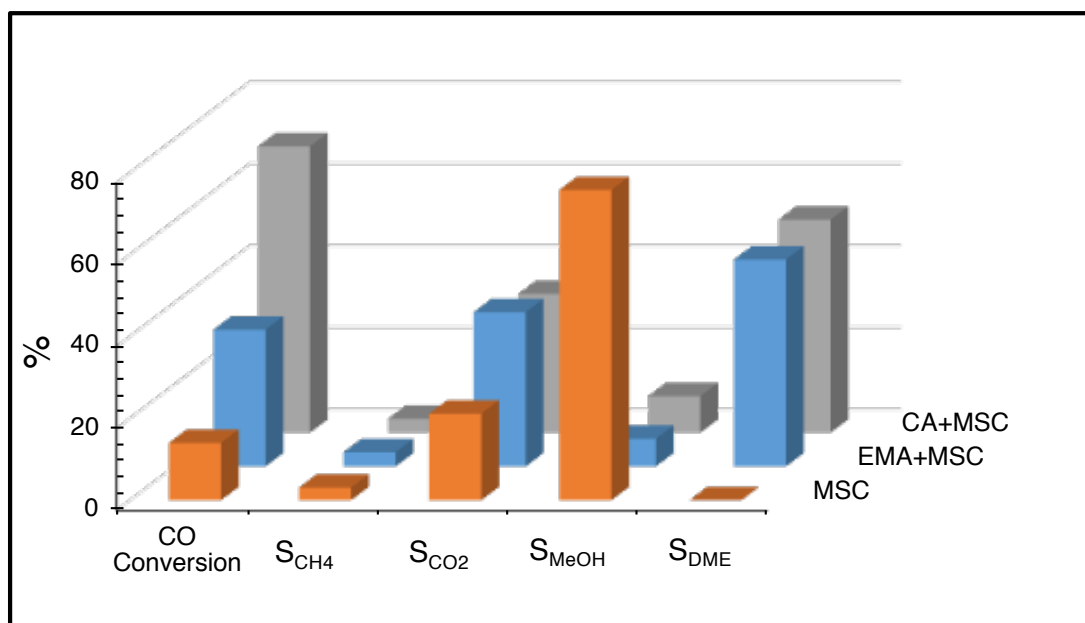
Figure 5.51. Effect of single-step DME synthesis on product selectivites over different catalysts (P: 50 bar, T: 275°C, $H_2/CO= 1/1$, GHSV: 5000 ml/h.gcat)

CO conversion values obtained using the MSC and MSC+CA catalysts and the equilibrium conversion values are presented in Figure 5.52. CO conversion values were close to equilibrium conversion values in both cases (only methanol synthesis and single-step DME synthesis). However, the enhancement in CO conversion value for the single-step DME synthesis showed the synergic effect of single-step DME synthesis.
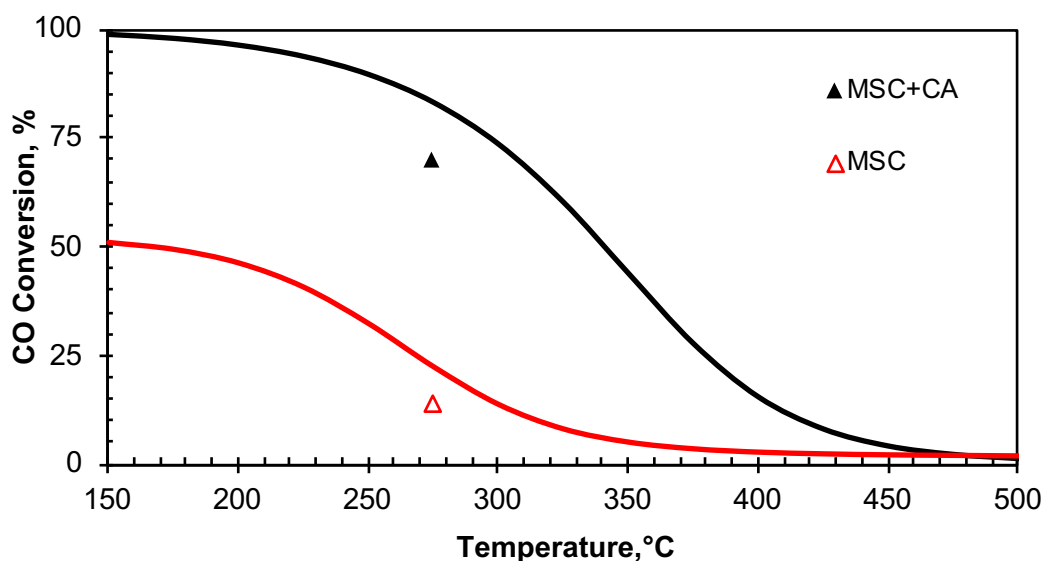
Figure 5.52. Comparison of CO conversion values obtained using the MSC and MSC+CA catalysts with the equilibrium conversion values (P: 50 bar, T: 275°C, H$_2$/CO= 1/1, GHSV: 5000 ml/h.gcat, red: methanol synthesis equilibrium and black: DME synthesis equilibrium conversion curve)

5.2.3. Effect of Reaction Temperature on DME Production

According to Arrhenius' Law, reaction rate increases as a function of temperature independent from the reaction enthalpy. However, increase in the reaction rate depends on the activation energy of the reaction. Mass and heat transfer dynamics may also play a significant role during the reaction. Therefore, effect of reaction temperature on CO conversion and product selectivity using MSC+CA catalyst mixture at a temperature range of 200-350°C under 50 bar pressure and 5000 ml/h.gcat GHSV was investigated and the results are given in Figure 5.53.

Formation of CO$_2$, methanol and DME and trace amount of methane and ethanol at 200°C temperature was the evidence of methanol formation (R1), methanol dehydration (R3), WGS (R4), methanation (R12) and ethanol formation (R8) reactions taking place in the reactor. Furthermore, methanol formation was the dominant reaction at 200°C. DME selectivity and CO$_2$ selectivity increased significantly at 250°C and 275°C temperatures. Formation of formic acid showed that R7 was also

taking place at these temperatures. CO conversion increased with an increase in temperature. On the contrary of CO conversion, DME selectivity increased up to 275°C, then it started to decrease. It is important to notice that R4, R7, R8, and R12 reactions were taking place dominantly in the reactor at 350°C. Moreover, WGS reaction had the highest reaction rate at 350°C, since CO_2 had the highest selectivity.
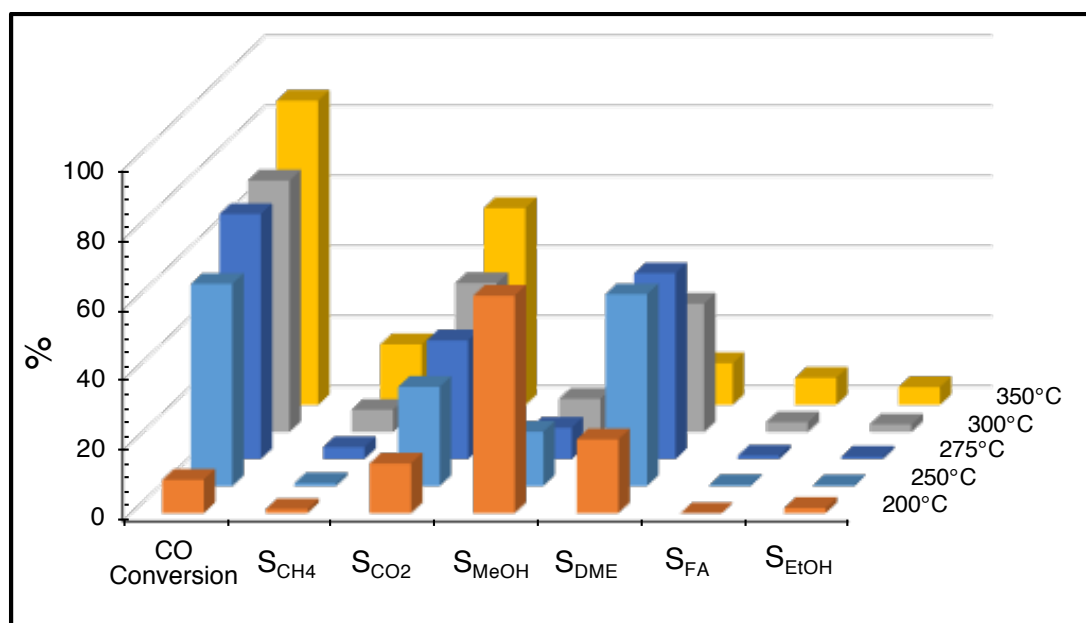
Figure 5.53. Effect of reaction temperature on CO conversion and product selectivities (P: 50 bar, H_2/CO= 1/1, GHSV: 5000 ml/h.gcat, Catalyst: MSC+CA (1/1 by wt.))

$$CO + 2H_2 \leftrightarrow CH_3OH \tag{R1}$$

$$2CH_3OH \leftrightarrow CH_3OCH_3 + H_2O \tag{R3}$$

$$CO + H_2O \leftrightarrow CO_2 + H_2 \tag{R4}$$

$$CO_2 + H_2 \leftrightarrow HCOOH \tag{R7}$$

$$2CO + 4H_2 \leftrightarrow C_2H_5OH + H_2O \tag{R8}$$

$$CO + 3H_2 \leftrightarrow CH_4 + H_2O \tag{R12}$$

Figure 5.54 represents the experimental CO conversion values and equilibrium conversion values as a function of reaction temperature. Equilibrium calculations were done using methanol formation (R1 and R2), methanol dehydration (R3) and WGS (R4) reactions. Therefore, CO conversion value at 350°C was not plotted on the figure since side reactions were not included in the equilibrium conversion calculations. Results revealed that, conversion values are getting closer to the equilibrium value with an increase in the reaction temperature and CO conversion value at 300°C almost reached equilibrium value.

$$CO + 2H_2 \leftrightarrow CH_3OH \qquad \Delta Hrxn = -90 \text{ kJ/mol} \qquad (R1)$$

$$CO_2 + 3H_2 \leftrightarrow CH_3OH + H_2O \qquad \Delta Hrxn = -49 \text{ kJ/mol} \qquad (R2)$$

$$2CH_3OH \leftrightarrow CH_3OCH_3 + H_2O \qquad \Delta Hrxn = -25 \text{ kJ/mol} \qquad (R3)$$

$$CO + H_2O \leftrightarrow CO_2 + H_2 \qquad \Delta Hrxn = -41 \text{ kJ/mol} \qquad (R4)$$
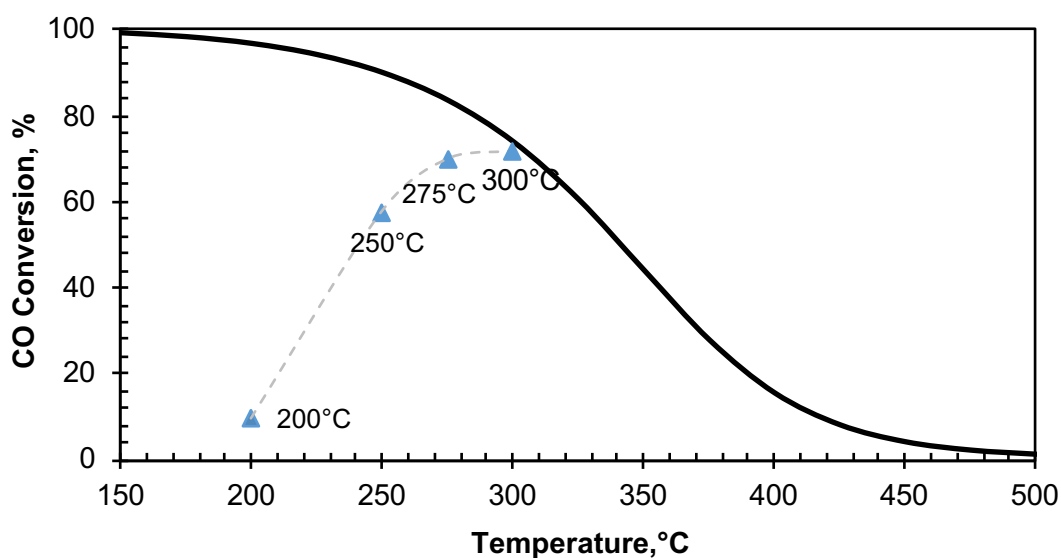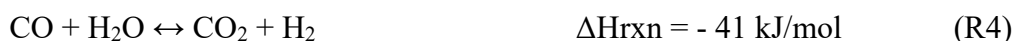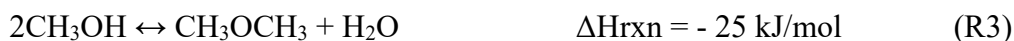
Figure 5.54. Effect of temperature on CO conversion and CO equilibrium conversion (P: 50 bar, H₂/CO= 1/1, GHSV: 5000 ml/h.gcat, Catalyst: MSC+CA (1/1 by wt.)) (Triangle symbols: experimental CO conversion values)

113

Figure 5.55 shows the effect of reaction temperature on CO conversion and DME selectivity, which reveals the optimum operating reactor temperature for DME synthesis. DME selectivity gave a maximum between 250°C and 275°C and decreased drastically after 275°C. CO conversion increased significantly from 10% to 58% when temperature increased from 200°C to 250°C, but a slight increase in CO conversion was observed between 250°C and 300°C. These results indicated that the optimum operating temperature for the single-step DME synthesis was between 250-275°C, which are in good agreement with the literature as discussed in Chapter 3. Hence the optimum operating temperature of the reactor was selected as 275°C due to high DME selectivity.

Consumption of two moles of CO for one mole of ethanol formation enhances the CO conversion, whereas consumption of four moles of H_2 for one mole ethanol formation enhances WGS reaction, which also increases the CO conversion. This is the reason of significant increase in the CO conversion value at 350°C
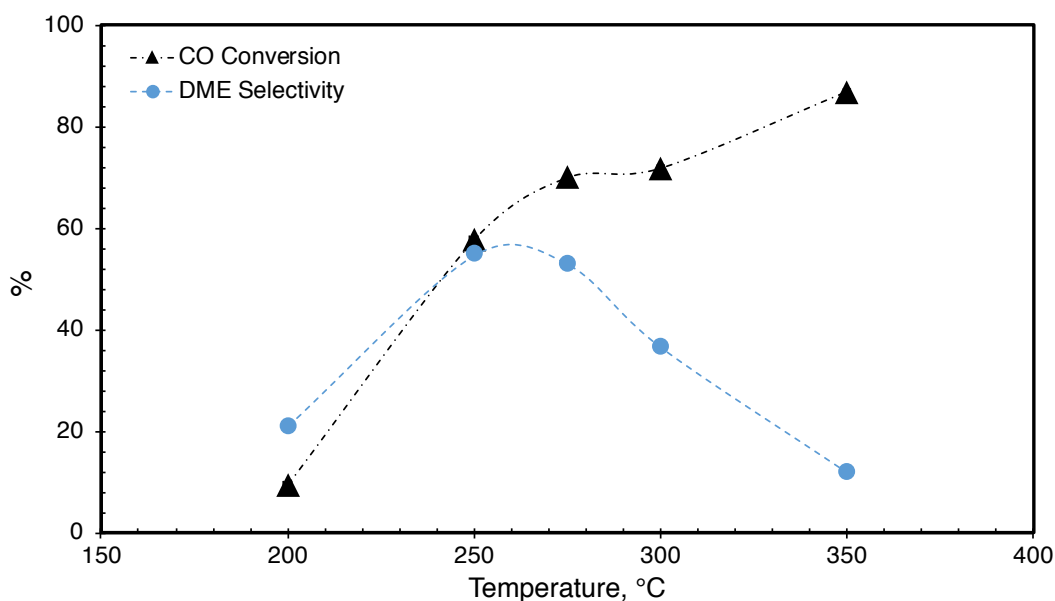
Figure 5.55. Temperature effect on CO conversion and DME selectivity (P: 50 bar, H_2/CO= 1/1, GHSV: 5000 ml/h.gcat, Catalyst: MSC + CA (1/1 by wt.))

Maximum ethanol and formic acid selectivity in all performance tests were found to be 7.8% and 5.2%, respectively over commercial methanol synthesis (MSC) and commercial γ-alumina (CA) catalyst mixture with 1:1 ratio at a temperature of 350°C, a pressure of 50 bar and GHSV of 5000 ml/h.gcat.

5.2.4. Effect of Reduction of Catalyst on DME Production

XRD pattern of MSC showed that Cu and Zn metal sites on the methanol synthesis catalysts are in oxide form. It is known that metallic Cu sites are more active in the methanol formation. Therefore, two activity tests were conducted with non-reduced and reduced MSC and EMA catalyst mixture at 275°C and 50 bar (Figure 5.56) to investigate the effect of reduction of the catalyst on CO conversion and selectivity. 70% CO conversion was obtained over the reduced MSC and EMA catalyst mixture, whereas 19.4% CO conversion was obtained over the non-reduced MSC and EMA catalyst mixture. CO conversion results over reduced and non-reduced catalysts revealed that either non-reduced MSC catalyst that contained both CuO and Cu_2O sites was slightly capable of catalyzing methanol production or non-reduced MSC catalyst has also some metallic Cu sites. However, reduced catalyst was much more active than the non-reduced one due to the presence of more active Cu sites, instead of CuO and Cu_2O sites in the catalyst.

Additionally, reduction of MSC catalyst may not occur during the reaction despite the presence of continuous hydrogen flow in the reactor. This might indicate that either high pressure or presence of highly reactive CO hinders the reduction process of copper oxide sites. The negative effect of high total pressure on reduction is also reported in the literature (Pio et al., 2017). They showed that 10 bar reduction pressure significantly had negative effect on the reduction compared to 1 bar pressure.
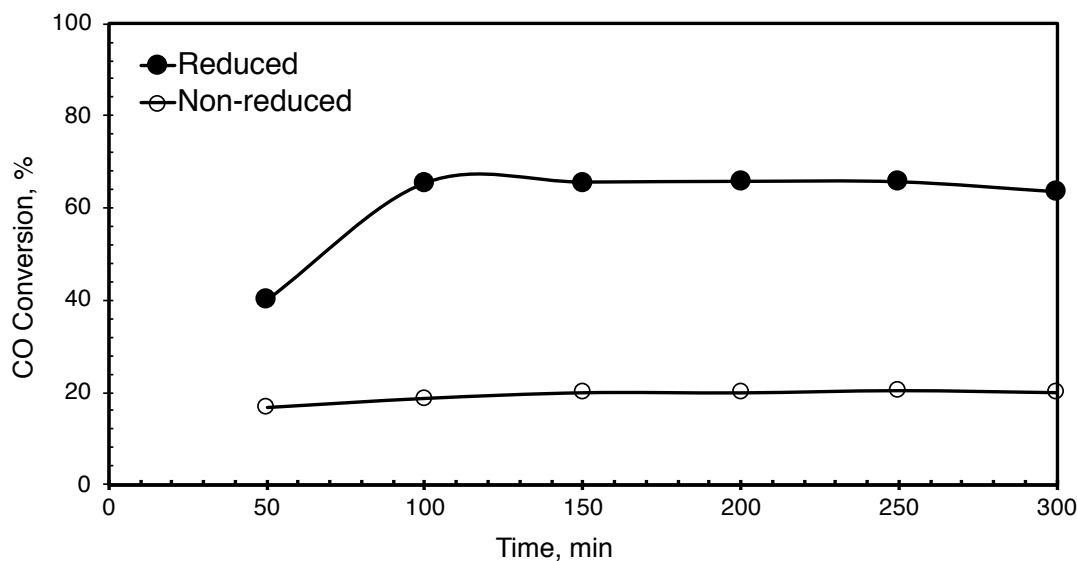
Figure 5.56. Effect of catalyst reduction on CO conversion (P: 50 bar, T: 275°C, $H_2/CO=$ 1/1, GHSV: 5000 ml/h.gcat, Catalyst: MSC + CA (1/1 by wt.)) (Filled symbols: reduced MSC, empty symbols: non-reduced MSC)

Effect of catalyst reduction on product selectivities are given in Figure 5.57. DME selectivity did not change significantly by reducing the catalyst. It can be said that product selectivities were not effected by the reduction of the catalyst and selectivities were close to each other for both case. This might show that methanol formation was catalyzed on Cu sites rather than CuO and Cu_2O sites on the non-reduced catalyst and the lower CO conversion was due to insufficient Cu sites on the non-reduced catalyst. However, the main effect of reduction was seen for the methanation reaction. The non-reduced catalyst was almost incapable of catalyzing the methanation reaction. Lower methane selectivity of non-reduced catalyst might be the reason of its slightly higher DME selectivity than the reduced one. All results were within the experimental error range.

116
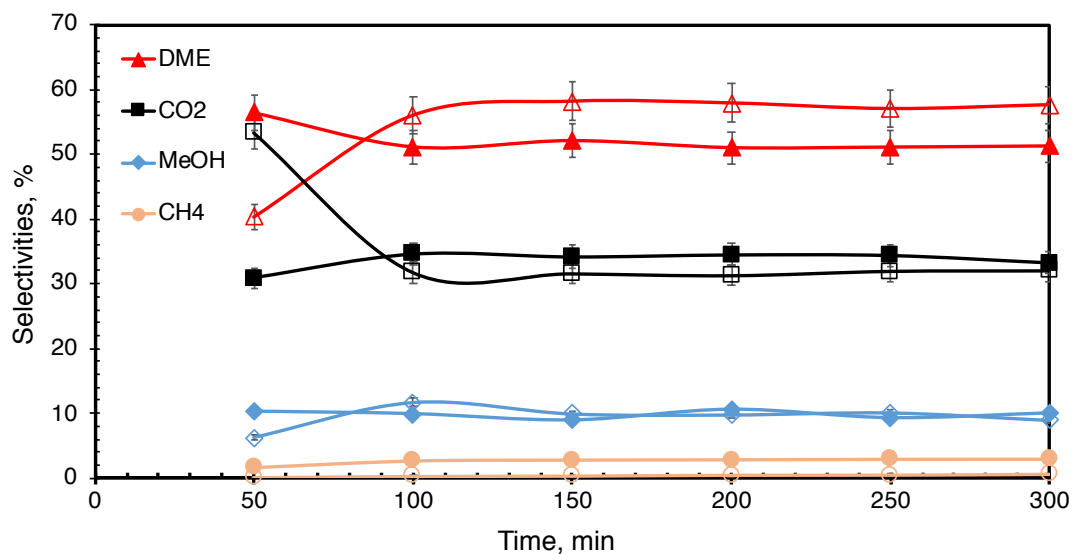
Figure 5.57. Effect of catalyst reduction on product selectivities on single step DME synthesis (P: 50 bar, T: 275°C, H$_2$/CO= 1/1, GHSV: 5000 ml/h.gcat, Catalyst: MSC + CA (1/1 by wt)) (Filled symbols: reduced MSC and empty symbols: non-reduced MSC)

5.2.5. Effect of GHSV on DME Production

DME production experiments in the presence of MSC + CA catalysts were conducted at two different GHSV values (5000 ml/h.gcat and 3333 ml/h.gcat) at 275°C and 50 bar. In order to set GHSV as 3333 ml/h.gcat, 0.45g catalyst mixture was used, instead of 0.3 g catalyst mixture.

The effect of GHSV on CO conversion with the error percentage is given in Figure 5.58. A decrease in GHSV value increased average CO conversion from 69% to 74%, and decreased DME selectivity. CO conversion increased by decreasing GHSV as expected since the average time spent by the reactant molecules in the reactor was longer. However, the difference between two conversion values was not significant. Effect of GHSV on average CO conversion and average product selectivities were also given in Figure 5.59. CO$_2$ and methanol selectivity slightly increased while DME selectivity slightly decreased with a decrease in GHSV. Change in the selectivity of CO$_2$ showed that a decrease in GHSV promotes the WGS reaction more than methanol

formation and methanol dehydration reactions. Overall, a decrease in GHSV did not cause any significant effect on both CO conversion and product selectivities. Considering these results and catalyst economy, the GHSV value of 5000 ml/h.gcat was preferred.
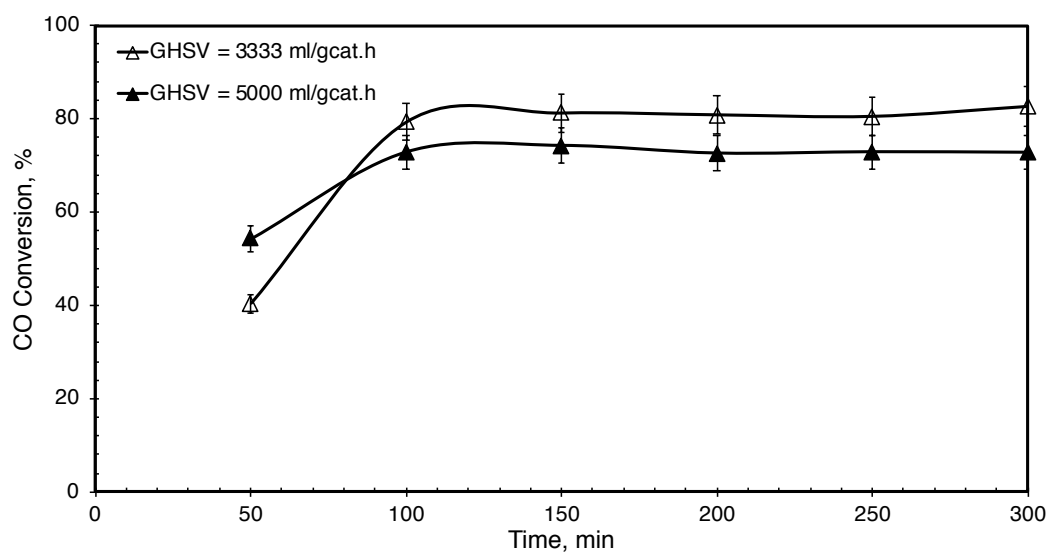
Figure 5.58. Effect of GHSV on CO conversion (P: 50 bar, T: 275°C, H_2/CO= 1/1, Catalyst: MSC + CA (1/1 by wt.))
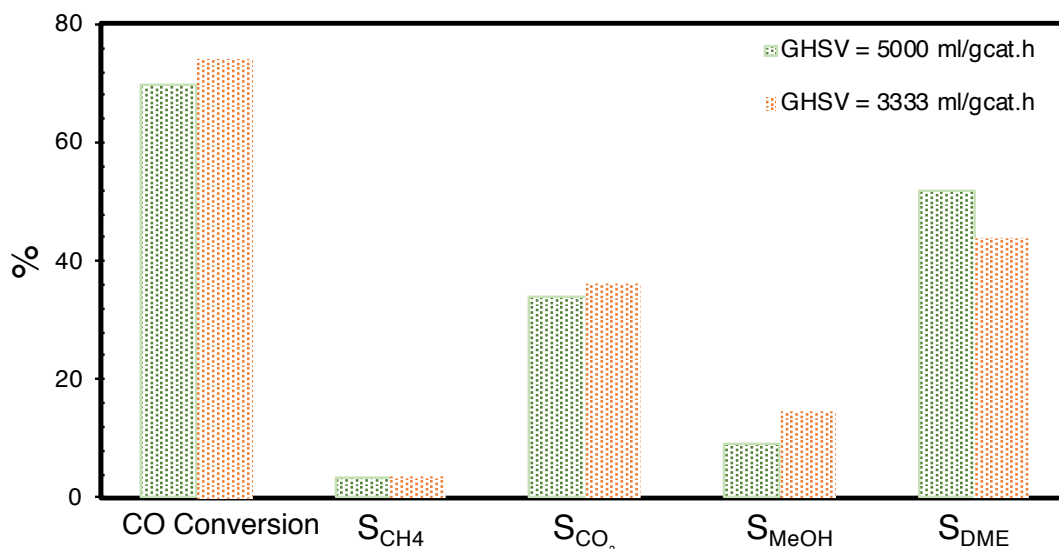
Figure 5.59. Effect of GHSV on average CO conversion and product selectivities (P: 50 bar, T: 275°C, H_2/CO= 1/1, Catalyst: MSC + CA (1/1 by wt.))

5.2.6. Effect of Syngas Composition on DME Production

CO and H_2 mixture is the ideal syngas composition but it also contains different amounts of CO_2 and it is known as a thermodynamically stable molecule. Therefore, CO_2 content in use of the syngas is not preferred because of the thermodynamic limitation. However, different amount of CO_2 is also obtained during the production of syngas in gasification and reforming processes depending on the method, raw material properties, and operation conditions. Conversion of CO_2 containing syngas into fuels, fuel alternatives and green chemicals is also a trending topic and developing technology.

Syngas mixtures containing three different CO_2 were used in the single-step DME synthesis in order to investigate the effect of CO_2 content on the conversion and the DME selectivity. Commercial methanol synthesis catalyst and commercial γ-alumina catalyst mixture were tested with three different molar $CO_2/CO/H_2$ ratio. All three experiments were conducted at 275°C, 50 bar and 5000 ml/h.gcat.

119

Since both CO and CO_2 are reactant in the feed, total $CO\&CO_2$ conversion was calculated and reported in this study. Total conversion values of syngas containing 10% CO_2 ($CO_2/CO/H_2$ = 1/4/5), 25% CO_2 ($CO_2/CO/H_2$ = 1/1/2) and 40% CO_2 ($CO_2/CO/H_2$ = 4/1/5) are given in Figure 5.60. Total $CO\&CO_2$ conversion values for these three mixture were obtained as 34.5%, 14.7%, and 4.7%, respectively. It was seen that with an increase in CO_2 content in the feed caused a decrease in the total conversion.
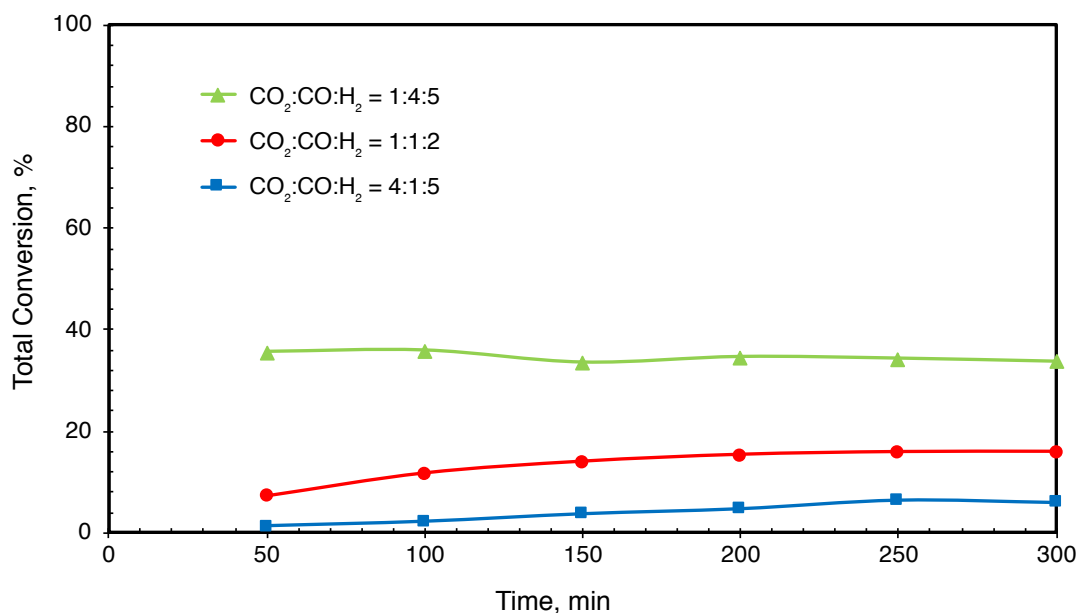
Figure 5.60. Effect of syngas composition on total conversion (P: 50 bar, T: 275°C, $CO_2/CO/H_2$ = 1/4/5, GHSV: 5000 ml/h.gcat, Catalyst: MSC + CA (1/1 by wt.))

These three performance tests using different syngas compositions with CO_2 content are presented in Figure 5.61 along with the product selectivities. It can be clearly seen that the increase in CO_2 content drastically lowers the total conversion under the same conditions. Even so, DME with high selectivity has been produced successfully. In addition, DME selectivities were close to each other in syngas containing 10% and

120

40% CO_2. However, the highest DME selectivity was found to be 78.5% with the syngas containing 25% CO_2. These results showed that Cu-Zn based methanol synthesis catalyst was incapable of activating CO_2 for the methanol synthesis since the increase in CO_2 content of the syngas lower the total conversion. This indicates that development of new methanol synthesis catalyst is required. It also showed that methanation (R12 and R13) reaction rate was increasing with the increase in CO_2 content of the syngas. Water formation in the methanation reaction may also play a negative effect on the methanol dehydration due to thermodynamic limitation.

$$CO + 3H_2 \leftrightarrow CH_4 + H_2O \tag{R12}$$

$$CO_2 + 4H_2 \leftrightarrow CH_4 + 2H_2O \tag{R13}$$
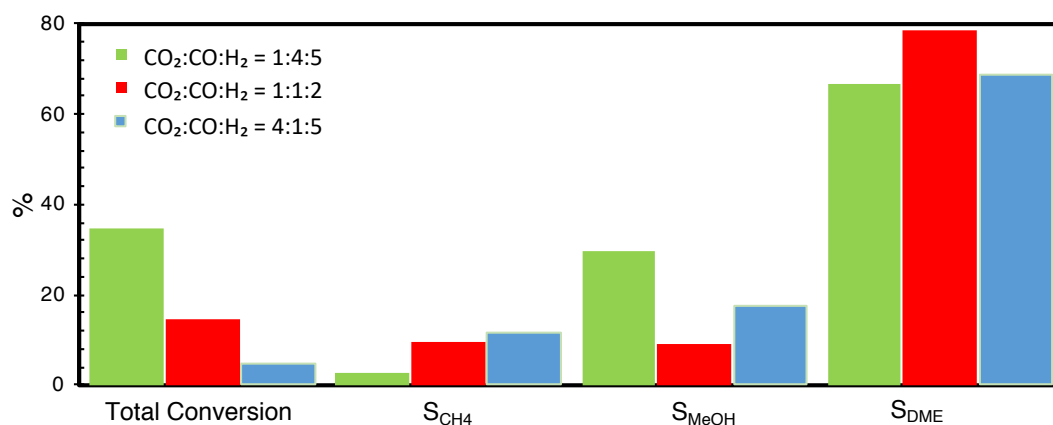
Figure 5.61. Effect of CO_2 content on total conversion and product selectivities (P: 50 bar, T: 275°C, GHSV: 5000 ml/h.gcat, Catalyst: MSC + CA (1/1 by wt.))

Total $CO+CO_2$ experimental conversion values and total equilibrium conversion curve for different syngas compositions are plotted and given in Figure 5.62.

About 4.7%, 14.7% and 34.5% total conversion values were obtained in the feed containing 40%, 25% and 10% CO_2, respectively. Equilibrium conversion values for these feed compositions were 15.5%, 30.6% and 46.6%, respectively. The closest

conversion value to the equilibrium conversion value was observed with the feed containing 10% CO_2 (CO_2/CO/H_2 = 1/4/5).
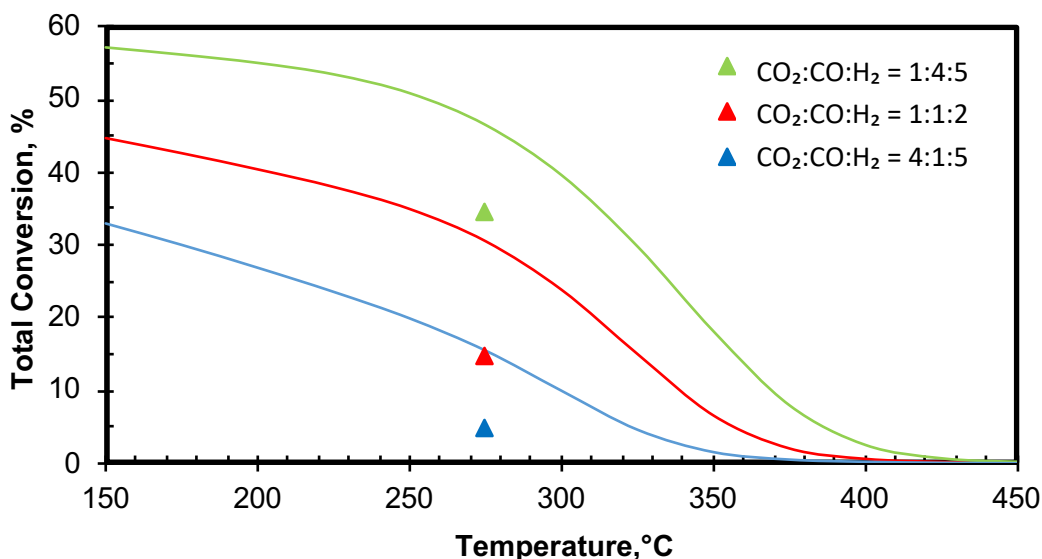
Figure 5.62. Effect of CO_2 content in syngas on total conversion and total equilibrium conversion (P: 50 bar, T: 275°C, GHSV: 5000 ml/h.gcat, Catalyst: MSC+CA (1/1 by wt.)) (Triangle symbols: experimental CO Conversion values)

5.2.7. Comparison of Alumina Catalysts in the Single-Step DME Synthesis

Three different mesoporous alumina, namely commercial alumina, synthesized amorphous alumina and synthesized γ-alumina catalysts were tested without loading any TPA since alumina materials have also acidic nature. CO conversion results of three performance test are given in Figure 5.63. CO conversion values for CA, EMA800 and EMA materials were 70%, 47% and 33.4%, respectively. It was seen that the commercial alumina catalyst showed the highest CO conversion since it is already used in the industry for methanol dehydration. EMA800 material showed higher CO conversion compared to the EMA catalyst.
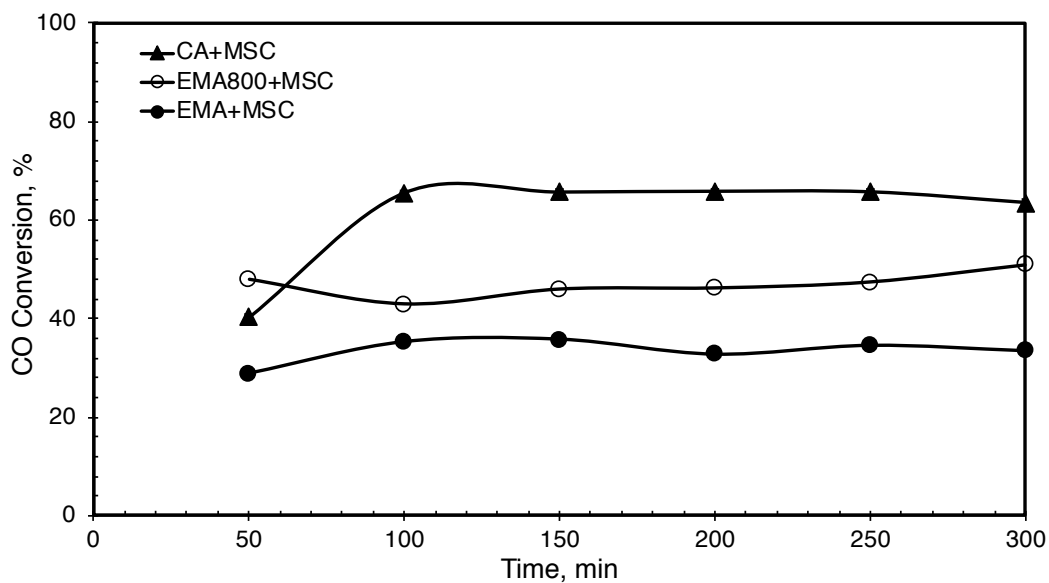
Figure 5.63. Effect of type of alumina on CO conversion (P: 50 bar, T: 275°C, H₂/CO= 1/1, GHSV: 5000 ml/h.gcat, Catalyst: alumina support + MSC (1/1 by wt.))

Comparative results of the catalysts are given in Figure 5.64. CO conversions in the descending order were found to be CA, EMA800 and EMA. Despite the highest CO conversion value was obtained from the EMA800 catalyst among the synthesized alumina materials, EMA material gave the highest DME selectivity. Both CA and EMA materials showed similar DME selectivity. However, the WGS reaction was the main side reaction in all three cases. Results also showed that EMA800 catalyst enhanced methanation reaction more than EMA and CA catalysts. These differences might be coming from their structural properties. XRD pattern revealed that EMA800 and EMA catalyst had different crystal structure. Both CA and EMA800 catalysts were in γ-alumina phase, however, EMA800 catalyst had lower DME selectivity than EMA catalyst, which was in amorphous structure. Furthermore, the EMA800 catalyst had the smallest pore size among the three alumina catalysts. This might result a higher pore diffusion resistance during the methanol dehydration, since DME is a larger molecule compared to H_2, CO, CO_2 and methane.

123
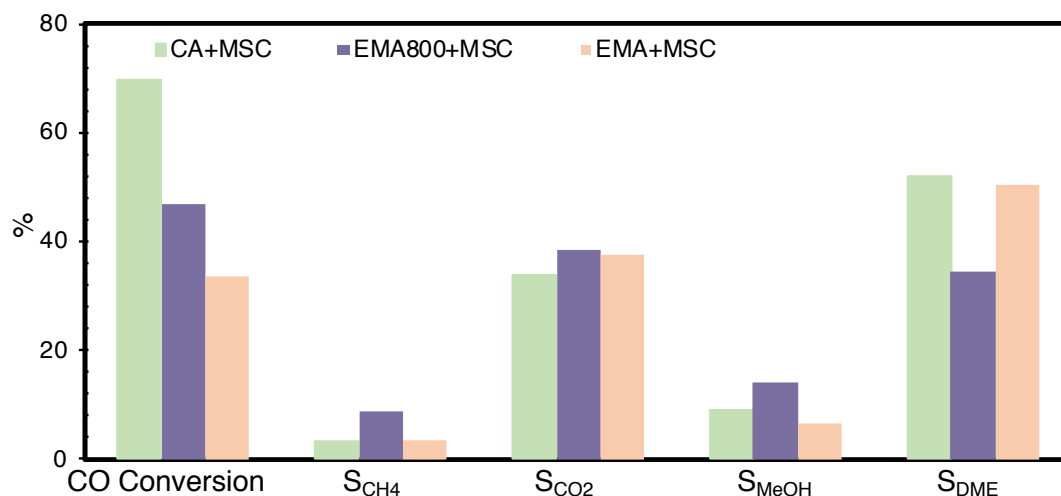
Figure 5.64. Effect of different mesoporous alumina catalysts on average CO conversion and product selectivities (P: 50 bar, T: 275°C, H_2/CO= 1/1, GHSV: 5000 ml/h.gcat, Catalyst: alumina support + MSC (1/1 by wt.))

5.2.8. Effect of TPA Loading into EMA Support on DME Production

TPA was loaded with different amounts (5, 10 and 25 wt. %) into EMA support using two different methods. These catalysts were physically mixed with MSC in the performance tests. Effect of TPA amount on CO conversion and product selectivites was investigated.

5.2.8.1. Impregnation Method Results

Three different TPA amounts were impregnated onto EMA catalyst. Figure 5.65 shows the average CO conversion and average products selectivites for EMA and TPA impregnated EMA catalysts. CO conversion increased with the addition of TPA in all cases except 25% TPA loaded one. TPA loading increased the methanol selectivity and decreased CH_4 and DME selectivities. Furthermore, TPA loading also decreased the CO_2 selectivity, which is an advantageous property for DME selectivity. This result showed that TPA loading hinders the WGS reaction compared to EMA catalyst. 10% TPA impregnated catalyst had both the highest CO conversion and DME

selectivity due to its highest acidity and surface area, among the other TPA impregnated catalysts. 25% TPA impregnated catalyst had the lowest DME selectivity and the highest methanol selectivity among three TPA impregnated catalysts due to its lowest surface area and acid capacity. However, EMA catalyst had the highest DME selectivity compared to TPA impregnated catalyst. BJH desorption pore size distribution showed that TPA loading decreased the pore size and increased the microporosity of the 10TPA@EMA catalyst. This might result a higher pore diffusion resistance during the methanol dehydration compared to EMA catalyst.
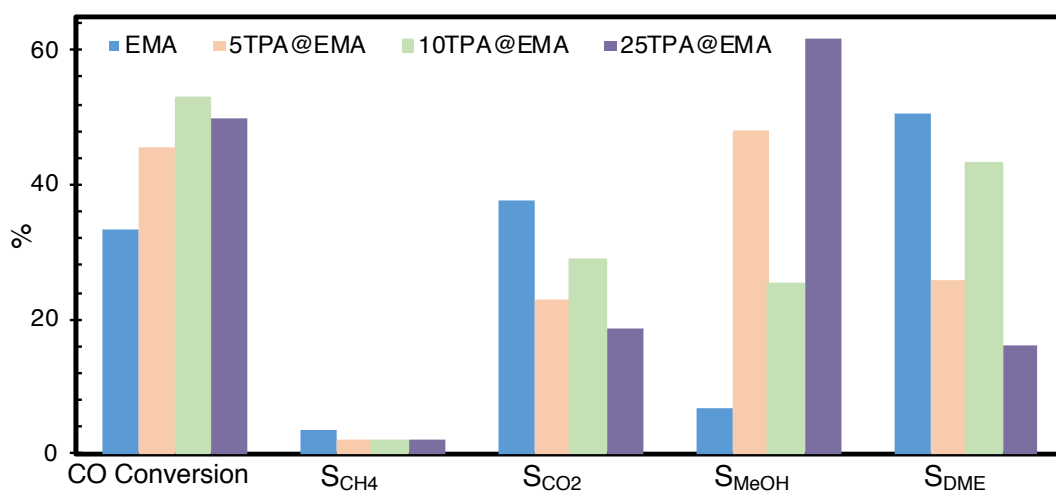
Figure 5.65. Effect of TPA amount impregnated to EMA support on CO conversion and product selectivites (P: 50 bar, T: 275°C, $H_2/CO= 1/1$, GHSV: 5000 ml/h.gcat, Catalyst: each was physically mixed with MSC)

5.2.8.2. One-pot Method Results

Three different EMA catalysts were synthesized with loading different TPA amounts via one-pot method and tested under 275°C, 50 bar and 5000 ml/h.gcat conditions. Figure 5.66 shows the average CO conversion and product selectivites for all types of one-pot synthesized catalysts mixed with the MSC catalyst. 10% TPA loaded catalyst had the lowest CO conversion and the highest DME selectivity among the others. The

25TPA/EMA catalyst had the lowest DME selectivity and the highest CO conversion and methanol selectivity. This might be due to its low surface area compared to the 10TPA/EMA catalyst.
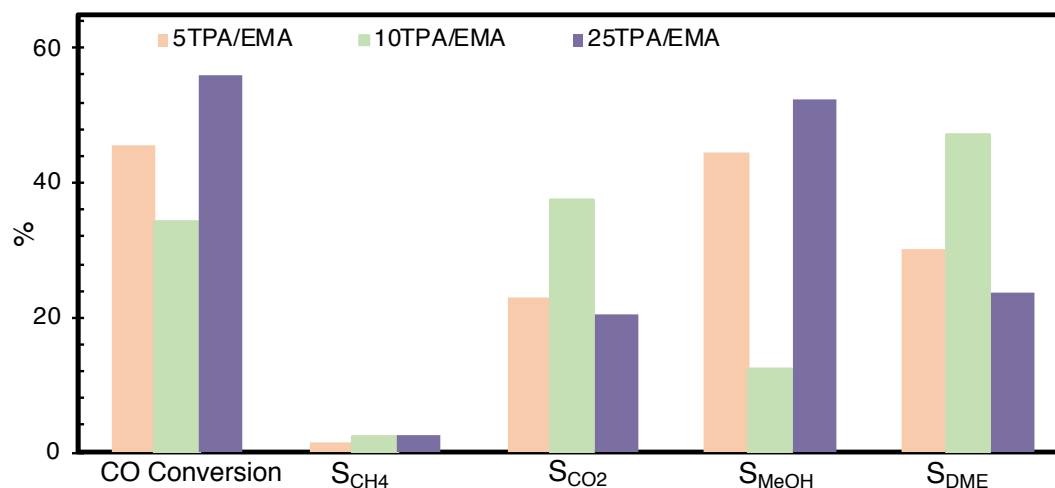
Figure 5.66. Effect of TPA amount loaded with one-pot method into EMA support on CO conversion and product selectivites (P: 50 bar, T: 275°C, $H_2/CO= 1/1$, GHSV: 5000 ml/h.gcat, Catalyst: each was physically mixed with MSC)

Figure 5.67 presents CO conversion comparison between impregnation and one-pot TPA loading methods. 5% TPA loading into EMA support gave the same CO conversion, regardless of the loading method. It can also be seen that, 10% TPA loaded catalyst gave the highest CO conversion among the catalysts synthesized using the impregnation method, whereas 25% TPA loaded catalyst gave the highest CO conversion among the catalysts synthesized using the one-pot method. However, both conversion values for 10TPA@EMA and 25TPA/EMA catalysts were close to each other.

126
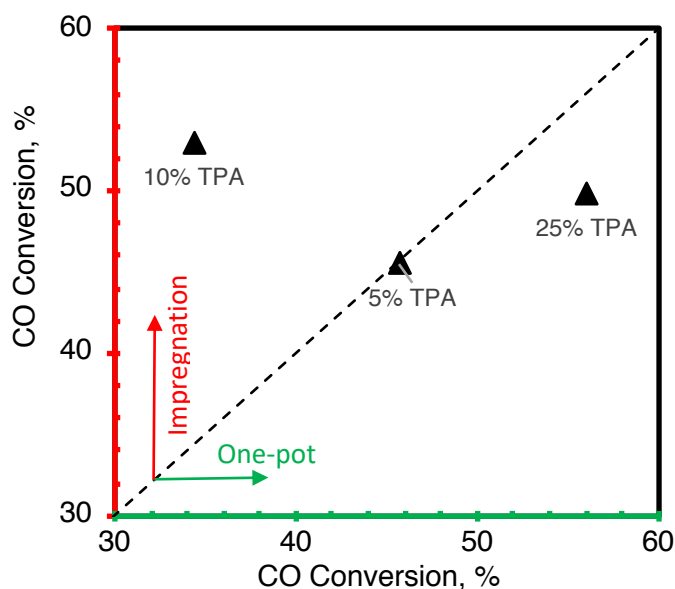
Figure 5.67. Effect of TPA loading method into support on CO conversion (P: 50 bar, T: 275°C, H$_2$/CO= 1/1, GHSV: 5000 ml/h.gcat, Catalyst: each was physically mixed with MSC)

In Figure 5.68, DME selectivity did not changed significantly by TPA loading method. DME selectivity of 10% TPA loaded both EMA catalysts were significantly higher than the other TPA loaded ones. Furthermore, one-pot synthesized catalysts gave higher DME selectivity in all cases compared to impregnation method, regardless of the loading amount. Hence, a significant result can be concluded that the optimum TPA loading amount is 10% in both loading methods. This result is in good agreement with the physical properties of 10% TPA loaded catalysts since both 10% TPA loaded catalysts were the superior among the others in terms of surface area and pore size. 10TPA@EMA had the highest acidity, whereas 10TPA/EMA catalyst had similar acidity with 25TPA/EMA catalyst. But the surface area values of the 10% TPA loaded catalysts were higher than that of the 25TPA/EMA catalyst.
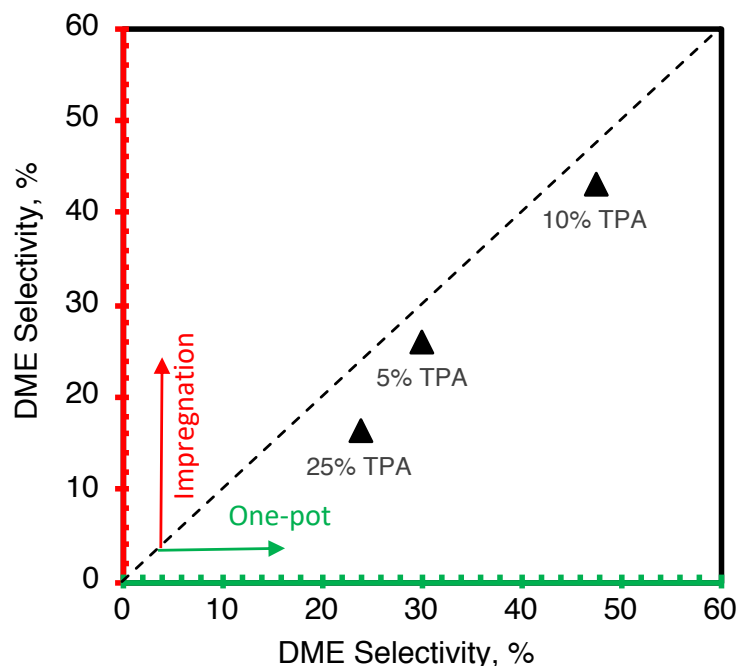
Figure 5.68. Effect of TPA loading method into support on DME selectivity (P: 50 bar, T: 275°C, H2/CO= 1/1, GHSV: 5000 ml/h.gcat, Catalyst: each was physically mixed with MSC)

In both method, 25% TPA loaded EMA catalysts had the lowest performance in terms of DME selectivity, whereas CO conversion values were considerably high. These results may indicate the lack of accessibility to the alumina surface by the reactants due to the presence of excess TPA in the structure. Hence, both alumina support and TPA may play a significant role in both CO conversion and methanol dehydration. Investigating the optimum TPA loading amount into the support is important in that manner.

5.2.9. Effect of Support on Bifunctional DME Synthesis Catalysts

Two different bifunctional DME synthesis catalysts were synthesized during this study. TPA and Cu-Zn were loaded into both EMA and CMK-3 supports, separately

and then these catalysts were tested to produce DME from syngas. Figure 5.69-Figure 5.70 show the CO conversion and product selectivites with respect to reaction time.

Interestingly, exactly the same CO conversion values were obtained for the TPA@Cu-Zn@EMA and TPA@Cu-Zn@CMK-3 catalysts. However, DME selectivity of TPA@Cu-Zn@CMK-3 catalyst was significantly higher than TPA@Cu-Zn@EMA catalyst (Figure 5.70).
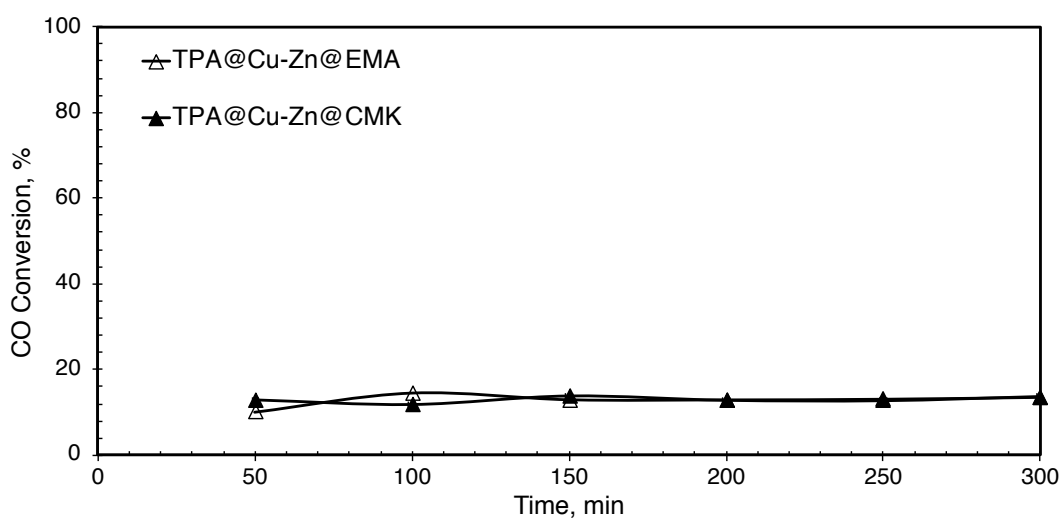
Figure 5.69. CO conversion in the presence of bifunctional DME synthesis catalysts (P: 50 bar, T: 275°C, $H_2/CO= 1/1$, GHSV: 5000 ml/h.gcat)

When the physical properties were compared between the two catalysts, TPA@Cu-Zn@EMA catalyst had higher total acidity. However, the TPD analysis showed that the TPA@Cu-Zn@CMK-3 catalyst had the zeroth order desorption curve, which means desorption of molecules from acid sites are independent from the coverage and depends on the temperature only.

Moreover, one should noticed that alumina support also contains acid sites. Average pore sizes of TPA@Cu-Zn@EMA was also found to be 8.5 nm. However, the TPA@Cu-Zn@CMK-3 had two different average pore diameters (3.9 nm and 38.5

nm). Broad pore size distribution of the TPA@Cu-Zn@CMK-3 catalyst from mesoporous region to macroporous region in the pore size distribution and its twice surface area of TPA@Cu-Zn@EMA may have also played a significant role in the single-step DME synthesis over the TPA@Cu-Zn@CMK-3 catalyst.

The TPA@Cu-Zn@CMK-3 catalyst might have a lower pore diffusion resistance for the methanol dehydration considering the higher surface area and pore size distribution and the zeroth order desorption mechanism properties of the TPA@Cu-Zn@CMK-3 catalyst may lead a lower pore diffusion resistance for the methanol dehydration.

Formic acid and ethanol formations were observed slightly high for both catalysts. 1.6% formic acid selectivity and 4.7% ethanol selectivity were obtained for the TPA@Cu-Zn@EMA catalyst, whereas 2.1% formic acid selectivity and 4.4% ethanol selectivity were observed for the TPA@Cu-Zn@CMK-3 catalyst. Among the physically mixed catalysts, these two side products and high CH_4 selectivity were only observed at 350°C over CA+MSC catalyst mixture,. Moreover, significantly higher CO_2 selectivity for both catalysts revealed that in addition to methanol dehydration reaction, R4, R7, R8, and R12 reactions were also mainly taking place in the reactor.

$$CO + H_2O \leftrightarrow CO_2 + H_2 \tag{R4}$$

$$CO_2 + H_2 \leftrightarrow HCOOH \tag{R7}$$

$$2CO + 4H_2 \leftrightarrow C_2H_5OH + H_2O \tag{R8}$$

$$CO + 3H_2 \leftrightarrow CH_4 + H_2O \tag{R12}$$

These four reactions were also mainly taking place at 350°C in the presence of CA and MSC catalyst mixture. This result might be the indication of formation of hot spots and nonuniform temperature distribution over the catalyst bed. Low surface area values and high microporosity properties of bifunctional catalysts might be the cause of the hot spot formation.
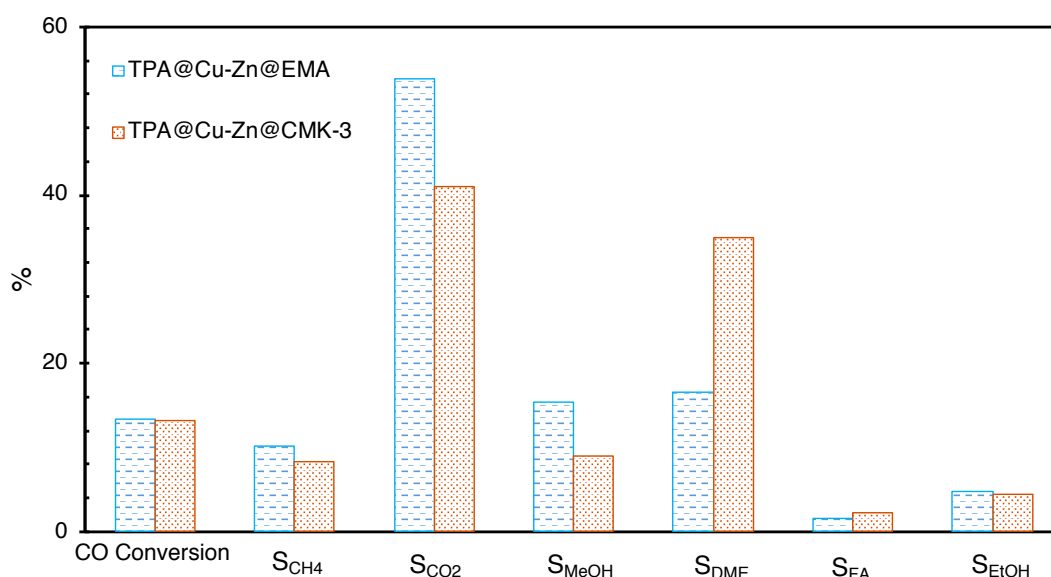
Figure 5.70. Average CO conversion and average product selectivities in the presence of bifunctional DME synthesis catalysts (P: 50 bar, T: 275°C, $H_2/CO= 1/1$, GHSV: 5000 ml/h.gcat)

The performance test of the TPA@Cu-Zn@CMK-3 catalyst was conducted using CO_2 containing feed ($CO_2/CO/H_2 = 1/1/2$) due its superior properties and higher DME selectivity. Total conversion and product selectivites and comparison of this bifunctional catalyst along with results of the CA+MSC catalyst mixture are given in Figure 5.71Figure 5.72.

Total conversion was 5% for the TPA@Cu-Zn@CMK-3 catalyst, whereas 14.7% total conversion was obtained in the presence of CA+MSC catalyst mixture. 78.5% and 51.2% DME selectivities were obtained for CA+MSC catalyst mixture and the TPA@Cu-Zn@CMK-3 catalysts, respectively. The CA+MSC catalyst mixture had higher methanol selectivity, whereas TPA@Cu-Zn@CMK-3 had significantly higher methane selectivity. However, one should notice that the TPA@Cu-Zn@CMK-3 catalyst had very low surface area for the same catalyst amount compared to CA+MSC mixture. Additionally, both lower methanol and DME selectivity of TPA@Cu-Zn@CMK-3 may be the indication of the low methanol synthesis activity of the

catalyst, whereas high DME and methanol selectivity values of CA+MSC mixture might be the indication of insufficient methanol dehydration activity.

Formic acid and ethanol selectivities of the TPA@Cu-Zn@CMK-3 catalyst were 9.5% and 7.2%, respectively. However, CA+MSC showed trace amount of formic acid and ethanol. Similar to CO_2 free performance test of the TPA@Cu-Zn@CMK-3 catalyst, high methane, ethanol and formic acid production might be the indication of hot spots on the catalyst bed.
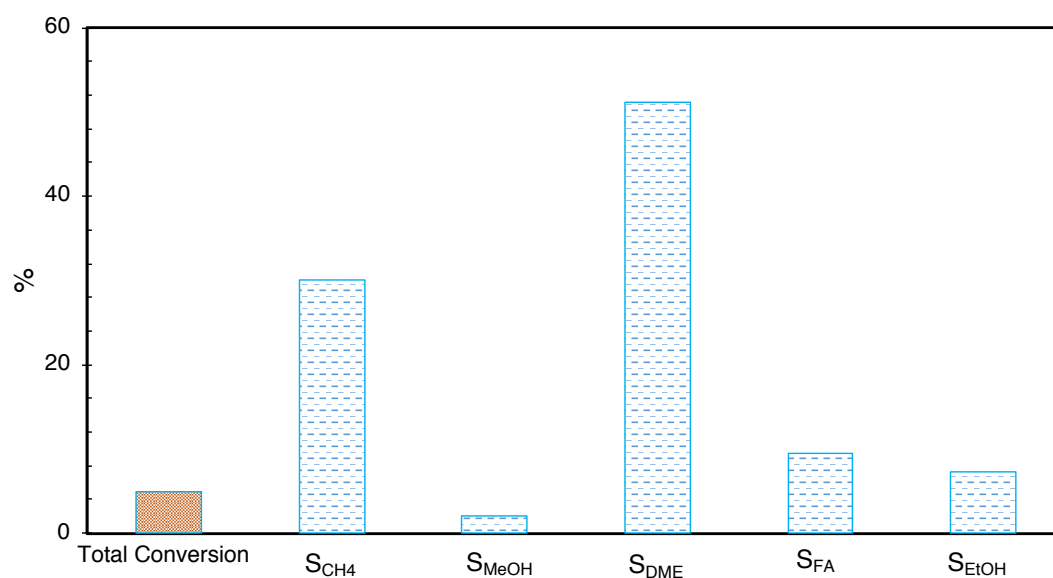
Figure 5.71. Total conversion and product selectivities of bifunctional TPA@Cu-Zn@CMK-3 catalyst (P: 50 bar, T: 275°C, $CO_2/CO/H_2$ = 1/1/2, GHSV: 5000 ml/h.gcat)
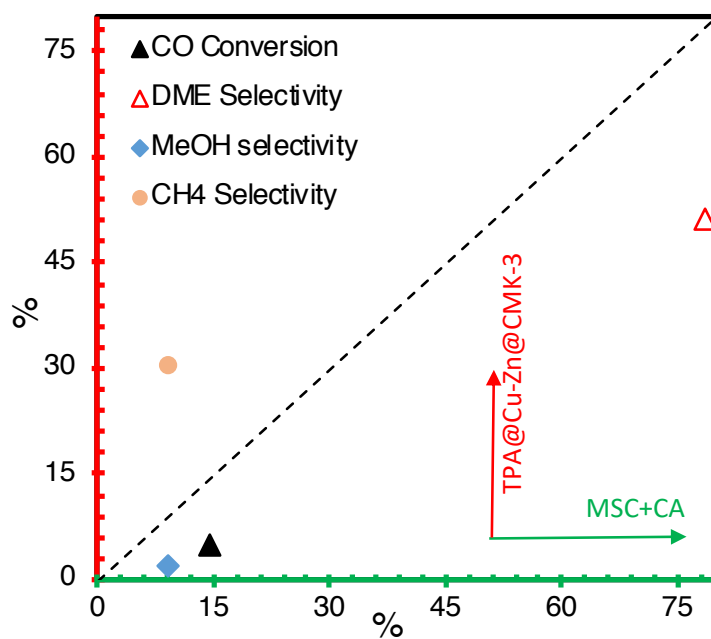
Figure 5.72. Comparison of bifunctional and physically mixed catalysts (P: 50 bar, T: 275°C, $CO_2/CO/H_2 = 1/1/2$, GHSV: 5000 ml/h.gcat)

CHAPTER 6

CONCLUSIONS AND RECOMMENDATIONS

- EMA and CMK-3 support materials were synthesized with Type IV mesoporous structure. One-pot synthesis method was superior than impregnation method in terms of TPA dispersion and physical properties considering NH_3-TPD, XRD, nitrogen physisorption and SEM-EDX results.

- Thermodynamic equilibrium studies were conducted at different pressure and temperatures. Pressure of 50 bar and $CO:H_2$ ratio of 1:1 were selected based on the equilibrium studies. Optimum operating temperature of 275°C was confirmed with the experimental study.

- Non-reduced commercial methanol synthesis catalyst (MSC) showed very low activity compared to reduced ones. Regardless of reduction state of the catalyst, the product selectivities of the reduced and non-reduced catalysts were similar. Results revealed that non-reduced MSC had limited number of active sites for methanol formation and it did not reduced during the reaction despite the presence of hydrogen. Therefore, reduction procedure was required before each experiment.

- Commercial methanol synthesis (MSC) and Commercial alumina (CA) catalyst mixture was found the most catalytically active couple with the highest CO conversion and DME selectivity. However, it was seen that MSC and EMA catalyst mixture was gave similar DME selectivity compared to CA and MSC mixture without any TPA loading.

- TPA loading into the support increased CO conversion in all cases. Furthermore, optimum TPA loading amount was determined as 10 wt. %, regardless of loading method. Both 10% TPA loaded catalysts mixed with MSC gave the highest DME selectivities among the others. 10TPA@EMA and MSC catalyst mixture was the most catalytically active catalyst mixture among the synthesized catalysts due its highest CO conversion and high DME selectivity.

- TPA and Cu-Zn containing bifunctional DME synthesis catalysts were synthesized using two different supports, namely; mesoporous carbon (CMK-3) and EMA. Both catalysts had higher total acidity values compared to the EMA support. Both catalysts gave the same CO conversion, however, TPA@Cu-Zn@CMK-3 catalyst showed significantly higher DME selectivity.

- Negative effect of CO_2 content in the feed was clearly seen in both thermodynamic and experimental studies.

- In this study TEM-EDX imaging could be conducted to observe the TPA location on the support material. This analysis may also help to identify the dispersion and crystal structure of TPA.

- Loading of TPA and Cu-Zr metals into EMA and CMK-3 supports is recommended to be able to synthesize methanol from CO_2 containing feed. Only H_2/CO_2 feed mixture could also be used to test these catalysts to observe the activity of the catalysts in the presence of CO_2.

- Effect of reaction temperature on methanol synthesis could be carried out to be able to compare the effect of temperature on both methanol synthesis and dehydration.

- Development of synthesis of EMA support and the detailed investigation of differences between EMA and CA catalysts are recommended.

- A narrow range of TPA loading might be carried out to find out more precise optimum TPA loading amount into support material. Furthermore, combination of both TPA and/or Cu-Zn loading into CA catalyst is recommended due to its high methanol dehydration activity.

- Investigation of the optimum TPA and Cu-Zn loading into the support materials is recommended. SEM or TEM mapping could be conducted to observe the metal dispersion over these supports. Furthermore, due to sintering of copper and deuteration of TPA at higher than 300°C, removal of impurities and calcination may not be completed at this temperature. Therefore, applying supercritical CO_2 extraction instead of calcination of catalysts is recommended.

REFERENCES

Adachi, Y., Komoto, M., Watanabe, I., Ohno, Y., & Fujimoto, K. (2000a). Effective utilisation of remote coal through dimethyl ether synthesis. *Fuel*, *79*, 229–234.

Adachi, Y., Komoto, M., Watanabe, I., Ohno, Y., & Fujimoto, K. (2000b). Effective utilization of remote coal through dimethyl ether synthesis, *79*, 229–234.

Azizi, Z., Rezaeimanesh, M., Tohidian, T., & Rahimpour, M. R. (2014). Dimethyl ether: A review of technologies and production challenges. *Chemical Engineering and Processing: Process Intensification*, *82*, 150–172.

Azizi, Z., Rezaeimanesh, M., Tohidian, T., & Reza, M. (2014). Chemical Engineering and Processing : Process Intensification Dimethyl ether : A review of technologies and production challenges. *Chemical Engineering & Processing: Process Intensification*, *82*, 150–172.

Barrera, D., Dávila, M., Cornette, V., De Oliveira, J. C. A., López, R. H., & Sapag, K. (2013). Pore size distribution of ordered nanostructured carbon CMK-3 by means of experimental techniques and Monte Carlo simulations. *Microporous and Mesoporous Materials*, *180*, 71–78.

Cava, S., Tebcherani, S. M., Souza, I. a., Pianaro, S. a., Paskocimas, C. a., Longo, E., & Varela, J. a. (2007). Structural characterization of phase transition of Al2O3 nanopowders obtained by polymeric precursor method. *Materials Chemistry and Physics*, *103*(2–3), 394–399.

Celik, G., Arinan, A., Bayat, A., Ozbelge, H. O., Dogu, T., & Varisli, D. (2013). Performance of silicotungstic acid incorporated mesoporous catalyst in direct synthesis of dimethyl ether from syngas in the presence and absence of CO2. *Topics in Catalysis*, *56*(18–20), 1764–1774.

Chorkendorff, I., & Niemantsverdriet, J. W. (2003). *Concepts of Modern Catalysis and Kinetics*. *Concepts of Modern Catalysis and Kinetics*. Weinheim, FRG: Wiley.

Ciftci, A., Sezgi, N. A., & Dogu, T. (2010). Nafion-Incorporated Silicate Structured Nanocomposite Mesoporous Catalysts for Dimethyl Ether Synthesis. *Ind. Eng. Chem. Res.*, *49*, 6753–6762.

Ciftci, A., Varisli, D., Cem Tokay, K., Asli Sezgi, N., & Dogu, T. (2012). Dimethyl

ether, diethyl ether & ethylene from alcohols over tungstophosphoric acid based mesoporous catalysts. *Chemical Engineering Journal*, *207–208*, 85–93.

de Jong, K. P. (Ed.). (2009). *Synthesis of Solid Catalysts*. Wiley.

Fadoni, M., & Lucarelli, L. (1999). Temperature programmed desorption, reduction, oxidation and flow chemisorption for the characterisation of heterogeneous catalysts. Theoretical aspects, instrumentation and applications (pp. 177–225).

Fleisch, T. H., Basu, A., Gradassi, M. J., & Masin, J. G. (1997). Natural Gas Conversion IV. *Studies in Surface Science and Catalysis*, *107*, 117–125.

Gonçalves, A. A. S., Faustino, P. B., Assaf, J. M., & Jaroniec, M. (2017). One-Pot Synthesis of Mesoporous Ni-Ti-Al Ternary Oxides: Highly Active and Selective Catalysts for Steam Reforming of Ethanol. *ACS Applied Materials and Interfaces*, *9*(7), 6079–6092.

He, J., Ma, K., Jin, J., Dong, Z., Wang, J., & Li, R. (2009). Preparation and characterization of octyl-modified ordered mesoporous carbon CMK-3 for phenol adsorption. *Microporous and Mesoporous Materials*, *121*(1–3), 173–177.

Iranshahi, D., Saeedi, R., & Azizi, K. (2017). Maximization of dimethyl ether production from synthesis gas by obtaining optimum temperature profile and water removal. *Fuel*, *190*, 386–395.

Jiang, S. P. (2014). Functionalized mesoporous structured inorganic materials as high temperature proton exchange membranes for fuel cells. *Journal of Materials Chemistry A*, *2*(21), 7637–7655.

Kasatkin, I., Kurr, P., Kniep, B., Trunschke, A., & Schlögl, R. (2007). Role of lattice strain and defects in copper particles on the activity of $Cu/ZnO/Al_2O_3$ catalysts for methanol synthesis. *Angewandte Chemie - International Edition*, *46*(38), 7324–7327.

Khoshbin, R., Haghighi, M., & Margan, P. (2016). Combustion dispersion of CuO-$ZnO-Al_2O_3$ nanocatalyst over HZSM-5 used in DME production as a green fuel: Effect of citric acid to nitrate ratio on catalyst properties and performance. *Energy Conversion and Management*, *120*, 1–12.

Kim, J. Y., Rodriguez, J. A., Hanson, J. C., Frenkel, A. I., & Lee, P. L. (2003). Reduction of CuO and Cu_2O with H_2: H embedding and kinetic effects in the formation of suboxides. *Journal of the American Chemical Society*, *125*(35), 10684–10692.

Kühl, S., Tarasov, A., Zander, S., Kasatkin, I., & Behrens, M. (2014). Cu-based catalyst resulting from a Cu,Zn,Al hydrotalcite-like compound: A microstructural, thermoanalytical, and in situ XAS study. *Chemistry - A European Journal*, *20*(13), 3782–3792.

Llanos, A., Melo, L., Avendaño, F., Montes, A., & Brito, J. L. (2008). Synthesis and characterization of HPW/MCM-41 (Si) and HPW/MCM-41 (Si/Al) catalysts: Activity for toluene alkylation with 1-dodecene. *Catalysis Today*, *133–135*(1–4), 20–27.

Lu, W.-Z., Teng, L.-H., & Xiao, W.-D. (2003). Theoretical Analysis of Fluidized-Bed Reactor for Dimethyl Ether Synthesis from Syngas. *International Journal of Chemical Reactor Engineering*, *1*.

Lu, W. Z., Teng, L. H., & Xiao, W. De. (2004). Simulation and experiment study of dimethyl ether synthesis from syngas in a fluidized-bed reactor. *Chemical Engineering Science*, *59*(22–23), 5455–5464.

McLaughlin, J. E. (2006). Establishing Minimum Pressurization Temperature (MPT) for Heavy Wall Reactors in Hydroprocessing Units. *Volume 7: Operations, Applications, and Components*, *2006*, 239–247.

Michorczyk, P., Kuśtrowski, P., Niebrzydowska, P., & Wach, A. (2012). Catalytic performance of sucrose-derived CMK-3 in oxidative dehydrogenation of propane to propene. *Applied Catalysis A: General*, *445–446*, 321–328.

Moradi, G. R., Ahmadpour, J., Yaripour, F., & Wang, J. (2011). Equilibrium calculations for direct synthesis of dimethyl ether from syngas. *The Canadian Journal of Chemical Engineering*, *89*(1), 108–115.

Ng, K. L. ., Chadwick, D. ., & Toseland, B. A. . (1999). Kinetics and modelling of dimethyl ether synthesis from synthesis gas. *Chemical Engineering Science*, *54*(15–16), 3587–3592.

Niemantsverdriet, J. W. (2007). *Spectroscopy in Catalysis: An Introduction: Third Edition. Spectroscopy in Catalysis: An Introduction: Third Edition* (Vol. 91).

Ogawa, T., Inoue, N., Shikada, T., Inokoshi, O., & Ohno, Y. (2004). Direct Dimethyl Ether (DME) synthesis from natural gas, *147*, 379–384.

Ozbay, N. (2008). *Biyodizel Yan Ürünü Gliserinin Eterifikasyonu Iile Yüksek Kalitede Yeni Yakit Formülasyonu*. PhD Thesis, Gazi University.

Peng, X. D., Wang, A. W., Toseland, B. A., & Tijm, P. J. A. (1999). Single-Step Syngas-to-Dimethyl Ether Processes for Optimal Productivity, Minimal Emissions, and Natural Gas-Derived Syngas. *Ind. Eng. Chem. Res.*, *38*(11), 4381–4388.

Richardson, J. T. (1989). *Principles of Catalyst Development. Advanced Materials* (Vol. 3). Boston, MA: Springer US.

Rodriguez, J. A., Kim, J. Y., Hanson, J. C., Pérez, M., & Frenkel, A. I. (2003). Reduction of CuO in H2: In situ time-resolved XRD studies. *Catalysis Letters*, *85*(3–4), 247–254.

San Pio, M. A., Gallucci, F., Roghair, I., & van Sint Annaland, M. (2017). Gas-solids kinetics of CuO/Al2O3 as an oxygen carrier for high-pressure chemical looping processes: The influence of the total pressure. *International Journal of Hydrogen Energy*, *42*(17),

Srinivas, M., Raveendra, G., Parameswaram, G., Prasad, P. S. S., & Lingaiah, N. (2016). Cesium exchanged tungstophosphoric acid supported on tin oxide: An efficient solid acid catalyst for etherification of glycerol with tert-butanol to synthesize biofuel additives. *Journal of Molecular Catalysis A: Chemical*, *413*, 7–14.

Takashi Ogawa, Norio Inoue, Tutomu Shikada, Osamu Inokoshi, Y. O. (2004). Direct Dimethyl Ether (DME) synthesis from natural gas. *Studies in Surface Science and Catalysis*, *147*, 379–384.

Tavakoli, A. H., Maram, P. S., Widgeon, S. J., Rufner, J., Van Benthem, K., Ushakov, S., Navrotsky, A. (2013). Amorphous alumina nanoparticles: Structure, surface energy, and thermodynamic phase stability. *Journal of Physical Chemistry C*, *117*(33), 17123–17130.

Timofeeva, M. (2003). Acid catalysis by heteropoly acids. *Applied Catalysis A: General*, *256*(1–2), 19–35.

Tokay, K. C., Dogu, T., & Dogu, G. (2012). Dimethyl ether synthesis over alumina based catalysts. *Chemical Engineering Journal*, *184*, 278–285.

Trunschke, A. (2013). *Modern Methods in Hetergeneous Catalysis Research - Surface area and pore size determination* (Vol. 1).

Varişli, D., Tokay, K. C., Çiftçi, A., Doğu, T., & Doğu, G. (2009). Methanol dehydration reaction to produce clean diesel alternative dimethylether over

mesoporous aluminosilicate-based catalysts. *Turkish Journal of Chemistry*, *33*(3), 355–366.

Varışlı, D. (2007). *Kinetic Studies For Dimethyl Ether And Diethyl Ether Production. PhD Thesis*. METU.

Wu, W., Wan, Z., Chen, W., Zhu, M., & Zhang, D. (2015). Synthesis of mesoporous alumina with tunable structural properties. *Microporous and Mesoporous Materials*, *217*, 12–20.

Xing, R., Liu, Y., Wang, Y., Chen, L., Wu, H., Jiang, Y., … Wu, P. (2007). Active solid acid catalysts prepared by sulfonation of carbonization-controlled mesoporous carbon materials. *Microporous and Mesoporous Materials*, *105*(1–2), 41–48.

Yates, J. G., & Lettieri, P. (2016). *Fluidized-Bed Reactors: Processes and Operating Conditions* (Vol. 26).

Yuan, Q., Yin, A.-X., Luo, C., Sun, L.-D., Zhang, Y.-W., Duan, W.-T., … Yan, C.-H. (2008). Facile Synthesis for Ordered Mesoporous γ-Aluminas with High Thermal Stability. *Journal of the American Chemical Society*, *130*(11), 3465–3472.

Zhang, L., Zhang, H., Ying, W., & Fang, D. (2011). Intrinsic Kinetics of Methanol Dehydration over Al2O3 Catalyst, 1538–1543.

Zhao, D. (1998). Triblock Copolymer Syntheses of Mesoporous Silica with Periodic 50 to 300 Angstrom Pores. *Science*, *279*(5350), 548–552.

APPENDICES

A. Thermodynamic Equilibrium Calculations

Thermodynamic equilibrium conversion was calculated as follows:

For the calculation of Gibbs free energy of the reaction, Gibbs free energy of formation values of reactants and products should be evaluated. Methanol synthesis reaction (R1) was taken as the model for the sample calculation.

$$CO + 2H_2 \leftrightarrow CH_3OH \qquad\qquad \Delta Hrxn = -90 \text{ kJ/mol} \qquad\qquad (R1)$$

$$\Delta G°_{rxn,298} = \Delta G°_{f,CH3OH} - (\Delta G°_{f,CO} + 2*\Delta G°_{f,H2}) \qquad\qquad (1)$$

Equilibrium constant at reference temperature and equilibrium constant of the reaction at any temperature can be calculated using following equations.

$$\Delta G°_{rxn,298} = -RT \ln K_{298} \qquad\qquad (2)$$

$$K = K°_{298} \exp \left(\int_{298}^{T} \frac{\Delta H°_{rxn}}{R\,T^2} dT \right) \qquad\qquad (3)$$

Equation of states were used at high pressure systems for more realistic results instead of ideal gas law. The Soave-Redlich-Kwong EOS was used for the fugacity calculations.

$$P = \frac{R\,T}{(V-b)} - \frac{a}{V\,(V+b)} \qquad\qquad (4)$$

where,

$$b = 0.08664\, \frac{R\,T_C}{P_C}$$

$$a = 0.42748\, \frac{(R\,T_C)^2}{P_C} \left(1 + m \left(1 - \sqrt{T_C} \right) \right)^2$$

$$T_r = \frac{T}{T_C} \quad \text{and} \quad m = 0.480 + 1.574\omega - 0.176\,\omega^2$$

In order to determine the thermodynamic equilibrium constant, the following equation was used.

$$K = K_P * K_\phi \tag{5}$$

where,

$$K_\phi = \frac{\phi_{CH_3OH}}{\phi_{CO} * \phi_{H_2}{}^2}$$

$$K_P = \frac{P_{CH_3OH}}{P_{CO} * P_{H_2}{}^2} = \frac{y_{CH_3OH}}{y_{CO} * y_{H_2}{}^2 * P_T{}^2}$$

Mol fractions of each component are given in Table A.1 based on 100 mol basis for the case of $CO:H_2$ ratio was equal to 1:1.

Table A.1. *Calculation for equilibrium mol fraction for the methanol synthesis reaction*

Species	n_i (mol)	n_t (mol)	n_{eqm} (mol)	y_i
CO	50	50-50x	$50-50x_{eq}$	$[50-50x_{eq})]/[100-100x_{eq}]$
H₂	50	50-100x	$50-100x_{eq}$	$[50-100x_{eq}]/[100-100x_{eq}]$
CH₃OH	-	50x	$50x_{eq}$	$[50x_{eq}]/[100-100x_{eq}]$
Total	*100*	*100-100x*	*100-100x_{eq}*	1

Fugacity coefficients of the each species for the mixture should be calculated.

Using the SRK EOS results the following equation for the fugacity coefficient of component *i* in a mixture:

$$\ln \widehat{\Phi}^V = \frac{B_i}{B_{mix}}(Z^V_{mix} - 1) - \ln(Z^V_{mix} - B_{mix})$$

$$- \frac{A_{mix}}{B_{mix}} \ln(\frac{2\sum_{j=1}^{k} y_j A_{ij}}{A_{mix}} + \frac{B_i}{B_{mix}})\ln(1 + \frac{B_{mix}}{Z^V_{mix}}) \tag{6}$$

where,

$$Amix = \sum_{i}^{k} \sum_{j}^{k} x_i x_j A_{ij}$$

and α_i is as,

$$Bmix = \sum_{i}^{k} x_i B_i$$

A_{ii}, A_{ij} and B_i are represented as for SRK EOS,

$$A_{ii} = 0.42748 \left(\frac{P_r}{T_r^2}\right)_i \alpha_i$$

$$A_{ij} = \left(1 - k_{ij}\right)\sqrt{A_{ii}A_{jj}}$$

$$B_i = 0.08664 \left(\frac{P_r}{T_r}\right)$$

and α_i is follows,

$$\alpha_i = \left[1 + (0.480 + 1.574\omega_i - 0.176\omega_i{}^2)\left(1 - \sqrt{T_{r_i}}\right)\right]^2$$

k_{ij} is the adjustable binary interaction parameter and it is symmetric.

On the other hand, compressibility factor for mixtures are calculated as;

$$Z^3_{mix} + pZ^2_{mix} + qZ_{mix} + r = 0$$

For the SRK EOS, p, q and r parameters are;

$$p = -1; \qquad q = A_{mix} - B_{mix} - B_{mix}^2; \qquad r = -A_{mix}B_{mix}$$

The molar volume of the mixture can be calculated as;

$$\tilde{V}_{mix} = \frac{Z_{mix}^V RT}{P}$$

Final equation resulted Equation (7) and the fractional equilibrium conversion of CO for each temperature and pressure values can be evaluated from using Equation (7).

$$K = \frac{\frac{50\, x_{eq}}{100 - 100\, x_{eq}}}{\left(\frac{50 - 50\, x_{eq}}{100 - 100\, x_{eq}}\right)\left(\frac{50 - 100\, x_{eq}}{100 - 100\, x_{eq}}\right)^2} \frac{1}{P_T^2} \frac{\Phi_{CH3OH}}{\Phi_{CO}\Phi_{H2}^2} \tag{7}$$

B. Ammonia Calibration Curve

Ammonia calibration curves are presented in Figure B.1.
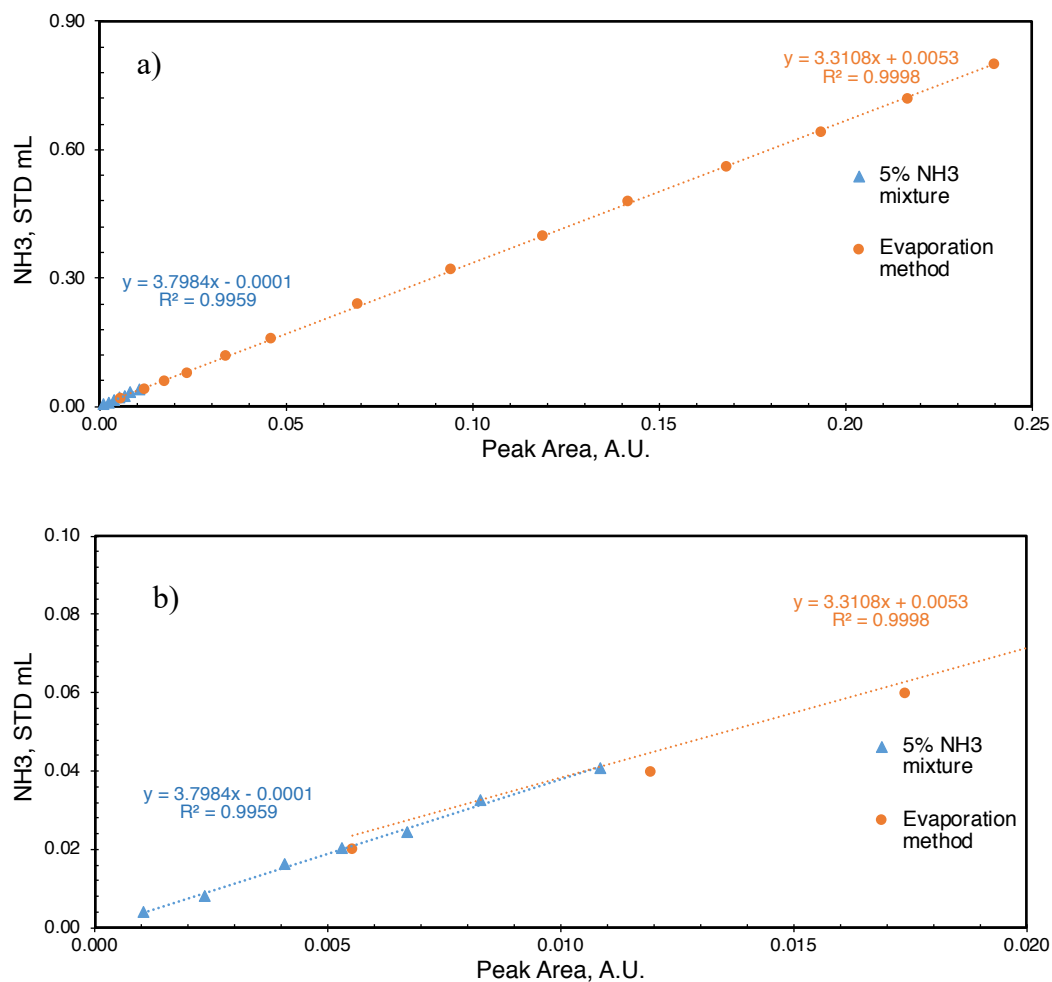
Figure B.1. a) NH_3-TPD calibration curve b) magnified version of calibration curve

C. GC Calibration

GC calibration factors calculations were conducted using the Gay-Lussac Law. At the same temperature and pressure, gas volumes are proportional to mole numbers of the gases, assuming that gases obey the ideal gas.

Calibration factor of CO (β_{CO}) was taken as 1 and calibration factor (β) for each component (i) was calculated from the formula below.

$$\frac{n_{CO}}{n_i} = \frac{A_{CO} \, x \, \beta_{CO}}{A_i \, x \, \beta_i}$$

where β_{CO} is the calibration factor of CO, n_{CO} is mole number of CO and A_{CO} is the area under the peak of CO in the GC pictogram.

D. XRD Data

XRD data of Al_2O_3, Cu, CuO, Cu_2O, Zn and ZnO, which was taken from **International Centre for Diffraction Data** (ICDD) PDF4+ 2019 database are given in Table D.1-D.6.

Table D.1. *XRD data for γ-alumina*

Compound Name: Aluminum Oxide

Chemical Formula: Al_2O_3

PDF Card No: 00-056-0457

Radiation: $CuK_{\alpha 1}$

Wavelength: 1.5405 Å

2θ (°)	d (Å)	Intensity	h	k	l
31.97229	2.7969	2	2	2	0
37.68181	2.3852	4	3	1	1
39.42608	2.2836	60	2	2	2
45.84463	1.9777	64	4	0	0
50.23088	1.8148	1	3	3	1
56.98095	1.6148	1	4	2	2
60.79077	1.5224	5	5	1	1
66.84788	1.3984	100	4	4	0
70.34492	1.3372	2	5	3	1
71.4943	1.3185	1	4	4	2
76.02449	1.2508	1	6	2	0
79.35933	1.2064	4	5	3	3
80.46382	1.1926	33	6	2	2
84.84914	1.1418	26	4	4	4
93.55049	1.0571	1	6	4	2
102.3391	0.9888	13	8	0	0
105.70076	0.9664	3	7	3	3
114.98278	0.9134	5	7	5	1
116.18162	0.9074	6	6	6	2

Table D.2. *XRD data for copper*

Compound Name: Copper					
Chemical Formula: Cu					
PDF Card No: 00-004-0836					
Radiation: $CuK_{\alpha 1}$					
Wavelength: 1.5405 Å					
2θ (°)	**d-spacing (Å)**	**Intensity (%)**	**h**	**k**	**l**
43.29658	2.088	100	1	1	1
50.433	1.808	46	2	0	0
74.13034	1.278	20	2	2	0
89.93068	1.09	17	3	1	1
95.13944	1.0436	5	2	2	2
116.91847	0.9038	3	4	0	0
136.5068	0.8293	9	3	3	1
144.71382	0.8083	8	4	2	0

Table D.3. *XRD data for copper oxide*

Compound Name: Copper Oxide
Chemical Formula: CuO
PDF Card No: 00-041-0254
Radiation: $CuK_{\alpha1}$
Wavelength: 1.5405 Å

2θ (°)	d-spacing (Å)	Intensity (%)	h	k	l
32.50826	2.752	8	1	1	0
35.43671	2.531	60	0	0	2
35.53826	2.524	100	-1	1	1
38.73043	2.323	100	1	1	1
38.93964	2.311	100	2	0	0
46.26261	1.9608	3	-1	1	2
48.7419	1.8667	25	-2	0	2
53.46489	1.7124	7	0	2	0
58.31077	1.5811	12	2	0	2
61.54679	1.5055	16	-1	1	3
65.82133	1.4177	12	0	2	2
66.27454	1.4091	14	-3	1	1
67.93191	1.3787	9	1	1	3
68.1454	1.3749	14	2	2	0
72.43349	1.3037	6	3	1	1
74.98772	1.2655	6	0	0	4
75.25973	1.2616	7	-2	2	2
80.18849	1.196	2	-2	0	4
82.37539	1.1697	4	-3	1	3
83.10272	1.1613	4	2	2	2
83.68455	1.1547	4	4	0	0
86.5668	1.1235	2	-4	0	2
89.81535	1.0911	5	-1	3	1

Table D.4. *XRD data for copper oxide*

Compound Name: Copper Oxide

Chemical Formula: Cu_2O

PDF Card No: 00-005-0667

Radiation: $CuK_{\alpha 1}$

Wavelength: 1.5405 Å

2θ (°)	d-spacing (Å)	Intensity (%)	h	k	l
29.55423	3.02	9	1	1	0
36.41832	2.465	100	1	1	1
42.29706	2.135	37	2	0	0
52.45388	1.743	1	2	1	1
61.34354	1.51	27	2	2	0
69.56926	1.3502	1	3	1	0
73.52625	1.287	17	3	1	1
77.32331	1.233	4	2	2	2
92.38032	1.0674	2	4	0	0
103.70092	0.9795	4	3	3	1
107.55821	0.9548	3	4	2	0
124.22199	0.8715	3	4	2	2
139.28376	0.8216	3	5	1	1

Table D.5. *XRD data for zinc*

Compound Name: Zinc

Chemical Formula: Zn

PDF Card No: 00-004-0831

Radiation: CuK$_{\alpha 1}$

Wavelength: 1.5405 Å

2θ (°)	d-spacing (Å)	Intensity (%)	h	k	l
36.2964	2.473	53	0	0	2
38.9923	2.308	40	1	0	0
43.23133	2.091	100	1	0	1
54.33554	1.687	28	1	0	2
70.05634	1.342	25	1	0	3
70.66048	1.332	21	1	1	0
77.02716	1.237	2	0	0	4
82.1021	1.1729	23	1	1	2
83.76462	1.1538	5	2	0	0
86.5572	1.1236	17	2	0	1
89.92018	1.0901	3	1	0	4
94.89993	1.0456	5	2	0	2
109.12851	0.9454	8	2	0	3
115.79811	0.9093	6	1	0	5
116.38495	0.9064	11	1	1	4
124.04846	0.8722	5	2	1	0
127.48673	0.8589	9	2	1	1
131.84053	0.8437	2	2	0	4
138.21107	0.8245	1	0	0	6
138.94717	0.8225	9	2	1	2

Table D.6. *XRD data for zinc oxide*

Compound Name: Zinc Oxide

Chemical Formula: ZnO

PDF Card No: 00-036-1451

Radiation: $CuK_{\alpha 1}$

Wavelength: 1.5405 Å

2θ (°)	d-spacing (Å)	Intensity (%)	h	k	l
31.76937	2.8143	57	1	0	0
34.42107	2.60332	44	0	0	2
36.2521	2.47592	100	1	0	1
47.53765	1.91114	23	1	0	2
56.60155	1.62472	32	1	1	0
62.86238	1.47712	29	1	0	3
66.37824	1.40715	4	2	0	0
67.96104	1.37818	23	1	1	2
69.09818	1.35825	11	2	0	1
72.55989	1.30174	2	0	0	4
76.95278	1.23801	4	2	0	2
81.3677	1.18162	1	1	0	4
89.60447	1.09312	7	2	0	3
92.78079	1.06384	3	2	1	0
95.30074	1.04226	6	2	1	1
98.60924	1.01595	4	1	1	4
102.94242	0.984641	2	2	1	2
104.13035	0.976632	5	1	0	5
110.38791	0.93812	3	3	0	0
116.27442	0.906943	8	2	1	3
121.56691	0.882558	4	3	0	2
133.92545	0.837033	3	2	0	5
138.50542	0.823695	2	2	1	4
142.90962	0.812469	3	2	2	0

XRD data of TPA is given in Table D.7.

Table D.7. *XRD data for TPA*

Compound Name: Tungstophosphoric acid (TPA)

Chemical Formula: $H_3PW_{12}O_{40}$

PDF Card No: -

Radiation: $CuK_{\alpha 1}$

Wavelength: 1.5405 Å

2θ (°)	d-spacing (Å)	Intensity (%)
8.76	1.01	100
8.00	1.10	79
28.26	0.32	43
28.22	0.32	31
17.50	0.51	30
9.22	0.96	29
46.92	0.19	29
18.50	0.48	28
19.96	0.44	24
25.84	0.34	18

E. Conversion and Selectivity Calculations

CO conversion was calculated from equation E.1. Since CO was the only carbon source, all carbonaceous compounds were coming from CO. Stoichiometric coefficient of DME and ethanol are two since two mole of CO was required to produce one mole of ethanol or DME.

$$X_{CO} = \frac{n_{CO,0} - n_{CO}}{n_{CO,0}} = \frac{n_{CO_2} + n_{CH_4} + n_{meOH} + 2(n_{DME}) + n_{FA} + 2(n_{EtOH})}{n_{CO_2} + n_{CH_4} + n_{meOH} + 2(n_{DME}) + n_{FA} + 2(n_{EtOH}) + n_{CO}} \tag{E.1}$$

Selectivity of CO_2, CH_4, formic acid and methanol were calculated using equation E.2.

$$S_i = \frac{n_i}{n_T} = \frac{n_i}{n_{CO_2} + n_{CH_4} + n_{meOH} + 2(n_{DME}) + n_{FA} + 2(n_{EtOH}) + n_{CO}} \tag{E.2}$$

Selectivity of DME and ethanol were calculated using equation E.3.

$$S_i = \frac{2(n_i)}{n_T} = \frac{2(n_i)}{n_{CO_2} + n_{CH_4} + n_{meOH} + 2(n_{DME}) + n_{FA} + 2(n_{EtOH})} \tag{E.3}$$

Total, $CO + CO_2$, conversion was calculated using equation E.4.

$$X_{CO+CO_2} = \frac{(n_{CO,0} + n_{CO_2,0}) - (n_{CO} + n_{CO_2})}{n_{CO,0}} \tag{E.4}$$

where,

$$X_{CO+CO_2} = \frac{n_{CH_4} + n_{meOH} + 2(n_{DME}) + n_{FA} + 2(n_{EtOH})}{n_{CO_2} + n_{CH_4} + n_{meOH} + 2(n_{DME}) + n_{FA} + 2(n_{EtOH}) + n_{CO}}$$